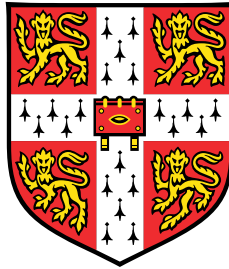


Thermographic particle image velocimetry: from phosphorescence to incandescence



Luming Fan

Department of Engineering
University of Cambridge

This dissertation is submitted for the degree of
Doctor of Philosophy

Queens' College

October 2018

I would like to dedicate this thesis to my beloved parents *Jing Wu* and *Jun Fan*.

Declaration

I hereby declare that except where specific reference is made to the work of others, the contents of this dissertation are original and have not been submitted in whole or in part for consideration for any other degree or qualification in this, or any other university. This dissertation is my own work and contains nothing which is the outcome of work done in collaboration with others, except as specified in the text and Acknowledgements. This dissertation contains fewer than 65,000 words including appendices, bibliography, footnotes, tables and equations and has fewer than 150 figures.

Luming Fan

October 2018

List of publications

Publications

L. Fan, Y. Gao, A. Hayakawa and S. Hochgreb. “ Simultaneous, two-camera, 2D gas-phase temperature and velocity measurements by thermographic particle image velocimetry with ZnO tracer ”. *Experiments in Fluids*, vol. 58:34 (2017). DOI: 10.1007/s00348-017-2313-2.

L. Fan, D. McGrath, C. T. Chong, M. N. M. Jaafar, H. Zhong, and S. Hochgreb. “Laser-induced incandescence particle image velocimetry (LII-PIV) for two phase flow velocity measurement”. *Experiments in Fluids*, 59:156 (2018). DOI: 10.1007/s00348-018-2610-4.

L. Fan and S. Hochgreb. “Uncertainty analysis in Structured Laser Illumination Planar Imaging (SLIPI) applied to non-linear signals: gas-phase phosphor thermometry”. *Measurement Science and Technology*, (2019). DOI: 10.1088/1361-6501/ab19ff.

B. Tian, C. T. Chong, **L. Fan**, J. Ng, C. Zhang and S. Hochgreb. “Soot volume fraction measurements over laminar pool flames of biofuels, diesel and blends”. *Proceedings of the Combustion Institute* (2018). DOI: 10.1016/j.proci.2018.05.094.

F. D. Domenico, P. Shah, B. Williams, P. Ewart, S. M. Lowe, **L. Fan** and S. Hochgreb. “High frequency measurement of temperature and composition spots with LITGS”. *Journal of Gas Turbines and Power*, 141(3):031003 (2018). DOI: 10.1115/1.4041275.

F. D. Domenico, **L. Fan**, S. M. Lowe, L. Weller, and S. Hochgreb. “Trade off between thermalisation and spatial resolution for LITGS measurements at 355 nm using biacetyl as an

absorber”. Accepted, 19th International Symposium on Applications of Laser and Imaging Techniques to Fluid Mechanics, July 2018, Lisbon, Portugal.

In preparation

L. Fan, C. T. Chong, P. M. D. Oliveira, B. Tian, and S. Hochgreb. “The effect of droplets on laminar propagation speed of an acetone-methane flame”.

Acknowledgements

I would like to express my genuine thanks to my supervisor Professor Simone Hochgreb, who has supported me so much during the past four years. I really enjoyed my PhD course under her guidance. I also want to thank my advisor Dr. Stuart Scott, who provided many great ideas on the phosphor synthesis, and generously offered me the opportunity to explore his chemical cabinet to find proper particles for my experiment. Special thanks to Dr. Cheng Tung Chong, his project sponsored my research here at the University of Cambridge.

Dr. Yi Gao is gratefully acknowledged: everything on optical alignment I had learnt was taught by her. Dr. Steve Lowe also passed numerous lab skills to me. I really missed the happy lab time together with them, although we were all struggling with the laser techniques we were working on (LITGS and TPIV).

Thanks to Cen, Kaiqi, Dante, Yaoyao, Bo, Francesca, Maxim, Anh Khoa, Robert, Jocelino, Pedro and other colleagues in the Hopkinson laboratory. It was so nice to have their company during this long journey. Thanks also go to other friends in Cambridge and my family, especially to Wenkai and Mengchen who took care of me when I fell sick during thesis writing. I will never forget their invaluable support. I am grateful for the help from our technicians: they are Roy, Robert, Peter, Mark, John and Ken. Without their efforts, none of the experiments described in this thesis can be achieved.

I also want to acknowledge the informal discussions with Professor Frank Beyrau, Dr. Benoit Fond, and Dr. Christopher Abram. This thesis is built upon their great work.

Finally, thanks to the readers of this thesis. I hope it could help.

Abstract

Thermographic PIV is a promising technique that enables simultaneous temperature and velocity imaging in flows with intentional seeded phosphor particles. This is highly attractive to researchers in fluid mechanics and combustion, as it directly visualizes the heat and mass transfer process in turbulent flows/flames. However, three problems for this technique are: (a) it requires two lasers and three cameras running simultaneously, making it a high-cost technique; (b) several recent studies reported the multiple scattering effects for gas-phase phosphor thermometry, which may severely bias the temperature measurement for certain flow configurations; and (c) the phosphorescent emission disappears at high temperature due to thermal quenching, which limits the temperature measurements to mostly non-reacting cases below 1100 K.

This dissertation is aimed at providing solutions to the issues described above. To reduce the cost of the current thermographic PIV setup, a simplified version is proposed which uses a double-pulsed laser with UV capacity and two CCD cameras operating in the double-frame mode. This experiment proves that, apart from Mie scattering, phosphorescence image pairs can also be used to perform cross-correlation and calculate the vector field. Therefore both velocity and temperature field can be extracted from phosphorescence emissions excited by a single laser (UV-PIV). Thermographic PIV with this simplified setup is demonstrated on an electrically heated air jet, and 3 K accuracy is achieved in the core region of the jet, by comparing with a thermocouple scan. A novel calibration process is also proposed to eliminate the influence of non-uniform laser profile on the temperature measurements.

The same technique is also applied to visualize heat transfer in an impinging jet. By correlating the instantaneous gaseous temperature fields with the averaged Nu profiles derived

from the wall temperature, the role of vortical structures in heat transfer is investigated and discussed.

During the application of thermographic PIV, the problem of multiple scattering emerged and has been reported by several studies, especially for cases where an excessive seeding is used. Multiple scattering was found to reduce the spatial resolution and bias the temperature measurements. A recent study demonstrated that the Structured Laser Illumination Planar Imaging (SLIPI) technique could effectively remove multiple scattering and near-wall effects from the LIP image. However, it is well known that the emission spectrum of some most commonly used thermographic phosphors is sensitive to the changes in laser fluence, whilst SLIPI intentionally modulates the laser profiles and thus may bring in uncertainty into the temperature retrieval. This has yet not been discussed in the literature. In this dissertation, a numerical analysis is conducted, by generating artificial laser induced phosphorescence images, to investigate the effects that SLIPI may have on the temperature measurements.

To implement simultaneous temperature and velocity measurements in flames, an entirely new approach of thermographic PIV is proposed in this dissertation. This new version is based on laser-induced incandescence (LII), rather than phosphorescence. Submicron black particles are seeded into a flame, and further heated by a high-energy top-hat laser sheet to several thousands kelvin. The particle temperature T_p can be measured by two-color pyrometry, where the temperature increase ΔT due to laser absorption can be determined by conducting an *in-situ* calibration. Thus the local temperature T_0 can be indirectly determined by subtracting ΔT from T_p . The same particle can also be used as PIV tracers. The concept and fundamentals of this new thermographic PIV approach are described in this thesis.

The combination of LII and PIV is also applied as a tool to measure the gas-phase velocity in a two-phase flow, which is a canonical problem for multiphase flow studies.

Table of contents

List of figures	xix
List of tables	xxix
1 Introduction	1
1.1 Multi-physics measurement in fluids	1
1.1.1 Filtered Rayleigh scattering (FRS) with PIV	4
1.1.2 Planar laser-induced fluorescence (PLIF) with PIV	4
1.1.3 Thermographic PIV	5
1.2 An overview of laser-induced fluorescence, phosphorescence, and incandescence	10
1.3 Objectives	11
1.4 Thesis structure	12
2 Simultaneous 2D, two-camera, thermographic PIV demonstration with ZnO tracers	15
2.1 Introduction	15
2.2 Experimental setup	16
2.2.1 Flow system	16
2.2.2 Optical system	17
2.2.3 Timing optimization	21
2.3 Calibration	22
2.3.1 ZnO calibration curves as a function of laser intensity	22

2.3.2	Laser sheet profile	25
2.3.3	Final calibration function	26
2.3.4	Laser sheet profile for double pulse mode	27
2.4	Operating conditions	28
2.5	Data processing	29
2.5.1	Thermography	29
2.5.2	Particle image velocimetry	30
2.6	Results and discussion	31
2.6.1	Temperature imaging	31
2.6.2	Simultaneous velocity and temperature imaging	34
2.7	Summary	36
2.8	Further Considerations	37
2.8.1	Double-pulsed UV laser	37
2.8.2	Particle size for velocity and temperature measurement	38
2.8.3	Phosphor particles with a longer decay time	39
3	Heat transfer visualization in a laminar impinging jet using phosphor thermography	41
3.1	Introduction	41
3.1.1	Impinging jet	41
3.1.2	Flow field measurement	43
3.1.3	Objectives	44
3.2	Experimental	45
3.2.1	Thin stainless steel foil	45
3.2.2	Infrared thermography	46
3.2.3	Flow and particle seeding system	47
3.2.4	Phosphor thermography	48
3.2.5	Image processing	52
3.2.6	Calibration of ZnO tracer	52
3.2.7	Test conditions	54

3.3	Determination of Nusselt number	55
3.3.1	Results and discussion	56
3.4	Temperature imaging	57
3.5	Summary	59
4	Numerical analysis on SLIPI: gas-phase phosphor thermometry	63
4.1	Introduction	63
4.1.1	Multiple scattering	63
4.1.2	SLIPI	66
4.2	Numerical method	70
4.2.1	PIV Synthetic Image Generator (SIG)	70
4.2.2	Adapted SIG for phosphor particles (LIP-SIG)	70
4.2.3	Emission behaviour dependence on temperature and laser fluence	73
4.2.4	SLIPI subimage generation and image reconstruction	75
4.3	Effect of non-linearity on signal yield	77
4.4	Effect of intensity ratio changes to laser fluences	81
4.5	Degree of multiple scattering	84
4.5.1	Overestimation caused by non-linear signal yield	85
4.5.2	Overestimation caused by particle image diffraction	85
4.6	Simulation uncertainties	87
4.7	Possible applications of the LIP-SIG program	88
4.8	Conclusions	89
5	TPIV based on LII signal from submicron black particles: concept and model	93
5.1	Introduction	93
5.2	Model	95
5.2.1	Particle temperature	95
5.2.2	Two-colour pyrometry and gas temperature	98
5.2.3	Tracer particle selection	101
5.3	Numeric results and discussions	102

5.3.1	Particle temperature and integrated LII signal	102
5.3.2	Sensitivity and dynamic range	105
5.3.3	Detection wavelengths and 2-color ratio	106
5.4	Summary	110
5.5	Further considerations	111
5.5.1	Tungsten carbide	111
5.5.2	Particle size for velocity and temperature measurement	111
6	LII-based particle image velocimetry for two phase flow velocity measurement	113
6.1	Introduction	113
6.2	Experimental	117
6.2.1	Optical system	117
6.2.2	Particles	118
6.2.3	Seeding density	119
6.2.4	Effects of the LII decay time on the maximum measurable velocity	120
6.3	LII-PIV demonstration on an air jet	121
6.3.1	Operating conditions	121
6.3.2	Raw images and data processing	123
6.3.3	Results and discussion	125
6.4	LII-PIV on a non-reacting droplet-laden flow	128
6.4.1	Operating conditions	128
6.4.2	Results and discussion: LII and droplet PIV	130
6.5	Demonstration of LII-PIV on a flame	134
6.5.1	Operating conditions	134
6.5.2	Results and discussion: WC flame PIV	135
6.5.3	Possibility of applying LII-PIV to a sooty flame	138
6.6	Summary	138
7	Conclusions and future work	141
7.1	Conclusions	141

7.2	Future work	144
7.2.1	Experimental demonstration of LII-TPIV	144
7.2.2	C-dot thermographic PIV	144
7.2.3	Thermographic phosphor synthesis by the impregnation method . .	146
7.2.4	Simultaneous temperature and velocity imaging on a droplet-laden flat flame by TPIV	147
7.2.5	LII-PIV on a droplet-laden flame and a sooting flame	147
	References	149

List of figures

1.1	An example of using the two frames of a PIV camera to capture phosphorescence (first frame, <i>left</i>) and Mie scattering signal (second frame <i>right</i>) from the same ZnO particles at a short time interval $\delta t = 10 \mu s$. A long pass filter ($> 400 \text{ nm}$) was installed in front of the camera. When the camera was focusing on the phosphorescent particle images, the Mie scattering image was defocused and vice versa.	3
1.2	Jablonski energy level diagram, adapted from [15].	11
2.1	Experimental setup. BD: beam dump; BS: beam splitter; CL: cylindrical lens; F: short band pass filter; FL: focal length; M: mirror; PD: photodiode. Cameras are non-intensified.	19
2.2	Timing diagram for (a) calibration of ZnO; (b) thermographic PIV measurements. The camera shutter opens $1 \mu s$ prior to the laser pulse in case of laser jittering. The diagram is not scaled to the actual time annotated.	20
2.3	Single-shot intensities of first and second frames obtained with Cameras A and B at two different wavelength ranges as indicated. Upper row: first frames recorded at time t ; bottom row: second frames recorded at time $t + 30 \mu s$. Images in the same row were used to calculate intensity ratio. Images on the right column were used to perform cross-correlation for PIV.	22

2.4	Schematic variation of normalized laser energy per pulse, probability of finding cross-correlation P_c , as a function of timing interval Δt between images. For PIV, the total energy was evenly distributed between the two pulses ($E_1 = E_2$). The particle seeding density, and hence the signal intensity, is proportional to the flow rate passing through the seeder.	23
2.5	(a) Mean intensity ratio of signal over wavelength range 450 ± 25 nm to that at wavelength range 387 ± 5.5 nm for a total laser energy of 8.6 mJ at a temperature 424 K in the marked region; (b) mean intensity ratio of the square region shown in (a), as a function of temperature and mean laser pulse energy (mJ). Intensity ratio variances are presented as vertical error bars. Lines are second order polynomial fits for each energy.	24
2.6	(a) Fluorescence from excited Coumarin 460 in a cuvette as recorded by camera B; (b) fluence obtained from highlighted region (1504×50 pixels) in (a) and the measured mean energy (mJ/cm^2) for varying energy levels. The dashed line indicates the center of the calibration region, with corresponding to fluences of 20, 33, 51, 76, $213 \text{ mJ}/\text{cm}^2$	26
2.7	Calibration function $I_r = I_r(T, F)$	27
2.8	(<i>left</i>) Laser fluence profile $F(z)$ for the first (blue) and second (red) pulses; (<i>right</i>) normalized shape function of the fluence profile. Averages represented by the solid line, standard deviation by the error bars.	28
2.9	Resulting sample temperature fields (K) after each image processing step for removing large aggregates. The area of the shown region is 150×150 pixel (3.3×3.3 mm)	30
2.10	Example single shot of temperature field at time t (<i>left</i>) and $t + 30 \mu\text{s}$ (<i>right</i>) based on calibration function $I_r(T, F)$	31
2.11	Mean temperature field obtained for the first pulse at time t (<i>left</i>) and second pulse at time $t + 30 \mu\text{s}$ (<i>right</i>). The laser sheet enters from the left side. To eliminate the effects of the CCD transfer noise, the mean temperature fields were smoothed by a 30-pixel (0.66 mm) 1D moving average along the vertical direction.	32

2.12	Mean temperature profiles processed from the first frame (<i>red</i>) and the second frame (<i>blue</i>), compared to values measured by a thermocouple (<i>dashed line with circles</i>) for an axial distance 10 mm (<i>top</i>) and 5 mm (<i>bottom</i>).	33
2.13	Temperature rms processed from the (<i>left</i>) first frames; (<i>right</i>) second frames at $t + 30 \mu\text{s}$	34
2.14	Two examples (<i>top and bottom</i>) of simultaneous temperature (<i>left column</i>) and velocity (<i>right column</i>) imaging. The vorticity contours are superimposed onto the temperature field. As expected, the temperature structures show similarities to the velocity structures.	35
3.1	A schematic view of an impinging jet, after [51]	42
3.2	(a) Schematic view of the heated-thin-foil setup. The Infrared camera was on top of foil but not shown in this figure; (b) detail design of the terminals.	46
3.3	A schematic view of the impinging jet (burner cross-section), and two measurement positions.	48
3.4	Experimental setup. BD beam dump; BS beam splitter; CL cylindrical lens; F bandpass filter; FL focal length; IR infrared camera; M mirror.	49
3.5	Example raw image for (a) cold foil at room temperature (293 K) and (b) heated foil at 623 K, both collected from the red channel. The colorbar shows the camera count. In the latter case, the particles on the surface were strongly quenched by the high temperature.	51
3.6	A scan of intensity ratio versus the averaged intensity (red channel) in the probe volume over 800 images, for inlet temperatures of 291, 351, 405 and 472 K, respectively. Images whose intensity in the core region was below 22 counts may bias the temperature measurements and were rejected.	53
3.7	(a) Mean intensity ratio ($425 \pm 25 \text{ nm}$ over $387 \pm 5.5 \text{ nm}$) at 472 K in the marked probe volume; (b) mean intensity ratio as a function of temperature in the marked region. Intensity ratio RMS are presented as vertical error bars. Circles are the calibration data points, and the black line is the best quadratic fit.	54

3.8	Nusselt number profiles calculated by the traditional heat flux method, for $H/D = 1.0, 2.0, 3.0$ and 4.0 , respectively.	57
3.9	Examples of instantaneous temperature field for (<i>upper</i>) $H/D = 2.0$, and (<i>bottom</i>) $H/D = 4.0$. The <i>left column</i> shows the raw phosphorescence image collected from the red channel, whilst the <i>left column</i> shows the corresponding temperature field.	58
3.10	(<i>Upper</i>) mean and (<i>bottom</i>) RMS temperature field measured for $H/D = 1, 2, 3$, and 4	60
4.1	Three mechanisms of multiple scattering for phosphorescence: (a) Elastic scattering of the phosphor signal emitted from the measurement plane; (b) excitation of phosphors by the scattered laser light; and (c) preferential re-absorption and secondary emission. The <i>black solid circles</i> represent phosphor particles.	64
4.2	Schematic diagram of three modulated harmonic sub-signals in non-dimensional space, showing the corresponding reconstructed signals.	66
4.3	Experimentally obtained response curves for ZnO at 350 K. <i>Blue circles</i> are data points collected at the blue channel and <i>red circles</i> at the red channel. The <i>lines</i> shows the corresponding two-term exponential fittings of the form $y = Ae^{ax} - Be^{bx}$	73
4.4	Flow chart for SLIPI image synthesis and reconstruction for linear signal behaviour: (a) definition of a modulated laser profile F and a uniform temperature field (350 K); (b) generation of 50 single-shots SLIPI images (200×200 pixels) using the number of particles ($N = 5000$), using a fixed gain function $G(\lambda, T)$; (c) addition of constant synthetic signals $I_{DC,b}$ and $I_{DC,r}$ to the two channels; (d) extraction of temperature field from conventional and SLIPI reconstructed image. As expected, the SLIPI operation corrects the temperature bias caused by intentionally added unmodulated signals I_{DC}	76
4.5	A convergence study of intensity ratio as a function of number of images averaged for SLIPI algorithm. $N = 5000$ for each single shot (0.125 particle/pixel). For static particles, as we assumed in this study, convergence can always be achieved; For moving particles, 20 images are sufficient to converge the temperature extraction for this high seeding level.	77

- 4.6 (a) Reconstructed SLIPI image on blue channel for two selected test fluences (peak fluence). The *upper row* shows the case for 30 mJ/cm^2 (linear regime) and the *bottom row* for 250 mJ/cm^2 (close to saturation); (b) horizontally averaged intensity profile of the SLIPI reconstructed image. Residual noise can be observed for the case of 250 mJ/cm^2 at a frequency of 3ν , where ν is the spatial frequency of the Ronchi grating modulation; 78
- 4.7 A the amplitude of true signal (*dotted line*) and the average intensity I_s (*solid line*) as a function of laser fluence on blue channel. For linear response, I_s should equal to A . However for the present non-linear response curves, a discrepancy between I_s and A is identified. 80
- 4.8 (a) Intensity ratio R_{rb} as a function of laser fluence at 350 K, based on experimental data collected from ZnO. *Circles* are averaged data points, and the *curve* is the best fit to the data points; (b) reconstructed SLIPI images for the two channels; (c) temperature field extracted from the reconstructed SLIPI images, and (d) after a low pass field was applied to (b), the streaks on temperature field are removed. For this case, $N = 5000$, period of modulation is 20 pixels, the laser fluence is 30 mJ/cm^2 82
- 4.9 Temperature extracted from conventional (T_c) and SLIPI images (T_s) as a function of excitation fluence. No multiple scattering was applied to the synthetic images, so the temperature bias is purely caused by the saturating emission characteristics of ZnO. For the cases simulated in this figure, $N = 5000$, $T = 350 \text{ K}$, and the period of modulation is 20 pixels. 83
- 4.10 Spurious degree of multiple scattering ϕ reported by SLIPI in both blue (*blue circles*) and red (*red circles*) channels for reference synthetic LIP images where zero multiple scatter signal was added, as a function of (a) particle number N , (b) particle images diameter d_τ , and (c) period of laser sheet modulation $1/\nu$, respectively. For unchanged variables, excitation fluence is 30 mJ/cm^2 , particle number $N = 5000$, laser sheet modulation 10 pixels, and particle image diameter 3 pixels. The temperatures T_s extracted from the SLIPI recovered images are also plotted in the same figure on the y axis on the right side. 86

- 4.11 SLIPI recovered temperature T_s as a function of excitation fluences, for (a) an emission intensity in proportional to d_p^2 or d_p^3 ; (b) a Gaussian or top-hat particle image profile; (c) a constant or a varying particle image size d_τ over the simulation field. The distributions of d_p and d_τ are plotted in the subfigures accordingly. Other parameters are kept the same as Fig. 4.9. 87
- 5.1 (Row 1) Particle temperature profile T_p for different particle sizes and laser fluences. The blue line illustrates the result given by the non-heat-loss model; (Row 2) temporal profile of LII signal S_λ detected at 400 nm wavelength for $d_p = 100$ nm; (Row 3) Time integral of the LII signal S_I at 400 nm captured by a camera as a function of gating time, the dashed line denotes the time when the difference S_I given by the two models reaches 10 %; (Row 4) the relative error of measured particle temperature T_m by two cameras (400/780 nm) to the adiabatic particle temperature T_a , as a function of gating time δt , particle size d_p and laser fluences F . Other input conditions are: $T_0 = 1800$ K, $\lambda_L = 532$ nm. 103
- 5.2 Numerical results of (a) fluence dependence of LII signal magnitude for $T_0 = 1800$ K, normalized at $F = 0.2$ J/cm² (b) time integral of LII signal S_I as a function of T_0 at 5 levels of laser fluence. Other input conditions: $d_p(t = 0) = 100$ nm, $\lambda_L = 532$ nm, $\lambda_s = 400$ nm, $\delta t = 20$ ns 106
- 5.3 Time integral of LII signal S_I at various detection wavelength ranging from 400 nm to 700 nm, as a function of ambient temperature T_0 . Input conditions: $d_p = 100$ nm, $F = 0.05$ J/cm², $\lambda_L = 532$ nm. Gating time $\delta t = 20$ ns. 108
- 5.4 (a) Numerical results of signal ratio (Gating time $\delta t = 20$ ns) as a function of ambient temperature for four combination of detection wavelengths, (b) the same curves in (a) are normalized to unity at $T_0 = 400$ K. Cases for both spectral lines (triangle) and bandpass filters (circle) were simulated. 109

- 6.1 First frame shots of a PIV image pair based on Mie scattering (*top row*), and LII signal (*bottom row*) in an air jet. Tracers are $0.2\ \mu\text{m}$ WC and $1\ \mu\text{m}$ alumina respectively (*columns*). The colorbars show the actual intensity counts recorded by the camera, which saturates at 9900 counts and has a dark noise around 5 counts. Note that the *hot* colormap is used to represent the incandescence signal, but it was actually collected from a blue channel ($425\pm 25\ \text{nm}$). 122
- 6.2 (a) Mie-scatter image of WC particles; (b) LII image of WC particles, both extracted from the first frame; (c) preprocessed LII image; (d) velocity field obtained at the same position based on the LII image pair (second frame not shown here). To present the robustness of the proposed technique, the vector field shown in (d) has not been post-processed by any interpolation or smoothing, and the interrogation region for removed vectors are shown in white. The area of the shown region is 200×200 pixel ($6.4\times 6.4\ \text{mm}^2$) 123
- 6.3 Example of single-shot velocity field based on (a) Mie scattering of $1\ \mu\text{m}$ alumina and (b) LII signal from WC. Note they were taken non-simultaneously. Removed vectors are intentionally left blank rather than interpolated. The percentage of remaining vectors in the marked region after median filtering (averaged over 400 single-shots) is 87% and 84% for Mie-scatter and LII-based PIV, respectively. . . . 125
- 6.4 Velocity probability density function (normalized) calculated from the marked region in Figure 6.3 over 400 single-shots. *Black line* denotes the LII-based PIV, and *red dotted line* represents the result from Mie-scatter PIV. 126
- 6.5 (a) Mean velocity field for the same air jet, measured with $1\ \mu\text{m}$ alumina (left half) and $0.2\ \mu\text{m}$ WC (right half). (b) The velocity profiles at $h = 15, 25, 35\ \text{mm}$ are extracted and compared. The LII-PIV with WC matches well with the results given by the $1\ \mu\text{m}$ alumina case (normal PIV). 127

6.6	(a) Velocity rms for the same air jet, measured with 1 μm alumina (left half) and 0.2 μm WC (right half). (b) The velocity profiles at $h = 15, 25, 35$ mm are extracted and compared. The velocity measurement by LII-PIV is more susceptible than Mie-PIV to the drop of seeding density in the mixing layer, hence a higher velocity rms is observed in this region.	128
6.7	(a) Schematic view of the laminar flame burner and the droplet-laden flow; (b) size distribution of the ethanol droplets measured by a PDA system at the outlet of the burner. A total number of 5000 droplets were sampled, and the size distribution is cut off at 80 μm , limited by the mask installed in front of the PDA detector. The bars show the measured data and the red curve is the best log-normal fitting to the bars.	129
6.8	Zoomed-in view of (a) Mie scattering and (b) LII image from the droplet/WC/air mixture.	131
6.9	Single-shot velocity field based on (a) Mie scattering from droplets and (b) LII signal from WC, which represents the gas-phase motion in this droplet-laden flow. Removed vectors are left blank intentionally. Note they were taken non-simultaneously.	132
6.10	(a) Mean velocity field of liquid phase (<i>left</i>) and gas phase (<i>right</i>); (b) The velocity profiles at $h = 15, 25, 35$ mm are extracted and compared. Ethanol droplets move significantly more slowly than the gaseous flow due to the effect of gravity relatively to the drag force. The dashed square marks the region where velocity PDFs in Fig. 6.12 are calculated.	133
6.11	(a) Velocity rms of liquid phase (<i>left</i>) and gas phase (<i>right</i>); (b) The velocity profiles at $h = 15, 25, 35$ mm are extracted and compared. In the jet core (well seeding) the gas-phase velocity fluctuation is slightly higher than that of the liquid-phase. . . .	133
6.12	Velocity PDFs calculated over the marked region in figure 6.10(a). <i>Black line</i> shows the gas phase velocity, whilst <i>blue line</i> presents the droplet velocity. For comparison, the velocity PDF based on 1 μm alumina (<i>red dotted line</i>) measured without the presence of droplets is also plotted.	134
6.13	Schematic view of the stagnation flame configuration.	135

-
- 6.14 (a,b) First frame a example PIV image; (c,d) Preprocessed image (first frame); (e,f) second frame of the PIV image; (g,h) Preprocessed image (second frame); (i,j) Mean velocity field. *Left column* is based on Mie scattering from alumina tracer, and *right column* on LII signal from tungsten carbide particles, respectively. 136
- 7.1 (a) Carbon dot solutions synthesized from candle soot, after [146]. The emission spectrum changes with the fraction of soot added into the reaction; (b) fluorescence image of C-dots depositing on a glass substrate by spray, under 365 nm argon laser excitation, adapted from [149]; (c) the emission spectrum of carbon dots shows some temperature dependency, adapted from [148]. 145
- 7.2 A schematic of (a) conventional firing method for phosphor synthesis, and (b) proposed method combining impregnation and firing for phosphor synthesis. . . . 146

List of tables

5.1 Simulation Parameters 98

Chapter 1

Introduction

1.1 Multi-physics measurement in fluids

Laser diagnostics techniques are important tools for combustion and other fluid mechanics studies. Most *in-situ* physical and chemical parameters, such as velocity, temperature, pressure, species concentration, mixture fraction, heat release rate, soot volume fraction etc., both point-based and two dimensional, time-resolved and spatial-resolved, have been successfully measured by laser techniques invented over the past four decades. To date, great efforts are still spared on developing new laser diagnostic techniques as well as improving the existing ones in order to extend the application of these techniques to much harsher environments as in a real combustor, where very limited optical access is allowed. Other challenges for such in-chamber measurements include extremely high temperature and pressure (thus a considerable change in refractive index which alters the laser pathway), strong flame luminosity, and severe signal trapping by soot.

While researchers are focusing on techniques for single parameter detection with higher accuracy and repeatability, in recent years, simultaneous multiple-quantity measurements in flows have also attracted considerable attention. Multiple-quantity measurements collect information of two or more parameters at the same time, which are highly of interest to researchers on fluid mechanics and combustion science because they can reveal the interaction between different quantities. For example, in turbulent combustion, the heat released in a

reaction greatly raises the local fluid temperature, which in consequence leads to changes in flow density, vector field and thus the transport of both burnt and unburnt reactants. The transport of reactants in return affects the reaction and the heat release rate. Obtaining information for several parameters (in this case the velocity, species concentration, and fluid temperature), especially 2D imaging and volumetric measurements by fast scanning, will greatly contribute to our understanding of the interaction between turbulence and reactions. The simplest way one can conceive to implement multi-physics measurements is to combine different techniques together. However, practically it is not that easy to add two or more detection system together, due to the following reasons:

(a) the existence of a different type of tracer may strongly interfere with the other technique performed at the same time. For example, in the presence of PIV particle tracers, the weak Rayleigh scattering signal from gas molecules will be buried into the strong Mie scattering signal which saturates detectors easily. Another example can be the combination of PLIF to PIV in a water tank. In a study on performing simultaneous PLIF and PIV in a water tank [1], the PIV particles were reported to deposit on the glass wall where the laser light entered and thus created streaks on the LIF image, which affected the quality of fluid temperature measurement;

(b) Aligning several laser sheets of different wavelengths can be difficult. Although high quality commercial beam combiners/dichroic mirrors are available, problems appear when the combined beams pass through the light sheet forming lenses. The focal length of a convex or concave lens changes with the wavelength of incident light, however the marked focal length for most commercial lenses are calibrated at a wavelength roughly in the centre of the visible range (400-700 nm), for example at 587.6 nm for all cylindrical lenses from Thorlabs. This means that the beam waist for different color light sheets formed by the same cylindrical lenses locates at different positions, and that the light sheet thickness will be very different at the test section especially when the wavelengths are far away from each other on the spectrum. This causes a discrepancy on the spatial resolution for different physical quantities and weakens the correlations between them. One possible way to solve this problem is to form two light sheets separately, and then to combine the light sheets on a

dichroic mirror. However, this requires the use of a large and expensive dichroic mirror with a high damage threshold. The same problem also applies to the imaging system with a widely opened aperture, because a camera lens is in essence a combination of several spherical lenses. Figure 1.1 shows an attempt to use the two frames of a PIV camera to capture the phosphorescence signal (first frame) and Mie scattering signal (second frame) from the same ZnO particles. The 355 nm light sheet was formed separately, and then carefully aligned and overlapped with a 527 nm green light sheet. A time delay of $10 \mu\text{s}$ was set to the 527 nm light source (single-pulsed) so as to let it be captured by the second frame. It can be observed clearly that when the camera was focusing on the phosphorescence particle image (400-475 nm), the Mie scattering particle image (527 nm) was defocused and vice versa.

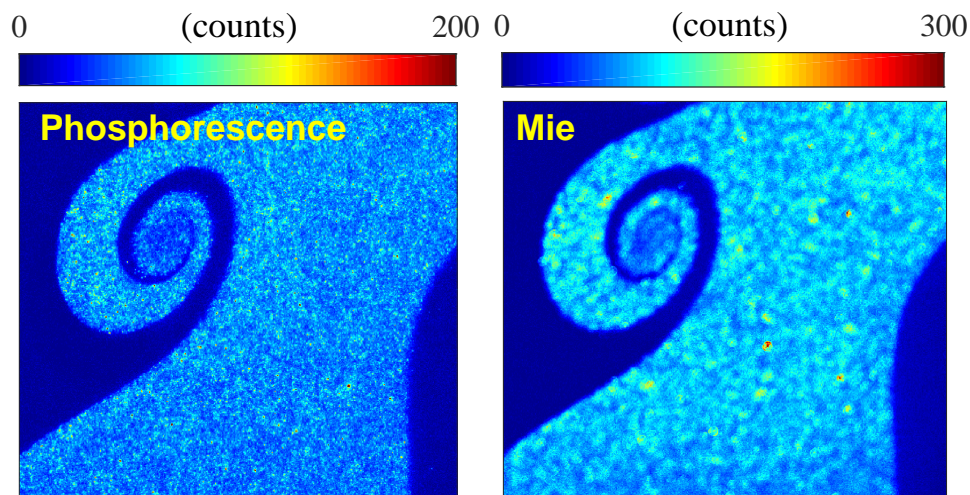


Fig. 1.1 An example of using the two frames of a PIV camera to capture phosphorescence (first frame, *left*) and Mie scattering signal (second frame *right*) from the same ZnO particles at a short time interval $\delta t = 10 \mu\text{s}$. A long pass filter ($> 400 \text{ nm}$) was installed in front of the camera. When the camera was focusing on the phosphorescent particle images, the Mie scattering image was defocused and vice versa.

(c) The expense of combining several laser techniques may be very high, since several lasers and cameras are running simultaneously. This may not be affordable to many laboratories. To reduce the number of lasers and cameras used by applying smart imaging, timing and gating strategies is another meaningful topic for the spread of such multi-physics measurement techniques.

Despite the difficulties, there have still been a large number of multi-physics measurements conducted in either liquid or gaseous flows. In this section, several techniques for simultaneous temperature and velocity measurement are reviewed.

1.1.1 Filtered Rayleigh scattering (FRS) with PIV

Flame temperature can be measured by Rayleigh scattering from gas molecules, because the Rayleigh scattering cross-section is governed by laser light intensity, temperature, pressure and gas composition. If intensity, pressure and gas composition are known parameters, the gas temperature T can be deduced from models. When Rayleigh thermometry is combined with PIV for simultaneous temperature and velocity measurements, however, the presence of particles strongly interferes with the Rayleigh signal which is much weaker than the strong Mie scattering from PIV particles. One solution to overcome this is the filtered Rayleigh scattering (FRS). Since on the spectral domain the Rayleigh scattering signal is broader than Mie scattering, a molecular filter (usually iodine) is used to remove the Mie signal from particles, whilst the two side wings of the Rayleigh signal are preserved. Using the remaining Rayleigh signal, the original profile on spectrum domain can be recovered, from which the temperature information is extracted. FRS has been demonstrated as a thermography technique in particle laden flames by [2–5], and combined with PIV to achieve simultaneous temperature and velocity measurements in [6].

FRS-PIV has been successfully applied in flames, showing a great potential in multi-physics measurements for combustion studies. However, it requires the use of high-power lasers, and is a relatively complex technique. Further, the temperature accuracy of FRS can be very poor in some cases, for example a 23% temperature bias at 1800 K was estimated in [6] as a worst case scenario.

1.1.2 Planar laser-induced fluorescence (PLIF) with PIV

Another possibility is to combine planar two-line laser-induced fluorescence (PLIF) with PIV. Temperature information can be extracted from the ratio of fluorescence signal released from

two different transitions. Most commonly used small molecular temperature tracers in flames are NO [7] and OH [8]. However, OH only appears in regions near the product zone, whilst intentionally seeded NO is highly toxic, which requires strict risk assessment prior to the experiment. Organic tracers decompose at high temperatures and hence are not suitable for in-flame measurements. Most simultaneous temperature and velocity measurements using combined PLIF and PIV have been conducted in non-reacting cases such as in a impinging jet [9], or in water [10]. In addition, multi-line PLIF/PIV requires two lasers and two cameras operating simultaneously, again making it a high-cost technique. For organic molecular tracers, acetone and toluene PLIF were frequently used in heat transfer measurements. However these highly diffusive chemicals could be harmful or even carcinogens to humans. In addition, they will condense at low temperatures, which prevents them to be used in cryogenic applications.

1.1.3 Thermographic PIV

Apart from the techniques reviewed above, thermographic particle image velocimetry (TPIV) is a recently introduced technique for simultaneous 2D temperature and velocity measurements in gaseous or liquid flows. In essence, it is a combination of laser-induced phosphorescence (LIP) and particle image velocimetry (PIV). The temperature field is detected from the ratio of the phosphorescence emitted at two spectral bands from phosphor particles excited by a UV light source, while the velocity field is calculated from the cross-correlation of two consecutive images that record the Mie scattering from the same particles illuminated by a double-pulsed laser.

Thermographic phosphors were previously investigated for surface thermometry on engines and gas turbines, and comprehensive reviews of such studies have been produced [11–13]. Applications of thermographic phosphor on fluid temperature measurements have also been reviewed by Abram and co-workers in a recent publication [14]. There are numerous types of phosphor, and their detectable temperature range varies, according to the dependence of their life time, spectral characteristics and phosphorescence yield on temperature. In general, both phosphorescence yield and lifetime decrease with temperature, often limiting

the range of application. The theory of phosphorescence is a continuing topic in material science due to its wide application to devices such as LEDs and solid-state lasers. Most thermographic phosphor tracers consist of a ceramic lattice doped with one or more types of rare-earth ions [15], which can sustain temperatures up to 2000 K [16]. Following photo-excitation, typically by UV light, ions in the host lattice in a phosphor particle are raised to higher energy states, and their relaxation to the ground state is accompanied by both radiative emission and non-radiative quenching. The possibility of the latter increases with stronger thermal vibrations of the host and becomes predominant at high temperatures, which leads to temperature sensitivity of both emission spectrum and decay time [17]. For most types of phosphor, the emission shows both a spectral shift and a faster decay time at higher temperature. These two temperature dependent characteristics have been used for surface thermography and developed as two different approaches: an intensity ratio method and a decay time method. Fuhrmann *et al.* [18] compared these two approaches for surface thermography and reported that the lifetime method was superior over the ratio-based method because of its high accuracy and precision especially at high temperatures. However, this time-resolved method may not be suitable for fast moving objects, because the lifetime of the chosen phosphor ($\text{Mg}_4\text{FGeO}_6:\text{Mn}$) (hence the measurement time) is too long to properly resolve the temperature field. The ratio method has more recently been used in a number of studies for 2D gas-phase temperature measurements based on the intensity ratio of the phosphorescent emission of particles at different wavelengths [19–25].

The emission characteristics of different phosphors have been investigated for decades, but most of these studies were based on phosphor particles in bulk or bonded to a surface. Recently, the photo-luminescent behavior of phosphor particles dispersed in flows was shown to be quite different from that observed in the bulk material [16, 24], suggesting that the calibration of the relationship between temperature to intensity ratio must be conducted in using dispersed particles. A particle counting system was developed to investigate the emission characteristics based on individual $\text{BAM}:\text{Eu}^{2+}$ particles in dispersed form [26, 27], while considering different laser fluences, seeding densities and their effects on the accuracy of the temperature measurement. The result showed that the intensity ratio was dependent on

the local laser fluence, and a normalization by the mean intensity-ratio field obtained at room temperature was proposed to eliminate the effects of spatial variation.

The LIP technique also shows potential for achieving multi-physics measurements in turbulent flows [28]. Omrane *et al.* [29] demonstrated simultaneous 2D measurements of gas-phase temperature and velocity for the first time, where two systems were used: a Nd:YAG laser operating at 355 nm to form a UV laser sheet and an ICCD camera with a stereoscope for two-color imaging, and a double-pulsed PIV laser providing a laser sheet at 532 nm in the same plane, collected by a non-intensified PIV double-frame imaging camera. This two-system setup was followed by [30] and [31]: the former demonstrated simultaneous 2D temperature and velocity measurements on a heated jet with Dy:YAG and Dy:Er:YAG tracers, while the latter achieved such measurements in a diesel engine with Pr:YAG tracers. Fond *et al.* [16] demonstrated simultaneous 2D measurements of temperature, velocity and mixture fraction on a heated jet, where the ICCD cameras were replaced by two non-intensified cameras. The result shows that non-intensified CCD cameras performed well in capturing the phosphorescence emission from BAM:Eu²⁺ at a temperature below 800 K. The same technique was repeated with two high-speed laser systems with additional three non-intensified CMOS cameras [32]. Recently, point-based simultaneous temperature and velocity measurements with phosphor particles were also achieved by combining LDA and LIP [33]. Following this work, a novel phase-shifted luminescence technique was developed [34], which used a temporally modulated CW laser beam to excite BAM:Eu²⁺ particles. The life time of the emission was accurately determined from the phase-shift between the light source and the emission. This smart innovation inherits the high-accuracy of lifetime method but at the same time circumvents the drawback of long measurement time, hence it can be potentially applied to measure turbulent flows.

The ratio-based thermographic PIV demonstrated by all aforementioned studies was realized by using two systems, consisting of 2 lasers and at least 3 cameras (or 2 with a stereoscope [29]) running simultaneously, making it a resource-intensive technique. The exact overlap of two laser sheets requires additional dichroic optics, and proper alignment. Using lifetime-based thermographic PIV, Someya and co-workers [35] seeded MFG particles,

a phosphor with a lifetime much longer than BAM:Eu²⁺, into an optical engine and excited by a single-pulsed UV laser sheet. A high-speed camera running at 40000 fps recorded the signal decay of the MFG tracers. The phosphor lifetime (hence the temperature) was estimated from the first four consecutive images after each pulse, and the velocity was also calculated based on the same images (single-pulse multi-frame PIV). According to the reported result, the lifetime thermographic PIV suffers from weaknesses such as long measurement time (hence not suitable for turbulent flows), narrow applicable temperature range (decay time drops drastically as temperature rises), and small field of view/poor resolution (the camera is running at high recording rate). However, this novel lifetime-based technique sheds light on an interesting idea regarding to thermographic PIV: apart from Mie scattering, phosphorescence can also be used to perform PIV. Although there have been some previous studies on micro-PIV with luminescent tracer particles [36–38], most such studies were conducted in liquid with quantum dots. The study by Someya *et al.* [35] demonstrated the feasibility of combining the PIV system and two-color system into one, which can greatly simplify the experimental setup. The results from this study also implies that phosphorescence signal can be use to perform PIV in order to avoid reflection problems in a confined space, or to mitigate laser flare when performing PIV through a tube with a large curvature.

Despite the advantages and versatility of thermographic PIV on the multi-physics measurement, there are still several aspects which need to be further improved by future studies, summarized as follows.

- 1) Although thermographic phosphors with a ceramic host can sustain extremely high temperatures up to 2000 K, the emission becomes very weak beyond 900 K and can no longer be detected. The application of TPIV in a flame has not yet been successful. A recent study made an attempt to measure the gas temperature and velocity in a hydrogen diffusion flame [39]. However, the measurements were limited to regions where the gas temperature was lower than 900-1000 K, and a conclusion was drawn that TPIV was suitable for measurement in the low-medium temperature regions where fuel injection and mixing with hot exhaust gases occurred. Considering the cost and

experimental efforts spent on this technique, if it only works within a low-medium temperature range, then acetone LIF plus PIV may be a cheaper and easier surrogate to achieve the same goal. Therefore, extending TPIV to a higher temperature and to combustion studies is a primary task for the TPIV community.

- 2) In several recent studies [40–42], the problem of multiple scattering for TPIV was reported. This usually happens when excessive seeding is used, or when the optical path is long (a bulky seeded co-flow or cross-flow for example), and it could bias the temperature measurement. The mechanism of multiple scattering of phosphorescence signal may be more complicated than that of Mie scattering in a dense spray where this phenomenon was initially observed and named for, and it has not yet been fully investigated. Although the Structured Laser Illumination Planar Imaging (SLIPI) technique was adopted [42] to remove the multiple-scattering from the averaged image, it suffers from disadvantages such as a low signal to noise ratio and thus poor precision. Further investigations are needed for a better understanding on the multiple scattering mechanisms, and for improved approaches to remove the effects of multiple scattering.
- 3) The cost of commercial phosphor particles is usually very high ($> \text{£}700$ per kg), and the state-of-the-art synthesis method for many phosphor particles is time-consuming. Hence inventing a less expensive and faster synthesis method than the current Sol-Gel method to produce thermographic phosphor particles in large scale could also benefit the spreading of TPIV. The work by Gonzales *et al* [43] reported the detail procedure for the Sol-Gel synthesis of BAM:Eu²⁺ particles, and the cost turned out to be about one third of the commercial product. Other approaches to produce phosphor particles such as flame synthesis are also under study.

1.2 An overview of laser-induced fluorescence, phosphorescence, and incandescence

In the following chapters, three types of laser-induced emission from particle-based or molecular tracers will be frequently mentioned. They are *laser-induced fluorescence* (LIF), *laser-induced phosphorescence* (LIP), and *laser-induced incandescence* (LII). The first two belong to the category of photoluminescence which involves transitions between energy states, and the last one is essentially thermal electromagnetic radiation where the laser only serves as a heating source. They have been developed independently as diagnostic tools for combustion, fluid mechanics, and heat transfer applications. It is necessary to briefly introduce the principle of these emissions prior to describing the experiments.

Fluorescence and phosphorescence are closely related terminologies and are sometimes used interchangeably [11]. They are not necessarily related to the form of the tracer: solids can emit fluorescence such as Anthracene, which is used to produce red dyes; whereas gaseous tracers such as acetone and biacetyl can produce phosphorescence emission under UV excitation. Early literature classified these two phenomena according to their time scale: the fluorescence emission usually has a duration of 10^{-9} - 10^{-3} s, whilst phosphorescence lasts longer from 10^{-3} - 10^3 s. However, more recent findings have again proven such a simple classification is inappropriate. For example, ZnO emission only lasts for several nanoseconds following UV excitation, but it is usually regarded as phosphorescence. Many other phosphors also present an emission shorter than 10^{-3} s at elevated temperatures. Current photoluminescence studies separate fluorescence and phosphorescence by their transition modes. Figure 1.2 (adapted from [15]) shows the Jablonski diagram for the photoluminescence process. Fluorescence has a relatively simple mechanism: a photon is emitted when an electron drops from the excited state to a lower energy state. Unlike fluorescence, phosphorescence emission requires the excited electron to change its spin mode via intersystem crossing from the singlet state S_1 to triplet state T_1 before a photon can be emitted, as shown in the figure 1.2. This process is rare and theoretically unfavored by

kinetics (but is possible in quantum mechanics), hence it is usually called as the ‘forbidden’ transition.

Figure 1.2 is removed for the copy right reason. Copyright holder is A.H. Khalid

Fig. 1.2 Jablonski energy level diagram, adapted from [15].

Incandescence, however, is related to black body radiation. According to the Wien’s law, the spectrum of black body radiation peaks at a wavelength that is inversely proportional to the temperature. When an object is heated to a high temperature of several thousands Kelvin, the spectral peak of black body radiation falls into the visible regime and the emission intensity is roughly proportional to T^4 . Emitted light from the glowing object is known as incandescence. In soot measurements, high-power lasers are used to heat soot particles to the sublimation temperature, and the LII signal is recorded for measuring the soot volume fraction. Details of this technique will be introduced in Chapter 5.

1.3 Objectives

The primary objectives of this thesis is to:

- 1) Develop a simplified experimental setup for TPIV using only one PIV laser and two CCD cameras, and demonstrate the accuracy of temperature measurements and investigate the limit for such setup.
- 2) Investigate the application of SLIPI to non-linear phosphorescent emission by a numerical method.
- 3) Develop a TPIV technique for simultaneous temperature and velocity imaging in flames.

1.4 Thesis structure

This thesis consists of 7 chapters. They focus on the improvement of current phosphor-based TPIV and the development of TPIV for high temperatures beyond 1000 K based on LII signal.

Chapter 1 introduces the background of multi-physics measurement in fluids, particularly simultaneous temperature and velocity measurements, and the history of thermographic PIV. Other literature relevant to the topic for each chapter will be reviewed in the ‘Introduction’ section at the beginning of each chapter.

Chapter 2 demonstrates a simplified experimental configuration for thermographic PIV on a simple heated jet with only one laser and two cameras with ZnO tracers. A new calibration method is also described in this chapter to solve the dependence of intensity ratio to local excitation fluence.

Chapter 3 applies gas-phase phosphor thermometry to investigate a canonical heat transfer problem: jet impingement for surface cooling. The role of large eddies in heat transfer between an air jet and a heated surface is revealed by direct visualizing the vortical structures and the temperature field.

Chapter 4 discusses the effects of applying Structured Laser Illumination Planar Imaging (SLIPI) to Laser-induced Phosphorescence (LIP) on the temperature measurement by conducting a numeric study. The experimental data collected from ZnO emission is built into

the code of PIV image generator in order to mimic the SLIPI operation procedure with three modulated laser sheets. Several problems are identified for this novel application of SLIPI on LIP, and potential solutions are suggested correspondingly.

Chapter 5 introduces the concept of an entirely new thermographic PIV technique for high temperature measurements in a flame. The theory of this technique is introduced, and modeling is performed by adapting the traditional LII soot model.

Chapter 6 demonstrates the use of laser induced incandescence (LII) of submicron tungsten carbide (WC) particles as a method for particle image velocimetry (PIV). The technique allows a single laser to be used for separate measurements of velocity of two phases in a droplet-laden flow. The attempt of conducting this technique in a two-phase flame is also presented and discussed, where conventional methods are not applicable.

Chapter 7 presents a summary of conclusions, and plans the future studies on both phosphor-based and LII-based thermographic PIV.

Chapter 2

Simultaneous 2D, two-camera, thermographic PIV demonstration with ZnO tracers

2.1 Introduction

In this chapter, the possibility of using a double-pulsed UV light source (UV-PIV system) and two non-intensified CCD cameras to implement thermographic PIV is demonstrated. Although in general it should be possible to capture the Mie scatter at 355 nm instead of the phosphorescence signal, the quantum efficiency of most (inexpensive) PIV cameras such as used in the present experiment is low at 355 nm, and most commonly used camera lenses have low transmissivity for UV light. Alternatively, it may also be possible to use the residual 532 nm if the laser has sufficient energy. The present approach focuses on using the phosphorescent signal for both PIV and LIP.

For purposes of demonstration, easily obtainable ZnO particles were selected as tracer particles for both thermography and velocimetry, as it displays high temperature sensitivity [44] and short decay-time ($< 1 \mu\text{s}$) [45] within 300–500 K. According to [44], most commercial ZnO contains some level of impurities that can serve as an activator for phosphorescent emission, and its photo-luminescent behavior is similar to commercial phosphor ZnO:Zn

in which Zn is deliberately added as a dopant. The use of ZnO is limited to temperatures lower than about 500 K, as the phosphorescence signal becomes too weak to be captured by a CCD camera. However, the same principles used in the present technique are transferable to fast-decay phosphors such as BAM:Eu²⁺, which yield suitable signal at higher temperatures, at sufficiently short decay times.

In this chapter, the experimental setup is described in Section 2.2, followed by the in-flow calibration of the signal in Section 2.3, including a method for correcting for effects of laser fluence non-uniformity on the intensity ratio. Instead of the normalization method proposed in [44], the calibration was conducted at different pulse energies and the corresponding laser profiles were measured, hence the local laser fluence was introduced into the calibration function. Sections 2.4, 2.5 and 2.6 show a demonstration of simultaneous temperature and velocity measurements based on the obtained calibration function. Sections 2.7 and 2.8 are the conclusions and afterthoughts to this study.

2.2 Experimental setup

2.2.1 Flow system

For both calibration of ZnO and thermographic PIV demonstration, an air jet of 7.2 mm diameter was used. The flow rate was 40 slpm at room temperature, controlled by a mass flow controller (Alicat MCR-250SLPM) for a bulk jet velocity of 17 m/s at standard conditions, and jet Reynolds number of $Re = 8000$. A co-flow of 0.4 m/s over a surrounding diameter 80 mm shielded the jet from ambient air. The jet was heated by rope heaters (Omega FGR-100) wrapped around the tube, providing a maximum outlet temperature of about 450 K for this flow rate. In-line heaters could not be used in this experiment, as aggregates of ZnO particles were found to stick between the coils and block the flow.

The ZnO particles (Sigma-Aldrich 96479) were heated to 120 °C and dried for 8 hours in an oven before the experiment. Unlike several commercial phosphor particles used in previous literature, ZnO particles ordered from Sigma-Aldrich were not coated with anti-agglomeration agents. Although the primary particle size of this product was reported to be

about 200 nm and most aggregates measured approximately 1-2 μm [44], a few aggregates of much larger size ($>20 \mu\text{m}$) could still be observed even after a long drying time, probably due to inter-particle forces. These large aggregates can result in error for both temperature and velocity measurements due to its long temperature response time [16] and non-negligible particle slip. Hence they were removed from the images during the preliminary processing stage.

ZnO particles were dispersed into the jet by a seeder (Texas Airsonics AJ-1), in which particles are fluidized by a vibrator. For this seeder, the minimum flow-rate that could efficiently seed particles into the jet was about 30 slpm, below which the particle seeding density was too low to produce a detectable signal. The co-flow was not seeded with particles due to the limited flow rate of the available seeders. This of course biases the velocity and temperature measurements in favour of the seeded flow, and prevents measurements further away from the mixing layer of the jet.

2.2.2 Optical system

The optical system is illustrated in Fig. 2.1. Typical dual-cavity lasers for PIV irradiate at 532 nm wavelength, while Nd:YAG lasers that can produce UV light generally deliver a single pulse per flashlamp pulse. This is one of the reasons why all previous studies have used two separate laser systems for LIP and PIV respectively. The laser used in the present study is a Nd:YAG laser (Continuum, Surelite III) operating with a third harmonic generator which produces pulsed illumination at 355 nm. Although the laser only has one cavity, it can produce two laser pulses each time by enabling the laser Q-switch to be opened twice during one flashlamp discharge, and the total energy is evenly distributed to each pulse by adjusting the Q-switch delay time [46]. However, this double pulse mode is optimized for pulse separation $\Delta t = 60 \mu\text{s}$, based on the instruction provided by the manufacturer. The total energy of two pulses decreases drastically as Δt deviates from this optimized value. In the experiment the laser was operated at 10 Hz and the pulse separation was chosen as $\Delta t = 30 \mu\text{s}$. This represented a compromise between suitable spacing for the range of velocities sought, yet sufficiently high energies to excite the fluorescing particles. A photodiode (PD)

was installed to monitor the energy of each pulse. The position of the PD was fixed during the calibration and all experiments to enable the correlation between PD signal and pulse energy.

Four lenses were used to form a collimated laser sheet. The combination of FL = -25 mm and a FL = 150 mm cylindrical lenses produces an approximately 40 mm tall non-diverging laser sheet. A following combination of FL = 150 mm and FL = -25 mm cylindrical lenses reduced the thickness of the light sheet. The thickness of the formed laser sheet above the jet nozzle was about 0.3 mm. A slit was used to remove the top and bottom edges of the laser sheet, where the intensity was too low for robust signals, resulting in a final height of the light sheet of about 35 mm. Unlike in previous studies, a collimated rather than diverging light sheet was used to obtain thermographic PIV for two reasons. First, the intensity of phosphorescence is generally much weaker than that of Mie scattering, so that a high laser fluence is preferred to excite phosphor particles before they are saturated. Second, neglecting light absorption by ZnO particles, the laser fluence distribution F of a collimated laser sheet is a function of the vertical direction z and can be measured easily. As shown further on, considering the intensity ratio of the fluorescence emission by the phosphor particles is slightly dependent on laser fluence, so that measurements of temperature require a correction based on the local laser light intensity.

Phosphorescence emitted from the seeded particles was imaged by two non-intensified low-speed PIV cameras (LaVision Imager Pro X 4M) both fitted with a AF Micro Nikkor 60 mm lens (f/2.8D). A 387 ± 5.5 nm interference filter (Edmund Optics 84094) and a 425 ± 25 nm filter (Edmund Optics 86961) were installed in front of cameras A and B respectively. The combination of these two filters was used in [44] and shown to yield high temperature sensitivity. A 50 mm diameter 50:50 beam splitter for UV light (Edmund Optics 48192) was mounted in front the cameras to separate the phosphorescent emission. During the calibration of ZnO, the setup was running in single-pulse/frame mode, and the exposure time was set to 90 ms, see timing diagram (a) in Fig.2.2.

For thermographic PIV demonstration, the laser was operated in double-pulse mode, and the exposure times of the two images were $5 \mu\text{s}$ and about 50 ms, for the first and second

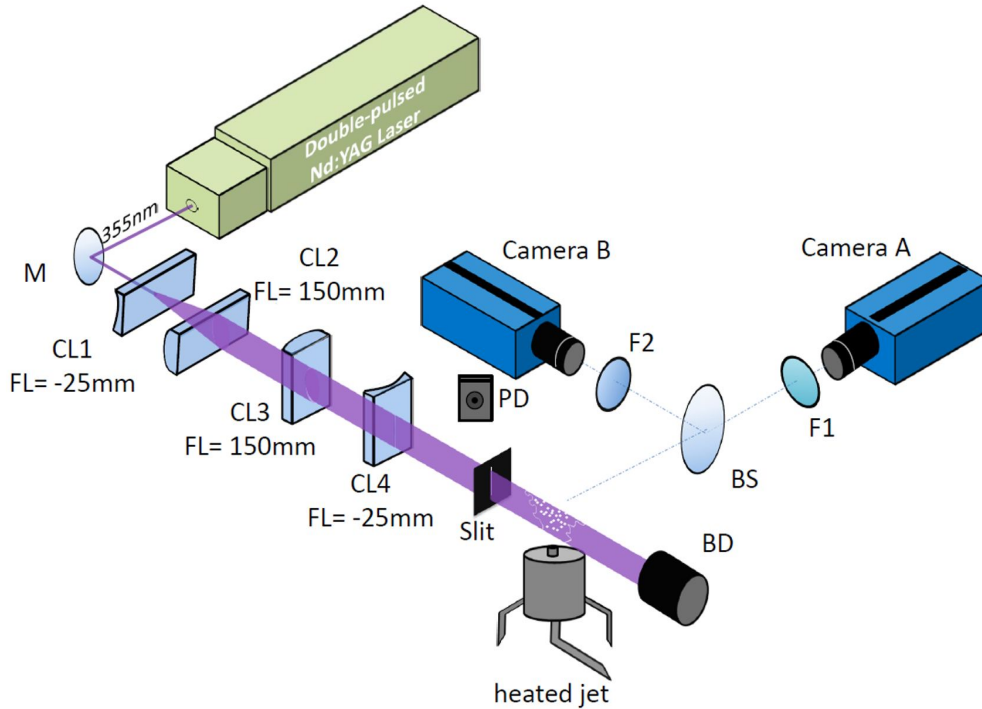


Fig. 2.1 Experimental setup. BD: beam dump; BS: beam splitter; CL: cylindrical lens; F: short band pass filter; FL: focal length; M: mirror; PD: photodiode. Cameras are non-intensified.

pulse, respectively. The minimum time on the first image is limited by the readout time for the first frame, as shown in timing diagram (b), and the second exposure time cannot be controlled. In the present experiments, the exposure times for ZnO calibration are set to a different value than that for thermographic PIV demonstration. However, there is negligible noise between the end of ZnO emission (of order of several nanoseconds) and the end of exposure, so that should not affect the results. However, for applications to flames, the exposure time for the calibration and actual experiment should be short and of the same order of the decay time, to avoid collection of undue flame luminosity during the interval.

In order to minimise the write out time and allow a sensible exposure time (or collection frequency) of 5 Hz, the experimental image was set to 1504×1024 pixels, corresponding to a $33.2 \text{ mm} \times 22.6 \text{ mm}$ field of view and a pixel resolution of $22.1 \mu\text{m}$, according to the calibration using a target placed at the jet position. No hardware or software binning was applied. Many previous studies, such as [16, 30, 44], used hardware binning to improve the signal to noise ratio. However the downside of binning is the severe loss of spatial resolution.

In the present study, no binning was applied to the raw images, because the measurements were conducted in the temperature range where the signal to noise ratio was reasonably high. The decision to perform in-chip or off-chip binning depends on the particular experimental conditions, *i.e.* whether SNR or resolution is most important.

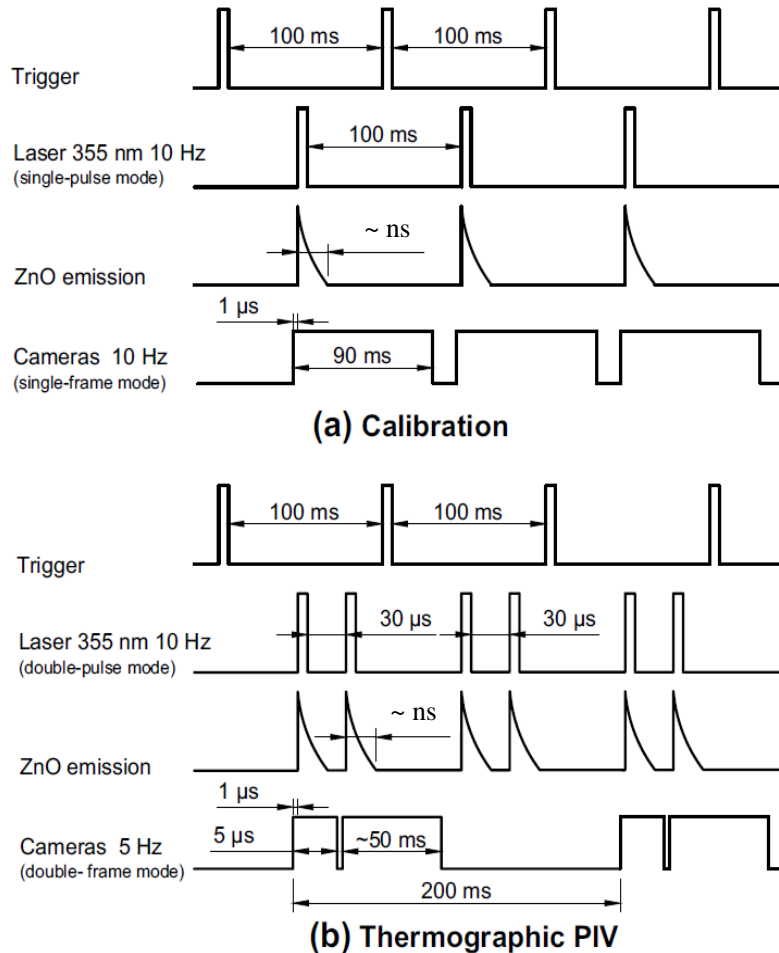


Fig. 2.2 Timing diagram for (a) calibration of ZnO; (b) thermographic PIV measurements. The camera shutter opens 1 μs prior to the laser pulse in case of laser jittering. The diagram is not scaled to the actual time annotated.

The image pairs recorded by the first frames at time t and the second frames at time $t + \Delta t$ were used to calculate the intensity ratio, while the two consecutive images recorded by each camera were used to produce the cross-correlation to calculate the velocity, as illustrated

by sample images in Fig. 2.3. Although of course using the same camera for PIV and LIP can be desirable, this must be tempered by a trade-off: the strong PIV signal must be stopped down to a small aperture to avoid pixel-locking, yet the phosphorescence requires large aperture for high signal. The user must therefore perform controlled experiments to make sure experiments are not contaminated by pixel locking. For temperature imaging, the two images in a pair recorded by different cameras need to be overlapped exactly in order to determine the ratio. Translation stages were used to roughly adjust the position of two cameras before the experiment to guarantee that the shift of raw images was less than 10 pixels. Further image mapping was implemented by a program that shifts and rescales the images recorded by camera A and overlaps it onto the images recorded by camera B. The final overlap difference between two images was less than 1 pixel. For PIV, the two consecutive frames recorded by camera B were preferred because the quantum efficiency of CCD sensors are maximized within visible wavebands, and thus images recorded by camera B show a higher signal to noise ratio. Since the decay time of ZnO is shorter than 1 μ s, particle images do not appear as streaks on either frame.

2.2.3 Timing optimization

The timing interval selected is a compromise between the following requirements: (a) a suitable mean displacement of the particles Δx to maximize the correlation peak detection probability, typically set to no larger than one-quarter of the interrogation window D_I , $\Delta x = U\Delta t \leq \frac{1}{4}D_I$, (b) a large enough energy per pulse delivered by the double pulsed Q-switch, which has an optimum timing to produce reasonably equal energies for both pulses, and (c) a suitably large flow rate and resulting bulk velocity U for the flow which produces sufficiently large seeding rate of particles. Figure 2.4 shows qualitatively how the signal and figures of merit vary with the chosen time interval. For the present system, using an interrogation window of 64×64 pixels, corresponding to a displacement $D_I = 1.4$ mm, the window of optimization produced a compromise of 40 slpm flow rate for a flow velocity of $U = 23$ m/s at 410 K and 30 μ s pulse separation. This produces a ΔX of about half the interrogation volume, rather than one-quarter. However, the relatively high particle number

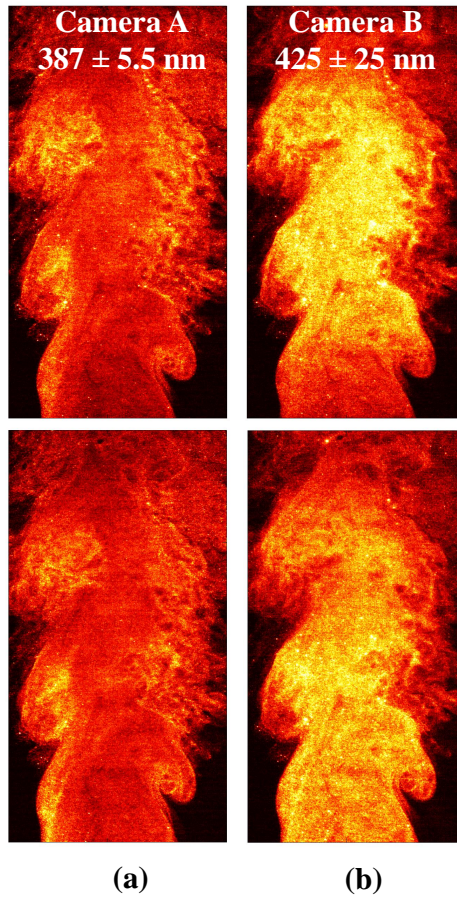


Fig. 2.3 Single-shot intensities of first and second frames obtained with Cameras A and B at two different wavelength ranges as indicated. Upper row: first frames recorded at time t ; bottom row: second frames recorded at time $t + 30 \mu\text{s}$. Images in the same row were used to calculate intensity ratio. Images on the right column were used to perform cross-correlation for PIV.

density at the selected flow rate can partially compensate for the effects of out-of plane loss of particle images [47, 48], so that acceptable 2D velocity measurements can still be achieved.

2.3 Calibration

2.3.1 ZnO calibration curves as a function of laser intensity

Calibration of ZnO fluorescence signal was conducted in the same jet flow for various temperatures ranging from room temperature to 424 K. Prior to the phosphorescence imaging, a K-type thermocouple of 0.5 mm diameter was placed in the jet core 5 mm above the nozzle

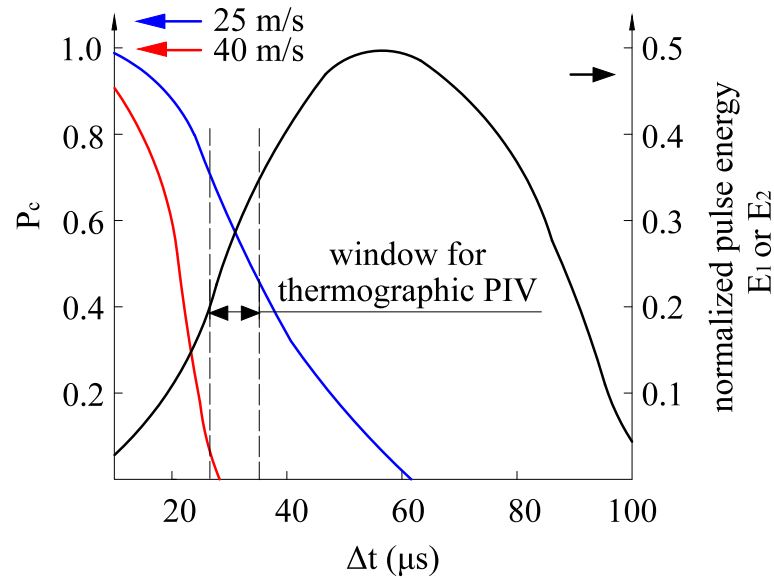


Fig. 2.4 Schematic variation of normalized laser energy per pulse, probability of finding cross-correlation P_c , as a function of timing interval Δt between images. For PIV, the total energy was evenly distributed between the two pulses ($E_1 = E_2$). The particle seeding density, and hence the signal intensity, is proportional to the flow rate passing through the seeder.

to record the mean temperature, in a central region where the flow was stable. The exposure time of both cameras, operated in single-image mode and synchronized with the laser pulse at 10 Hz, was set to 90 ms. Since the intensity ratio of ZnO has been reported to be dependent on laser fluence, six levels of pulse energy were tested for each temperature. The mean pulse energy integrated over the whole region was measured (2.8, 6.4, 8.6, 11.6, 15.8, 34.6 mJ) at each energy level for over 900 pulses by a powermeter placed at the jet position. For each condition, the intensity ratio was measured over the probed region and averaged spatially, over a $1.1 \times 1.1 \text{ mm}^2$ square region shown in Fig.2.5(a). The local and mean ratio was calculated for a total of 600 images. For 2.8 mJ pulse energy, the average signal to noise ratio in the square region is only about 2.0, which is too weak and would result in large errors. Hence only higher energy levels were considered, as reported in in Fig.2.5(b). The curves obtained show some discrepancies relative to those ones reported in [44], possibly due to the use of a different beam splitter with a higher reflectivity for near UV light, and the use of higher laser fluences.

A key issue in producing a robust calibration is the solid aerosol be as monodisperse and uniform as possible, and that the reference be obtained at similar conditions. The phosphorescence effect is a surface phenomenon, and its effectiveness is subject to the surface to volume ratio of the particle. As in many surface phosphorescence techniques, there is no expectation that the details of energy transfer will be entirely predictable for particles of different microscopic characteristics, so that calibration at relevant conditions is essential.

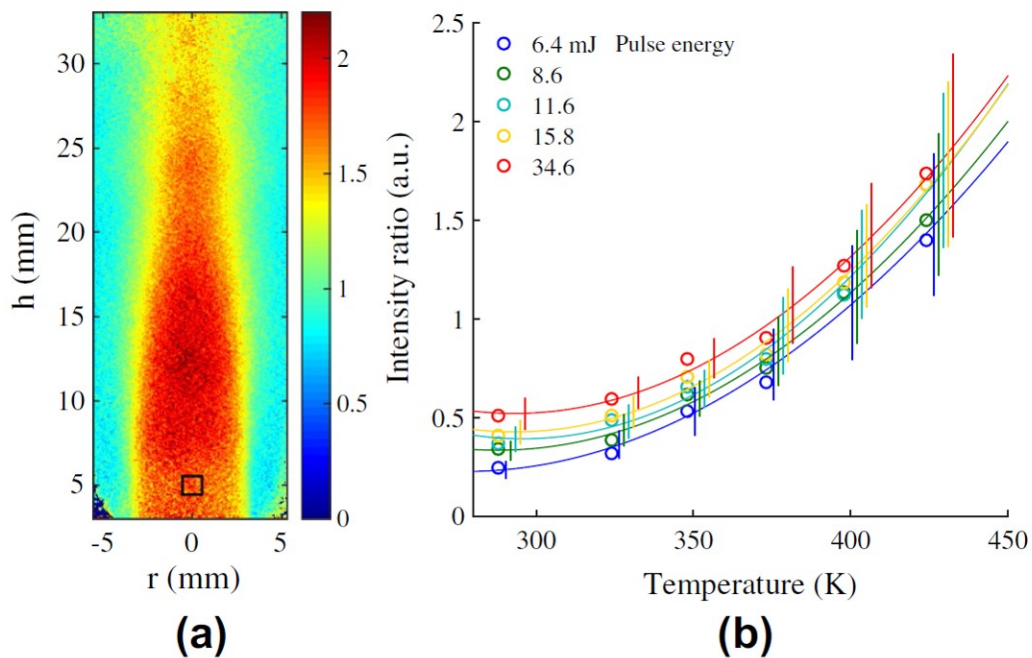


Fig. 2.5 (a) Mean intensity ratio of signal over wavelength range 450 ± 25 nm to that at wavelength range 387 ± 5.5 nm for a total laser energy of 8.6 mJ at a temperature 424 K in the marked region; (b) mean intensity ratio of the square region shown in (a), as a function of temperature and mean laser pulse energy (mJ). Intensity ratio variances are presented as vertical error bars. Lines are second order polynomial fits for each energy.

The measured intensity ratios are an increasing function of temperature, and a weak function of the laser pulse energy. The weak dependency on laser energy is probably caused by two reasons: the particle absorption and the change of luminescence characteristics of ZnO due to increasing excitation fluences [44]. In order to eliminate the effects of nonuniform spatial distribution of laser fluence, Abram *et al.* [44] suggested that the dependence of the measured intensity ratio on fluence disappears once it is normalized by the room temperature

intensity ratio. However, the fluence range they applied was 5-20 mJ/cm², and a 7.2 K error caused by such normalization was reported at 475 K. Since a non-diverging Gaussian laser sheet was used in the present setup, in our case a much larger span of laser fluences (20-213 mJ/cm², see section 3.2) was applied to excite the particles. Hence, to achieve a better accuracy, instead of using the normalization method, the local laser fluence F is measured and introduced into the calibration function:

$$I_r = I_r(T, F) \quad (2.1)$$

where I_r is the intensity ratio, T the temperature, and F is the local laser light fluence at the calibration point. However it should be noted that the flat-fielding correction also compensates the error sources brought by laser extinction and absorption, which cannot be achieved by the present calibration method. If laser extinction do exist in this case, it will bias temperature measurement at the far side, as the laser fluence gradually decreases when passing through the seeded flow. However, from the averaged image obtained from the experiment, no obvious decay of emission intensity is observed along the incident direction of laser light. This suggests current seeding rate does not cause severe laser attenuation.

2.3.2 Laser sheet profile

The local laser light fluence varies along the axial direction according to the laser light profile, denoted as $F(z)$. The mean laser sheet profile $F(z)$ along the axial distance z was measured by exciting diluted laser dye Coumarin 460 in a cuvette and imaging the fluorescence (435-485 nm) using camera B. In order to avoid saturation of the dye, the laser sheet was attenuated to approximately 1% of original energy by using two pieces of glass and a prism. The mean laser intensity profile obtained over the highlighted rectangle shown in Fig. 2.6(a) was averaged over 900 shots. The laser intensity profile is assumed to be proportional to the fluorescence intensity obtained. Given the measured mean pulse energy (mJ) and the thickness of the laser sheet (0.3 mm), the intensity profile can be translated into laser fluence

(mJ/cm^2), as shown in Fig. 2.6(b). Corresponding laser fluences at the calibration point for the five energy levels are 20, 33, 51, 76, 213 mJ/cm^2 , respectively.

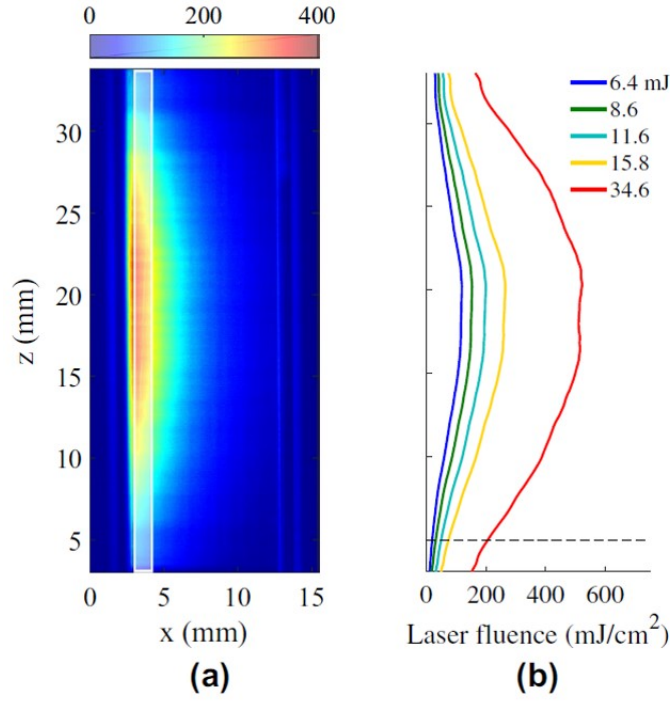


Fig. 2.6 (a) Fluorescence from excited Coumarin 460 in a cuvette as recorded by camera B; (b) fluence obtained from highlighted region (1504×50 pixels) in (a) and the measured mean energy (mJ/cm^2) for varying energy levels. The dashed line indicates the center of the calibration region, with corresponding to fluences of 20, 33, 51, 76, 213 mJ/cm^2 .

2.3.3 Final calibration function

The calibration function $I_r = I_r(T, F)$ was finally obtained from the ratio of signals obtained in the region of interest shown in Fig.2.5(a), and the local fluence obtained at the same location by using the profile in 2.6(b). The plot of $I_r(T, F)$ is shown in Fig.2.7. The intensity ratio grows slowly for a fluence above 80 mJ/cm^2 , which matches well with the result reported in [44]. The calibration function was extrapolated to $F = 250 \text{ mJ}/\text{cm}^2$, in case the maximum laser fluence during the thermographic PIV demonstration falls beyond the calibration range. The final calibration grid was refined to $0.1 \text{ mJ}/\text{cm}^2 \times 0.1 \text{ K}$ by interpolation. The surface

shows a distortion at higher temperatures and low laser fluences, owing to the low signal to noise ratio and was avoided during the experiment.

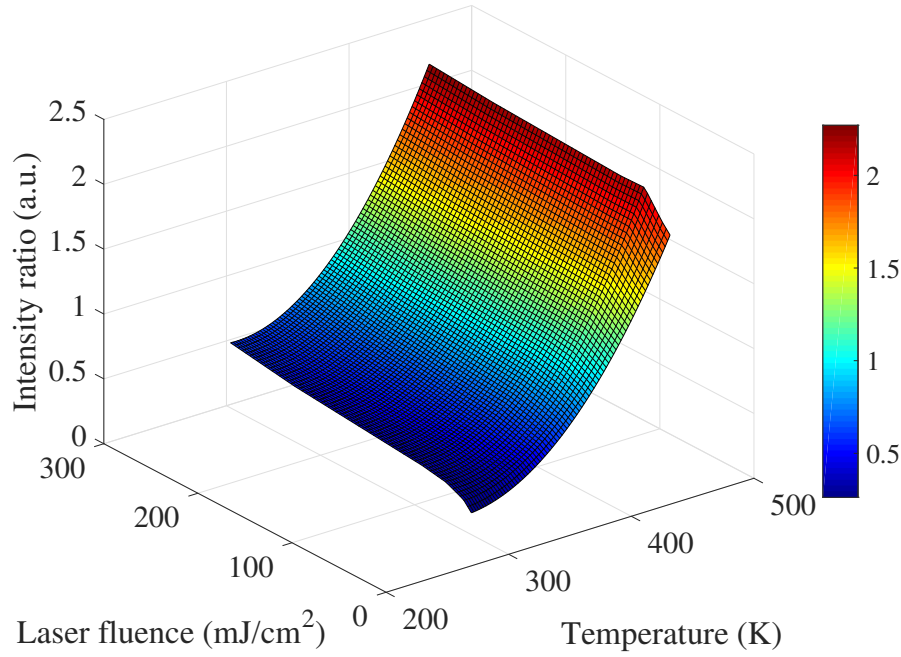


Fig. 2.7 Calibration function $I_r = I_r(T, F)$

2.3.4 Laser sheet profile for double pulse mode

Since we can use either the first or second pulse to obtain the intensity ratio, it is necessary to characterize the local laser fluence for both the first and second laser pulse. The laser fluence profiles $F(z)$ measured for both pulses are shown in Fig.2.8(a). During the experiment, the energy released by the flashlamp charge also fluctuates from pulse to pulse. If the normalized mean shape function of the fluence profile $\hat{F}(z)$ remains the same for all individual pulses, the fluence profile for an instantaneous profile $F(z)$ is assumed to be proportional to the mean profile $\hat{F}(z)$, and proportional to the total energy of the pulse E :

$$F(z) = \frac{E}{\bar{E}} \hat{F}(z) \quad (2.2)$$

where \bar{E} is the mean energy over all laser pulses, and E is the energy of individual pulse, both of which are monitored by the PD. The measured temporal energy fluctuations of the first pulse and the second pulse are about 15% and 12% respectively. Fig.2.8(b) shows that the normalized shape function $\hat{F}(z)$ does not change significantly from pulse to pulse, even though the pulse shapes are different. The single-shot intensity ratio obtained in this manner was translated into temperature according to the calibration function $I_r(T, F)$ and the local mean laser fluence for the first or second laser pulse.

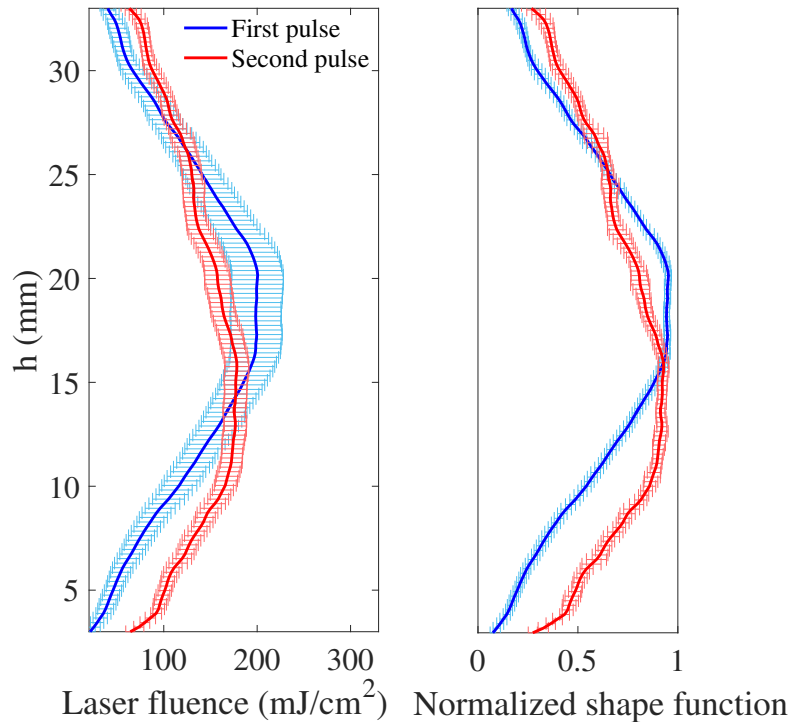


Fig. 2.8 (*left*) Laser fluence profile $F(z)$ for the first (blue) and second (red) pulses; (*right*) normalized shape function of the fluence profile. Averages represented by the solid line, standard deviation by the error bars.

2.4 Operating conditions

A flow rate of 53 slpm of air for a bulk velocity of 23 m/s at a measured outlet temperature of 410 K, was used to generate the test flow field of a jet mixing layer. The two cameras were

running in double-frame mode at 5 Hz, a frequency that was limited by the storage speed. A total of 900 double-frame images were recorded by each camera. The temperature results obtained by thermography were compared to a traverse of a thermocouple at 5 and 10 mm above the jet nozzle.

2.5 Data processing

2.5.1 Thermography

Data processing for 2-color thermography was completed by a Matlab program. The background image was recorded and subtracted from all raw images and a 5×5 pixel moving average filter was used to increase the signal to noise ratio and smooth the image, resulting in a spatial resolution of $110.5 \mu\text{m}$. A threshold of 10 counts was considered as the threshold of noise to be removed from the images, for a maximum signal of 5000 counts (large aggregates) and mean signal intensity of about 300. In most of the raw images there are a few large aggregates, whose intensity appears significantly higher than those of small particles. The intensity ratio of these large aggregates is also higher than the surrounding intensity ratio, as illustrated in Fig.2.9(a), because the temperature response time of large particles is significantly longer than for the small ones[16]. To remove the large aggregates, all pixels with intensity higher than 500 counts in the raw images were removed, and the corresponding regions excluded from the processing. The resulting intensity ratio field is shown in Fig.2.9(b), where the edge of large aggregates can still be seen due to diffraction. The area removed was extended by 3 pixels outwards to remove the diffraction of those large aggregates, as shown in Fig.2.9(c). The values for the removed regions were determined by interpolation, Fig.2.9(d). We note that the problem of large aggregates is less likely to happen if commercial coated phosphor particles are used.

After large aggregates were removed from raw images, the intensity ratio field was translated into temperature via the following process: the laser fluence profile for each pulse was calculated from the mean fluence profile and the individual pulse energy recorded by the PD based on Eq.(2.2); the laser fluence corresponding to each row of pixels was extracted

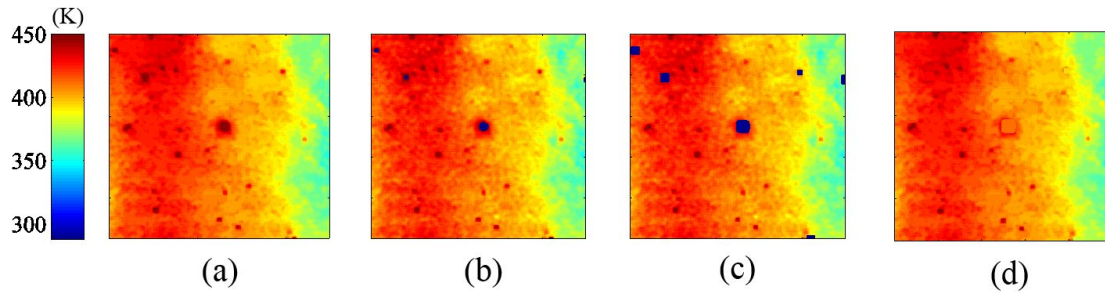


Fig. 2.9 Resulting sample temperature fields (K) after each image processing step for removing large aggregates. The area of the shown region is 150×150 pixel (3.3×3.3 mm)

from the profile, and the closest value I_r to the measured intensity ratio was searched to determine the temperature. The main advantage of this data processing method is that the laser fluence does not need to be uniform, but the data processing time is long (approximately 4 minutes per image).

2.5.2 Particle image velocimetry

The phosphorescence in the 400–450 nm bandwidth was recorded by camera B and used for cross-correlation for PIV, as the CCD sensors are much less effective for the lower selected spectral line (381–393 nm). However, the signal to noise ratio of the phosphorescent PIV images is significantly lower than PIV images recorded at 532 nm, and the resulting detectability of cross-correlation peak can be relatively poor. The most efficient way to increase pixel intensity under the present conditions is to increase the seeding density, as the former is a linear function of the latter [27]. Hence an efficient seeder that can provide enough particles dispersed into the flow is essential for high quality cross-correlation of phosphorescent PIV image pairs. However, it should be noted that the high seeding density can also cause multiple scattering effects and bias the temperature measurement [22, 27, 41], hence there is a compromise between guaranteeing a sufficiently high signal-to-noise ratio and avoiding severe multiple-scattering effects.

The images were processed by the Davis 7.2 software from LaVision. Vectors were calculated using a multipass cross-correlation, with a constant 64×64 pixel window size

and an overlap of 75% in three passes, which gives 91×61 vectors in total. Vectors with a Q-factor below 1.2 were removed, and a 3×3 pixel moving average filter was applied to smooth the vector field. The final nominal vector spatial resolution is approximately 0.37 mm/vector.

2.6 Results and discussion

2.6.1 Temperature imaging

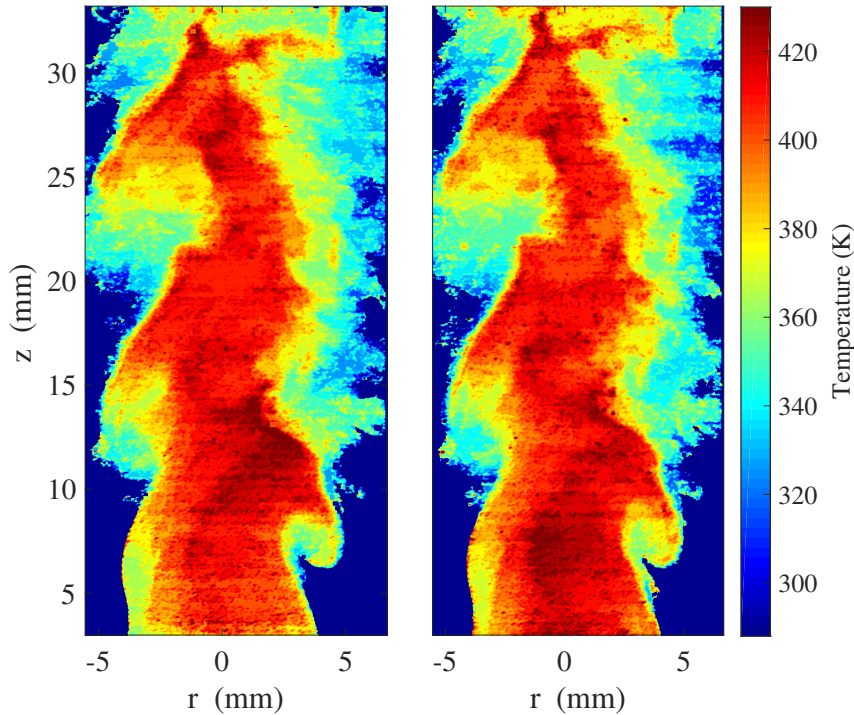


Fig. 2.10 Example single shot of temperature field at time t (left) and $t + 30 \mu\text{s}$ (right) based on calibration function $I_r(T, F)$.

Figure 2.10 shows single shot 2D temperature fields extracted from the calibrated and corrected image ratios for times t and $t + 30 \mu\text{s}$. The entrainment structures can be observed clearly and the temporal change of temperature field during the time interval is also clear by comparing the two frames. The horizontal streaks are a result of CCD charge transfer noise.

This was confirmed, as the streak direction changed 90 degrees for a corresponding different camera orientation.

Figure 2.11 shows the mean temperature fields over the first and second frames. To eliminate the effects of CCD transfer noise, the mean temperature fields were smoothed by a 30-pixel (0.66 mm) 1D moving average filter along the vertical direction. The images on figure 2.11, the temperature on the left half of the jet appears higher than the right half. This could be a result of laser light absorption, as the laser beam is emitted from left to the right on the figure: the absorption can affect the local particle temperature, as well as the local fluence on the far side of the laser sheet. However, as remarked further on, the temperature field measured by the thermocouple is not entirely symmetric, and that accounts for part of the difference. The two frames appear slightly different. This is probably due to the non-top-hat laser sheet, which leads to different SNR and laser heating effect along the axial direction.

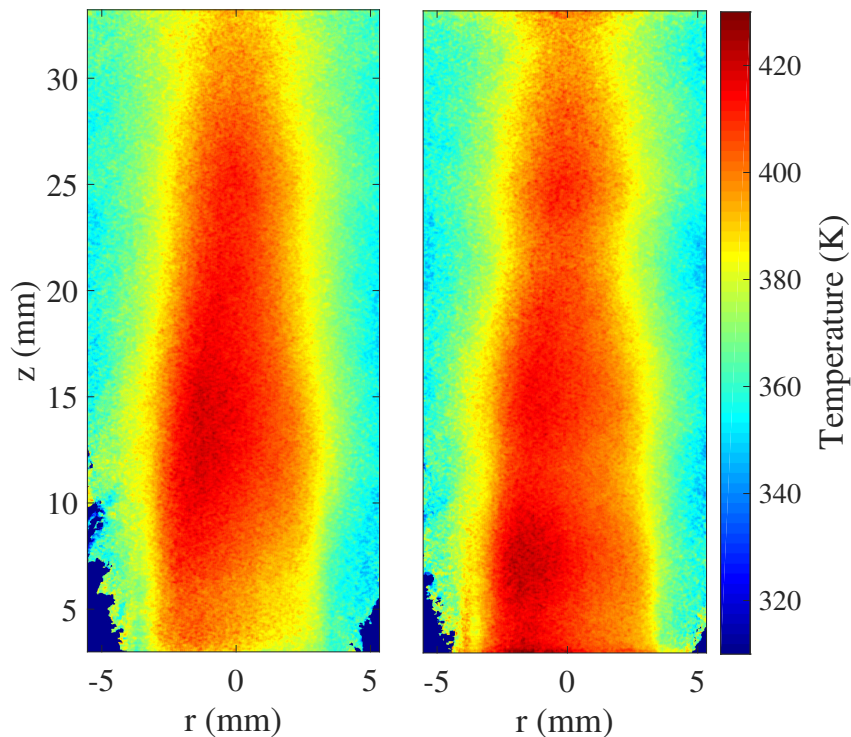


Fig. 2.11 Mean temperature field obtained for the first pulse at time t (*left*) and second pulse at time $t + 30 \mu s$ (*right*). The laser sheet enters from the left side. To eliminate the effects of the CCD transfer noise, the mean temperature fields were smoothed by a 30-pixel (0.66 mm) 1D moving average along the vertical direction.

A comparison between the mean thermographic results and an average thermocouple sweep is shown in Figure 2.12. The profile measured by the thermocouple is not symmetric, and the maximum temperature appears 1 mm to the left of the geometric centre of the jet. The heating was generated by wrapping tape heaters around the tube, so that it is possible that the heat transfer rate might not have been uniform. Results show that for an axial distance 10 mm from the base of the jet, the temperature profiles extracted from both frames are in good agreement with that measured by the thermocouple. The discrepancy increases on both sides because of the increasingly poor signal to noise ratio due to dilution of the seeded jet by the unseeded co-flow. In a turbulent flow, this biases the mean temperature measured by the thermographic measurements towards the hot side of the jet, as the probability of signal from the seeded hot region is larger than that of the unseeded part. At an axial distance of 5 mm, the temperature profile processed from the first frame is biased to a lower value. The reason for the temperature bias is probably due to the low laser fluence (see Figure 2.8(a)) and thus the poor signal to noise ratio at this height in the first frame.

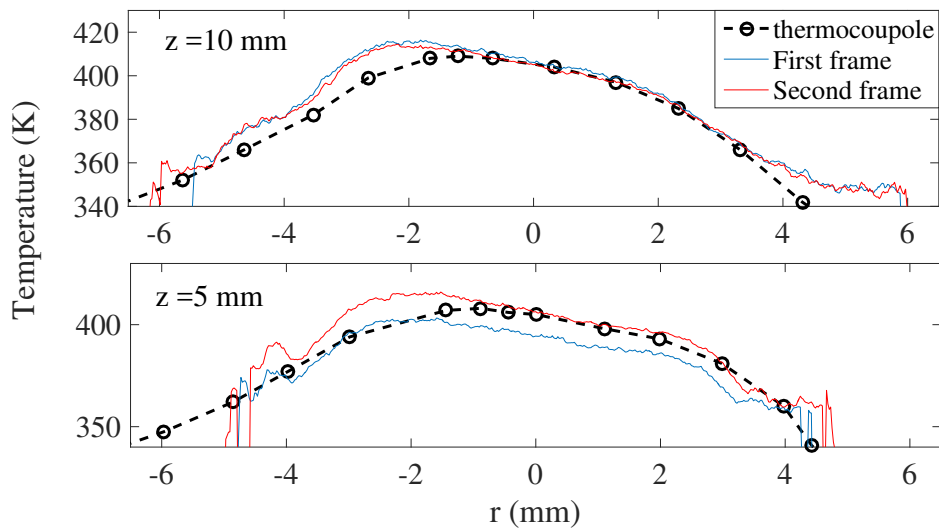


Fig. 2.12 Mean temperature profiles processed from the first frame (*red*) and the second frame (*blue*), compared to values measured by a thermocouple (*dashed line with circles*) for an axial distance 10 mm (*top*) and 5 mm (*bottom*).

The root mean square of the temperature field processed from the first and the second frames are shown in Figure 2.13. In the core region, the temperature rms is estimated as 15

K for a 410 K outlet temperature. The high fluctuation on the outer zone is clearly because of the combination of low signal to noise ratio due to particle dilution, combined with the actual high variance due to turbulent mixing. The high values at the bottom of the image arise due to the lower fluence. Better quantification of the rms should be made by seeding the outer flow for more uniform signal to noise ratio.

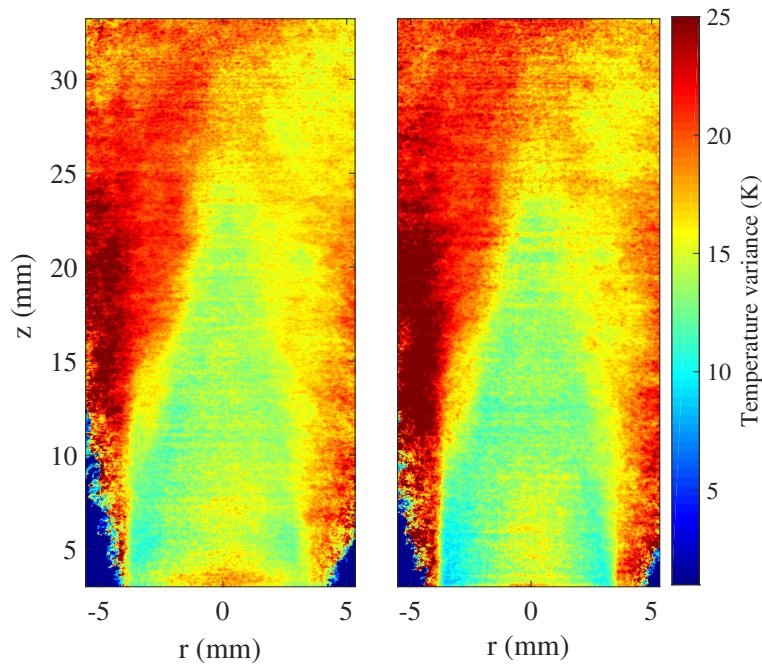


Fig. 2.13 Temperature rms processed from the (*left*) first frames; (*right*) second frames at $t + 30 \mu\text{s}$.

2.6.2 Simultaneous velocity and temperature imaging

Figure 2.14 shows two sample images of simultaneous temperature and velocity fields. The white contour on Figs.2.14(a)(c) corresponds to the 2D vorticity calculated based on the velocity field shown in (b)(d). The vorticity contours match well with the expected entrainment structures, and the velocity field shows similarities to the temperature field, as expected for a heated simple jet. In figures 2.14(b)(d), there are some empty zones where the vectors were removed, as the quality factor was lower than 1.2, with the presence of spurious vectors which significantly deviated from its surrounding vectors (see Fig.2.14(b)). The uncertainty in velocity measurements arises due to: (i) long pulse separation due to the

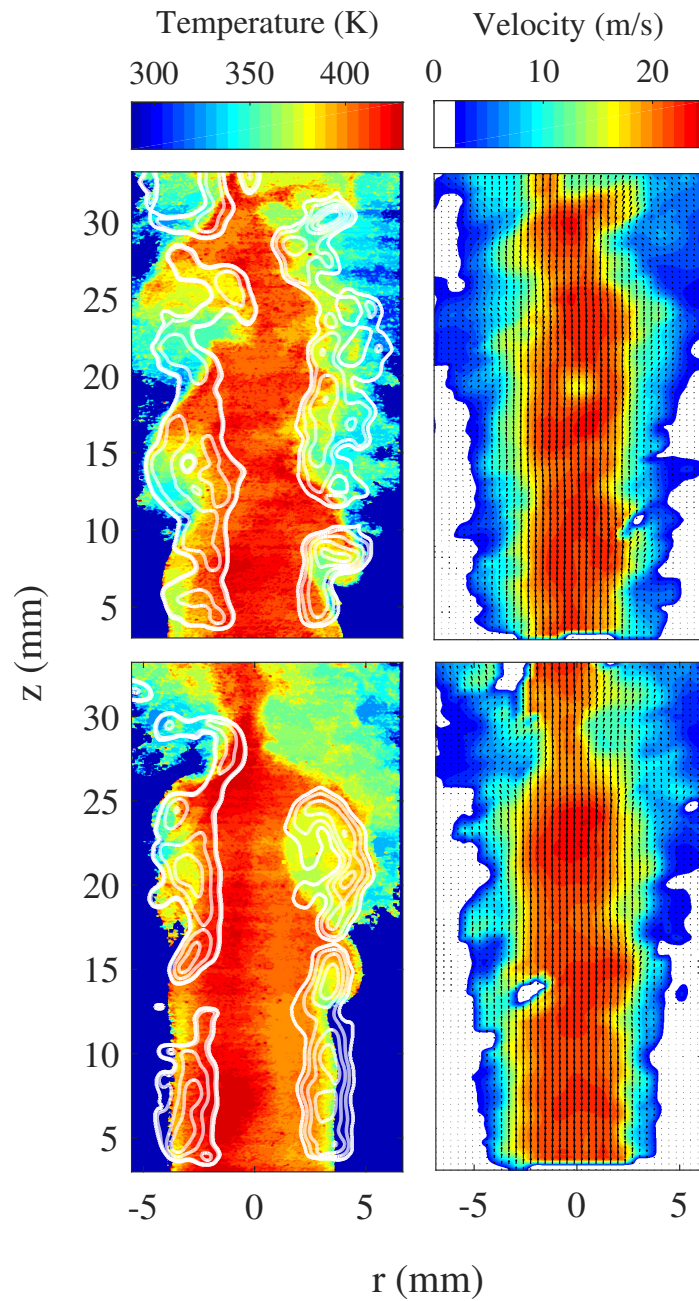


Fig. 2.14 Two examples (*top and bottom*) of simultaneous temperature (*left column*) and velocity (*right column*) imaging. The vorticity contours are superimposed onto the temperature field. As expected, the temperature structures show similarities to the velocity structures.

optimization of laser energy: this limits the detectability of cross-correlation peaks, (ii) the presence of large aggregates which cannot fully follow the flow, and (iii) low particle number density in the mixing regions. The first factor can only be improved by using a two-cavity PIV system with a third harmonic generator, while the remaining two can be solved by using coated particles and seeding the co-flow as well.

In general, separating the PIV and LIP measurement by using more lasers and cameras makes the system more flexible: (a) the SNR of the PIV image becomes independent of the phosphorescence emission and thus does not depend on temperature, (b) pixel-locking can be more easily avoided, and (c) higher temperatures can be detected by LIP, as hardware binning can be applied. There is however a compromise between the cost and the versatility of the system. The results shown here demonstrate that the concept can realise temperature and velocity images at low cost, without sacrificing too much in accuracy and dynamic range for both velocity and temperature.

2.7 Summary

Simultaneous 2D temperature and velocity measurements were demonstrated by thermographic PIV based on ZnO particles, using a single laser, and two non-intensified cameras. Phosphorescence from excited ZnO particles was proved to be suitable for conducting PIV, and hence the experimental setup was to a large extent simplified comparing with previous studies [16, 29–31]. A single-cavity YAG:Nd laser installed with a third harmonic generator was operated in double-pulse mode (enabling the Q-switch twice during one flash-lamp charge) and two non-intensified CCD cameras were running in double-frame mode to record the phosphorescence signal, eliminating the need of using another PIV laser at 532 nm and an extra camera for recording the Mie scatter.

To compensate for the effects of laser fluence on the intensity ratio, a non-diverging laser sheet was arranged, and the profiles of the laser sheet were measured for both calibration and experiments. Calibration was conducted at various temperatures and different laser energies, to yield a calibration function of intensity ratio to temperature and laser fluence $I_r(F, T)$. The

intensity ratio field was transferred into temperature according to $I_r(F, T)$ and measured local laser fluences F . A comparison with mean temperatures obtained by a thermocouple showed that the accuracy of ZnO thermography was within 3 K at 410 K (0.7%) in the jet core region. As a 2D thermometry technique, 1% accuracy for flows below 500 K is expected so as to make it a competitive candidate among all state-of-the-art temperature imaging techniques.

Compromises were made in the time separation ΔT to allow sufficiently high energies for both PIV and phosphorescence. However, reasonable velocity measurements were obtained due to large particle number density in each interrogation window. Higher spatial resolution temperature and velocity imaging ($110.5 \mu\text{m} \times 110.5 \mu\text{m}$) are demonstrated compared with previous studies. Unsurprisingly, the velocity structures show similarities to the temperature structures, and the vorticity contour is correlated with the entrainment structures shown on the temperature field. This shows the potential of thermographic PIV for investigating fundamental problems in fluid mechanics. Future work will aim to improve the quality of the data via optimized timing, resolution and seeding of the co-flow streams.

Due to several limitations on hardware, the experimental parameter settings are sitting on the edge of the optimum conditions for both PIV and thermography. The data quality could be largely improved if (a) a dual-cavity PIV laser with UV capabilities is made available so that the pulse energy is not limited by the pulse separation time, (b) commercial phosphor particles with coating can be used, to remove particle aggregation, (c) high quantum yield sensors are used for fluorescence cameras near the UV, and (d) an effective seeding mechanism can be guaranteed for various ranges of flow rate. If these conditions can be satisfied, the thermographic PIV technique can be readily applied and optimized to investigate various problems of turbulent heat transport and mixing.

2.8 Further Considerations

2.8.1 Double-pulsed UV laser

The main experimental difficulty in this study was caused by the single-cavity laser. We tried to operate the Continuum single-cavity UV laser in double pulse mode, which then created

several constraints such as pulse energy, time interval between two pulses, and the quality of laser beam. This placed a great challenge for the experiment that an appropriate window should be found for sufficiently high laser energy but at the same time reasonably short time interval for the jet velocity. The compromise also sacrificed the quality of both temperature and velocity measurements. To obtain a good temperature measurement, it is better to have a diverging light sheet formed at a high laser energy, and trimmed by a slit so that the final laser profile at the test section is near top-hat (for example to use the central region of the laser profile at $z = 16\text{-}22$ mm *blue line* only, shown in figure 2.8). On the contrary, in the present experiment, the fluence of the Gaussian laser sheet varies significantly from 20-213 mJ/cm² spatially. If a robust SNR is guaranteed at the edges of the light sheet, the particles subjected to the top-hat region would have already been saturated and heated up by the excessively high laser fluence. For a good velocity measurement, a laser system with a tunable pulse interval independent from the output energy is necessary, and a top-hat energy profile is desirable.

This problem can be solved by upgrading a green PIV laser to a UV-PIV laser. Commercial third-harmonic crystals that suit the energy level of most PIV lasers have now available for prices in the low thousands.

2.8.2 Particle size for velocity and temperature measurement

Zinc oxide is a special phosphor since it does not contain a separate ceramic component, which makes the morphology of ZnO very different from other phosphors such as BAM:Eu²⁺. The primary particle size of ZnO powder used in this study is very fine (about 200 nm [44]), but due to large inter-particle forces, aggregate sizes range from one micron to over 20 microns. It has been explained that large aggregates bias both temperature and velocity measurements because of the long relaxation time. However, in later experiments (the heat transfer experiment described in the next Chapter), we added a 0.8 mm orifice downstream the seeder to break down the aggregates by the strong shear formed at the exit of the orifice (a long pipe line was used to dampen the noise generated by the choked flow). The image quality was greatly improved by this measure, and the inline heater was no longer blocked by the aggregates even after hours of operating time. Small particle sizes are also good for

temperature measurements as they reduce the response time to temperature change and may mitigate multiple scattering effects. However, particles of such a small size (probably less than 500 nm since no distinct particle image is observed) are not suitable for PIV measurements, which require clear particle image patterns to enable a robust cross-correlation. Clearly, the phosphorescence image shown in figure 1.1 is too smooth for detecting a unique correlation peak.

According to the analysis above, the optimal particle size range for both temperature and velocity measurement should be around 0.5-2 μm . Within this range, the particle relaxation time is sufficiently short [16] whilst the phosphorescence or Mie scattering signal is strong enough to produce a recognizable spot for individual particles. This conclusion is of course suitable for the present experiment, and different field of views, velocities and camera resolutions would lead to different numbers as a result of the same considerations.

2.8.3 Phosphor particles with a longer decay time

One important premise of this single-laser, two-camera setup is that the phosphorescence emission decays sufficiently fast so the individual particle image does not appear as a streak on both frames. The decay times of ZnO and BAM:Eu²⁺ are less than 1 and 2 μs at room temperature and even shorter at high temperatures, hence satisfy the assumption well. However, for two other types of frequently used thermographic phosphors, YAG:Dy and MFG:Mn, the decay times at room temperature are about 0.4 and 1 ms [12] respectively. Consequently, at low temperatures, the phosphorescence emission from each individual particle leaves a particle trajectory on the CCD chip, especially for the second frame, hence may not be suitable for low speed lasers and cameras.

Chapter 3

Heat transfer visualization in a laminar impinging jet using phosphor thermography

3.1 Introduction

3.1.1 Impinging jet

Heat transfer by jet impingements has been investigated for decades due to the wide application for surface cooling in combustors, gas turbines and electrical devices. An impinging jet consists of three regions: the free jet impinges onto a hot surface (**stagnation region**), flows along the surface (**wall-jet region**) until it finally detaches from the surface and forms a large recirculation zone (**mixing region**). During this process large amount of heat is brought away from the surface. Figure 3.1 shows a schematic view of an example impinging jet, adapted from [49]. There has been a vast literature on this topic, both experimental and computational. Comprehensive reviews of the previous experimental efforts can be found in [50] and [51], and numerical studies have been summarized by [52] and [53]. The characterizing parameter for impinging jet is the Nusselt number Nu , defined as the ratio of convective and conductive heat transfer. Most of previous studies on the impinging jets

were focusing on investigating how the Nusselt number profile along the impinging wall was affected by nozzle-plate distance and Reynolds number [49, 54–56], nozzle shape and geometry [57], confinement [58], jet array arrangements [59–62], pulsating flow [63–65], multiple-phase fluids [66–68] and their combinations, for the purpose to find an optimal cooling configuration which enabled highly efficient heat transfer.

Figure 3.1 is removed for the copy right reason. Copyright holder is M. Angioletti.

Fig. 3.1 A schematic view of an impinging jet, after [49]

The scope of this chapter is limited to the effects of nozzle-plate distance on the Nusselt number. The two main conclusions from the literature regarding the nozzle-plate distance are summarized as follows:

First, in several early studies [54, 69], the Nusselt number at the stagnation point was found to increase with nozzle-plate distance H/D , attained a maximum at a distance $\sim 110\%$ of the potential core length [70], and then decrease beyond this point, for a Reynolds number above 20000. This optimal nozzle-plate distance for heat transfer is considered to be the outcome of a competition between the development of turbulence-induced mixing and depletion of arrival momentum at the stagnation point, as H/D increases.

Second, for small nozzle-plate distances, the maximum Nusselt number is not located at the stagnation point [55]. Instead, the Nusselt number profile forms two symmetric peaks at both sides of the stagnation point, named as ‘secondary peaks’ in the following text. Similar observations were also reported by [54, 71] and others. As H/D increases, the secondary peaks gradually move outward and disappear, and the local maximum returns to the centreline.

The formation of the secondary peak is still controversial. Lytle and Webb [55] attributed this to a high radial velocity and thus an intense shear with ambient air at low H/D values which caused high turbulence at the position of secondary peaks. O'Donovan *et al* found that the secondary peaks appeared only when the potential core of the jet was truncated by the wall, and that the position of the two peaks coincided with the shear layer on both sides of core. Following these observations they drew a conclusion that the secondary peaks were influenced more by the axial velocity fluctuations rather than the radial velocity fluctuations [72]. Some researchers linked the secondary peaks to the vortex structures originated from the jet shear layer. Breakdown of the vortical structure enhances near-wall momentum [73] and thus promotes the local heat transfer.

3.1.2 Flow field measurement

Although the essence of the impinging jet study is to investigate the role of air flows on heat transfer, most of previous studies focused on vector field measurements with the aid of PIV and correlating them with Nu profiles. There were only a few attempts made on temperature imaging [74], or simultaneous measurements with velocity [10, 9, 75, 76] by combining PLIF and PIV. All these experimental studies revealed a heat removal mechanism whereby the vortex structure produced a 'flare' which extracted and ejected hot air away from the thermal boundary layer. However, in a quantitative analysis in [9] where simultaneous temperature and velocity data were obtained from toluene PLIF plus PIV, the heat transfer by vortices took only 7.5% and 12.5% of the overall turbulent heat flux for Reynolds numbers of 5000 and 2000, respectively. This suggests the heat removal mechanism by vortices should only has a marginal effect on the Nusselt number profile. To understand the role of vortical structures beyond the small scale stochastic turbulence in heat transfer enhancement, further multi-physics measurements are needed. One major difficulty in temperature measurements using acetone or toluene PLIF for gaseous impinging jets is that the diffusivity of these molecular tracers is very high, so the signal strength drops quickly in the jet-wall region, limiting the temperature measurements within a small area close to the geometric centre (for example $r/D < 0.6$ in [9]). Therefore this technique can hardly be applied to investigate the

heat transfer beyond the stagnation zone, where vortical structures develop, interact with ambient air and finally break up, unless the whole test rig is placed in a container filled with toluene vapor.

One possible alternative is to use phosphor particles as the temperature tracer, which have a much larger Sc number in air. Although the seeded jet flow still mixes with unseeded ambient air which leads to a drop in SNR, it is a much slower process than the diffusion of toluene, thus allowing a much large measurable area away from the stagnation point, as demonstrated in the present study. Further, LIP allows the simultaneous measurements of velocity and temperature, allowing simultaneous local and statistical assessments of heat and momentum transfer in the vicinity of the wall.

3.1.3 Objectives

Although jet impingement has been investigated for years, there are still many disagreements, especially on the formation of the secondary peaks on Nu profiles at low nozzle-plate distances. To conclusively close these disputes, a database including simultaneous acquired time-resolved field temperature, velocity, and instantaneous Nu profile at various conditions must be created and analyzed. So far there have not been any studies that could provide such comprehensive data for impinging jets, due to the high cost and experimental difficulties involved. However, with the high-speed thermographic PIV system, combining with a high-speed infrared camera (for Nusselt number measurement), this goal could be realized at a reasonable expense.

In this study, we use phosphor thermometry to measure the gas-phase temperature in a **laminar** impinging jet using two ICCD cameras, whilst a low-speed IR camera was installed to measure mean Nu profiles on a ohmic-heated surface which produces a constant heat flux. This study serves as a feasibility demonstration for future work using high-speed systems, which enables time-resolved measurements.

3.2 Experimental

3.2.1 Thin stainless steel foil

The most common approach to measure Nusselt number for impinging jets is called ‘heated-thin-foil’ method, also known as the ‘heat flux’ method. The key of this method is to create a known isoflux surface by heating an extremely thin metal foil/shim using a high current. The small thickness and resistivity of the foil results in approximately uniform distribution of current and thus heat dissipation. In the present study, a $150\text{ mm} \times 81\text{ mm} \times 25\text{ }\mu\text{m}$ shim made from stainless steel 302 (Precision Brand 22125/22L1) was used. The terminals consist of two copper strips which were bolted on the short sides of the foil, as shown in figure 3.2. Silver adhesive (Thorlabs EG58) was used as conductor between the copper strips and the foil to ensure full contact, so as to avoid overheated spots at the terminals. The foil was stretched by springs which were fixed to four posts. Ceramic beads (RS 536-4078) were used to prevent heat conduction via the spring to the posts.

Both sides of the foil were coated with a thin layer of black paint. This increases the surface emissivity for the IR thermography, and mitigates near-wall effects for phosphor thermography such as reflection that may affect the accuracy of the temperature measurement. The emissivity of the paint was measured as 0.92 via a standard procedure, described as follows: A $35 \times 35 \times 20\text{ mm}^3$ copper block was heated by a heating film (Omega Engineering KHLV-101/10-P) from the rear side. On the front side, the surface temperature distribution is almost uniform. Half of this face was coated with the same black paint, whilst the other half was taped with a piece of 0.1 mm thick electrical insulation tape (Scotch Brand 88 black vinyl) with a known emissivity of 0.96. The surface temperature was recorded by a FLIR T650sc infrared camera, and the emissivity of the paint was then derived from the ratio of measured temperature on the two materials. The accuracy of the IR camera is $\pm 1\text{ K}$, and the final uncertainty of the emissivity measurement was estimated as 0.5%.

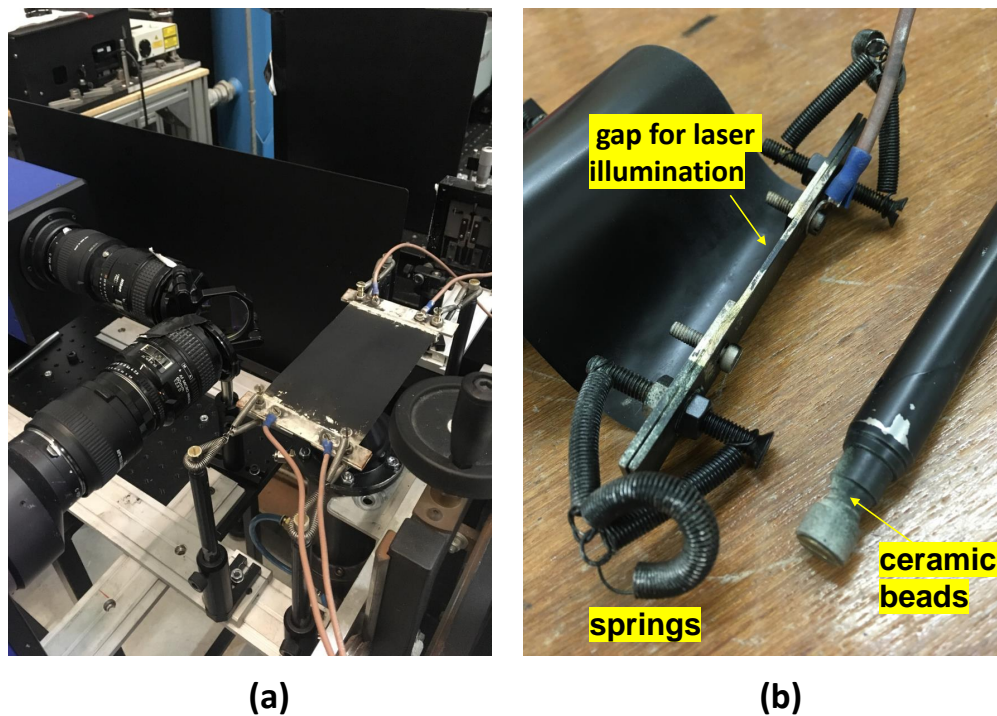


Fig. 3.2 (a) Schematic view of the heated-thin-foil setup. The Infrared camera was on top of foil but not shown in this figure; (b) detail design of the terminals.

3.2.2 Infrared thermography

The current passing through the stainless steel foil was set to 60.0 A, controlled by a special power supply (Telonic PWX1500L) that allowed a maximum current of 150 A. The voltage measured by the power supply was 5.85 V under this condition. The infrared camera had a full image size of 480×640 pixels, and was positioned on top so as to measure the foil surface temperature from the rear side of the plate relatively to the flow. The surface temperature was averaged over 30 images for each test condition. The spatial resolution of this IR camera is calibrated as 0.2 mm/pixel. Since the foil is thin, we assume the surface temperature measured from the back equals to that from the front side (impingement). Without the presence of the impinging jet, the foil temperature is about 623 K. About ± 10 K temperature fluctuation was observed due to the small perturbation of ambient air flows.

Unlike previous experimental studies which performed the heat flux method at a low current, we heated the foil by a strong current to a high temperature beyond 500 K. The

reasons for setting such a high temperature is related to the accuracy of the gas-phase phosphor thermography, which is introduced in subsection 3.2.4. A high foil temperature also reduces the uncertainty in IR thermometry. The radiative signal from the camera itself and other objects in the laboratory is reflected by the foil and contributes to the recorded signal; if the foil temperature is high, reflection contributions are negligible compared with the strong radiative signal emitted from the foil. Whereas this is useful for the present thermographic method, higher temperatures lead to lower accuracy of the heat flux method: since the radiative heat loss is proportional to $(T_s^4 - T_\infty^4)$, it can consume a higher fraction of the losses relatively to the total ohmic heat produced by the current at high temperatures. In such case, an accurate estimation of exact value on the heat loss becomes more important for the accuracy of the Nusselt number measurements.

3.2.3 Flow and particle seeding system

A cylindrical chamber with an aerodynamically shaped nozzle of 12 mm exit diameter was used to produce the impinging jet, shown in figure 3.3. The nozzle flow produces a top hat velocity profile at the outlet, as characterized by PIV in a previous study. The air flow rate for the jet was controlled by a 50 slpm Alicat MFC with 1% fs precision, and the value was set to 25 slpm. The bulk velocity is estimated as ~ 4.0 m/s at the exit, and the corresponding Reynolds number is $Re = 3200$, calculated based on the nozzle diameter and the air flow rate at 291 K. ZnO particles (Sigma-Aldrich 96479) were used as gas-phase temperature tracers and were dispersed into the air flow by a vibrating-type seeder (Texas Airsonics AJ-1). The seeding rate was controlled by the power to the vibration unit. The primary particle size of the ZnO powder was reported to be about 200 nm [44]. However, in our previous study described in Chapter 2, the issue of particle agglomeration for the same ZnO product was reported, which affected the quality of the data and was therefore removed by image processing. Herein, the agglomeration problem was solved by adding a 0.8 mm orifice to the air-line downstream the seeder: the high shear formed at the exit of the orifice easily break up most of the large aggregates. The high-frequency acoustic noise produced by the choked flow was dampened through a 5 metre-long pipe which led the flow to the chamber. This

method greatly improved the data quality for LIP measurements, as shown in the raw images presented further on.

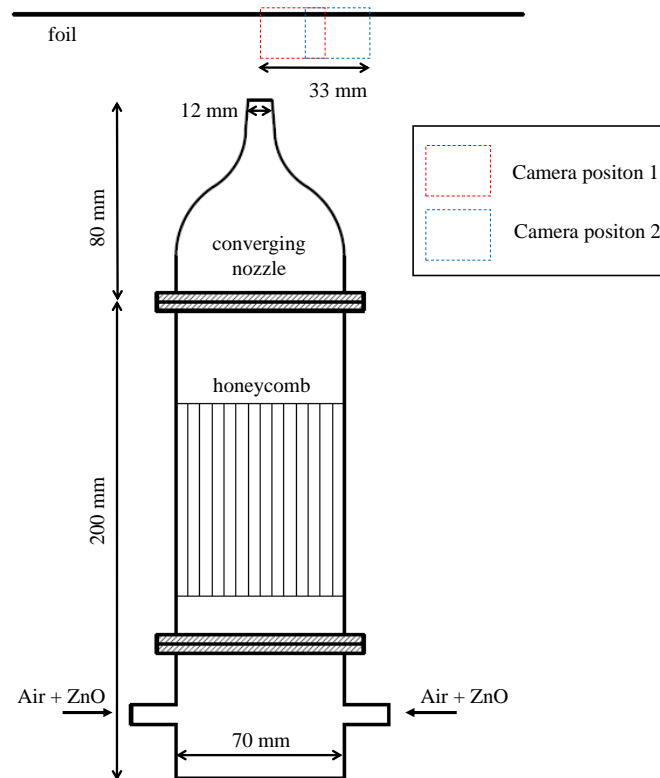


Fig. 3.3 A schematic view of the impinging jet (burner cross-section), and two measurement positions.

3.2.4 Phosphor thermography

A Nd:YAG single-pulsed laser (Continuum, Surelite III) operating with a third harmonic generator was used to produce a laser sheet at 355 nm, illustrated in figure 3.4. To avoid direct incidence of laser light shining onto the foil, which causes strong reflection, a combination of $FL = -9.7$ mm and a $FL = 150$ mm cylindrical lenses was set at the right position to produce an approximately 80 mm tall non-diverging laser sheet. The field of view was limited by height of the second cylindrical lens to around 40 mm, while the edges of the laser profile were blocked by the lens holder. A $FL = 400$ mm cylindrical lens followed to reduce the beam thickness to about 0.2 mm at the test section. The laser sheet was further trimmed

by a slit to 10-20 mm in height, depending on the nozzle-plate distance, to avoid scattered laser light from the nozzle leading to biases in the measurement [42]. The final laser sheet formed over the nozzle has a top-hat shape, as verified by the laser-dye method described in [77]. The measured laser fluence at the test section was 113 mJ/cm^2 with a temporal fluctuation about 8%.

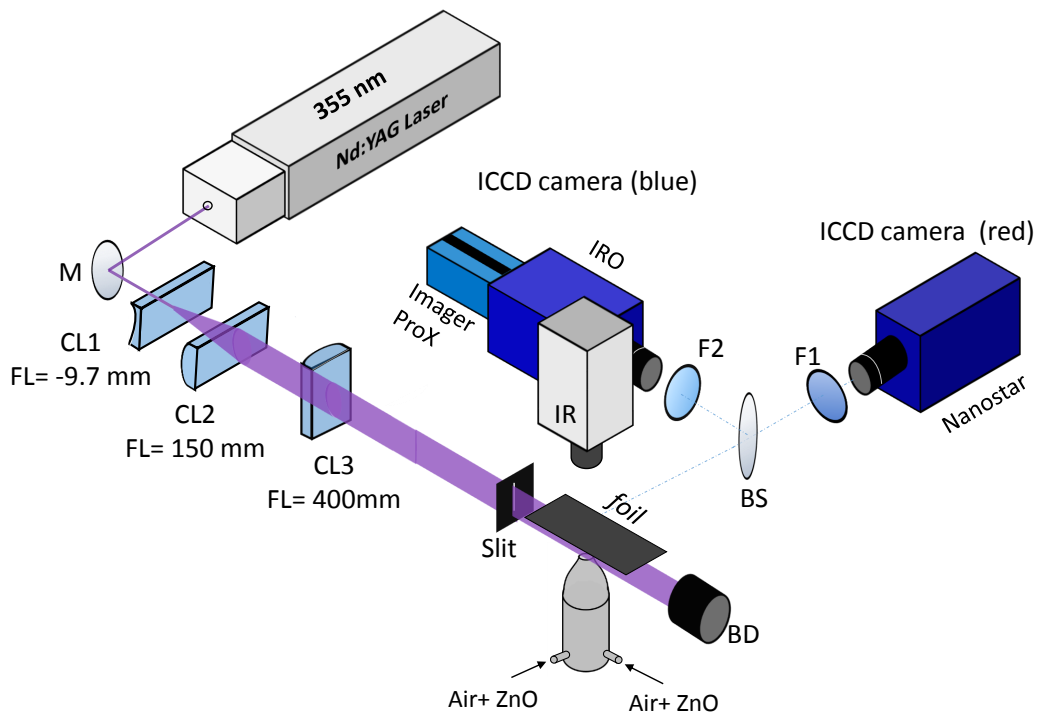


Fig. 3.4 Experimental setup. BD beam dump; BS beam splitter; CL cylindrical lens; F bandpass filter; FL focal length; IR infrared camera; M mirror.

In order to avoid multiple scattering effects, a low seeding rate was intentionally used. Two ICCD cameras (a Nanostar and a ImagerProX 4M equipped with an IRO, Lavision) were used to boost the signal for the two-color measurement. A good spatial resolution was achieved by using an AF Micro Nikkor 60 mm lens ($f/2.8D$) was combined with a Sigma $\times 2$ Teleconverter to focus the image. Since the Nanostar has image size of 1280×1240 pixels while that of ImageProX is 2048×2048 pixels. We performed 2×2 hardware binning for ImageProX so as to achieve a similar spatial resolution for both cameras. The two cameras were carefully aligned on micro-stages to overlap their field of view. The pixel

resolution for each camera was calibrated by a target. Further image rescaling and mapping was implemented by a Matlab program, and the final pixel resolution for both cameras was determined as $21 \mu\text{m}$. A $387 \pm 5.5 \text{ nm}$ interference filter (Edmund Optics 84094) and a $425 \pm 25 \text{ nm}$ filter (Edmund Optics 86961) were installed in front of the IRO (blue channel) and the Nanostar (red channel), respectively. A 50 mm diameter 50:50 beam splitter for UV light (Edmund Optics 48192) was mounted in front the cameras to separate the phosphorescent emission. The gain of the blue and red channel was set to 50% and 30% respectively. The use of an intensifier smeared the particle images and slightly reduced the spatial resolution relatively to a non-intensified image. However, since a moving average filter is applied to process the raw image later in the image processing stage, the blurring caused by the use of intensifiers does not affect the final spatial resolution for the temperature measurement. The shutter opens $\sim 1 \mu\text{s}$ before the laser pulse and the exposure time was set to $5 \mu\text{s}$ for both cameras in order to capture the whole emission decay ($< 1 \mu\text{s}$), for both ZnO calibration and impinging jet measurement. The laser was operating at 10 Hz, whilst the cameras were recording at 5 Hz due to the limitation of storage speed. A total number of 800 image pairs were recorded for each test condition.

The temperature sensitivity of ZnO emission is low below 350 K with the two selected filters. Hence, the foil temperature should be sufficiently high ($\sim 623 \text{ K}$) to heat the air up to the best working temperature range for ZnO particles for this filter combinations. For the same reason, the flow speed must not be too high, otherwise the residence time is too short to warm up the air flow adequately. This currently limits the range of Reynolds number that can be investigated. In this study, we used a low Reynolds number (3200), and observed the influence of H/D on the heat transfer. If an investigation of a higher Reynolds number is intended, then phosphors such as $\text{La}_2\text{O}_2\text{S:Eu}$ and $\text{Y}_2\text{O}_2\text{S:Er}^{3+}, \text{Yb}^{3+}$ should be chosen because they have a much higher temperature sensitivity in 300-350 K range than ZnO does.

Another reason to set such a high foil temperature is related to the particle deposition. Inevitably, a few particles depositing on the foil produced a blooming spot on the image at the corresponding position when the foil is cold. However, if the foil temperature is high ($> 500 \text{ K}$), the particles on the foil emitted little signal due to strong thermal quenching. Hence,

by setting a high foil temperature, the near-wall effect can be greatly reduced, as shown in figure 3.5. Some previous studies have reported an enhancement of heat transfer by adding submicron particles into the gas or liquid (Nano-fluids) such as [78], but inconsistent or even contradictory observations have also been reported by some other research groups [79]. In the present study, we observed that the foil temperature was on average ~ 2 K higher when the jet flow was seeded with ZnO particles than a non-seeded flow. This could probably be attributed to the particle deposition, which formed a thin layer that prevented the heat transfer. Although this slight temperature difference would cause little error to the measurement, only 100 images (in 20 seconds) were recorded for each dataset, after which the foil was carefully cleaned by a non-flammable air duster to prevent accumulation of particles. This procedure was repeated until a total number of 800 images had been collected for each test condition.

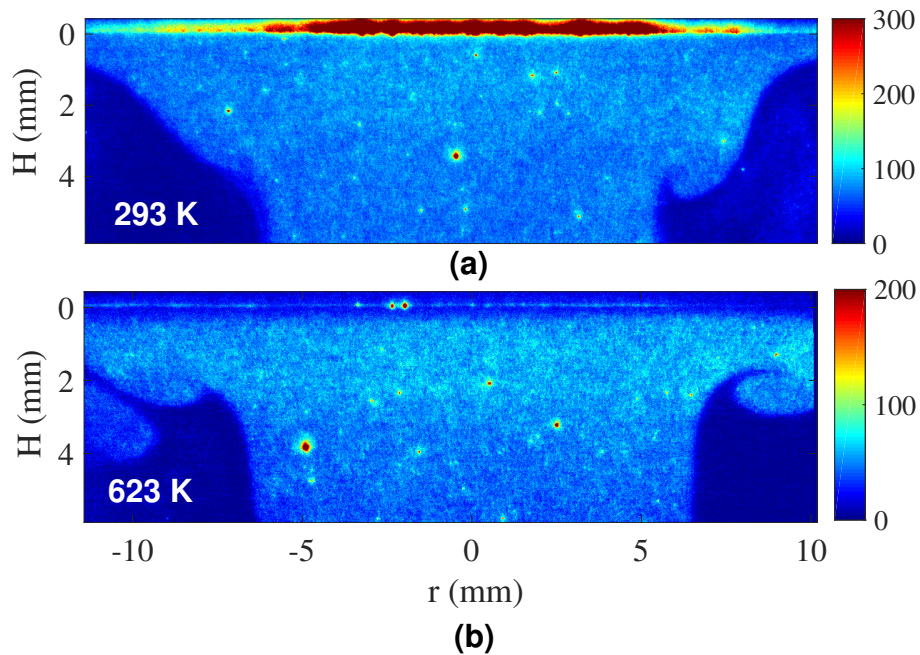


Fig. 3.5 Example raw image for (a) cold foil at room temperature (293 K) and (b) heated foil at 623 K, both collected from the red channel. The colorbar shows the camera count. In the latter case, the particles on the surface were strongly quenched by the high temperature.

3.2.5 Image processing

Dark noise and background was subtracted from all images. The image pairs collected at two channels were further mapped for a perfect overlap, and then smoothed by a 5×5 moving average filter. The noise level after smoothing is 1.6 counts, and the final spatial resolution is $105 \mu\text{m}$. A threshold of 15 counts was applied to remove the noise and weak signal before the ratio was taken between two channels. A flat field correction (normalize the intensity ratio field by the one measured at room temperature to eliminate the effects of non-uniform excitation, laser attenuation etc.) was not performed here, because of the deposition problem for a cold foil shown in figure 3.5. Therefore in this experiment extra efforts were taken to reduce the error brought by not conducting flat fielding, as follows: (a) a top-hat non-diverging laser sheet was generated, (b) laser sheet was trimmed to prevent reflection, (c) a low seeding rate was used to avoid laser attenuation and (d) white field correction was performed by imaging a piece of A4 paper at a defocused position, which was illuminated by a LED torch (RS 479623) at a far distance, to correct of the non-uniformity in filter transmissivity, CCD sensitivity, and reflectivity of the beam splitter. These arrangements should effectively improve the accuracy of the temperature measurement without conducting the flat-field correction.

3.2.6 Calibration of ZnO tracer

The intensity ratio of ZnO phosphorescence signal at the chosen two bandwidths was calibrated as a function of temperature on a heated jet, which had a nozzle diameter of 9.2 mm and $\text{Re} = 3800$ at 291 K. The air flow was heated to various temperatures by an in-line heater (Omega Engineering AHP-7562), ranging from room temperature to 473 K. In our previous work [77], the use of such in-line heaters was not possible because aggregates of ZnO particles were found to stick between the coils and thus block the flow. However, after applying the orifice to break up the aggregates in this study, the seeded flow no longer clogged the heater even after hours of operation.

Prior to the phosphorescence imaging, a K-type thermocouple of 0.5 mm diameter was placed in the jet core 3 mm above the nozzle (with the presence of particles) to record the mean temperature, in the central region where the flow was stable for each condition. The intensity ratio measured over the probed region marked by a $1.05 \times 1.05 \text{ mm}^2$ black square. Since the seeding rate fluctuated shot-to-shot, occasionally there were snapshots with extremely low seeding, and thus a poor SNR which would bias the temperature measurement. To eliminate this, we took a scan of the whole 800 images recorded for each temperature, and plotted intensity ratio (spatially averaged) in the marked square versus the corresponding the signal intensity at the red channel ($425 \pm 25 \text{ nm}$) in the same region, as shown in figure 3.6. When the signal strength is lower than 22 counts, the measured intensity ratio starts to bias. Based on this threshold, all images whose intensity in the red channel is lower than 22 counts in the core region were rejected. The remaining images numbered over 400 for each temperature. Since the flow used in this study remains laminar, several hundreds of images are sufficient for converged statistics. The same criteria was also applied to preprocess the impinging jet data.

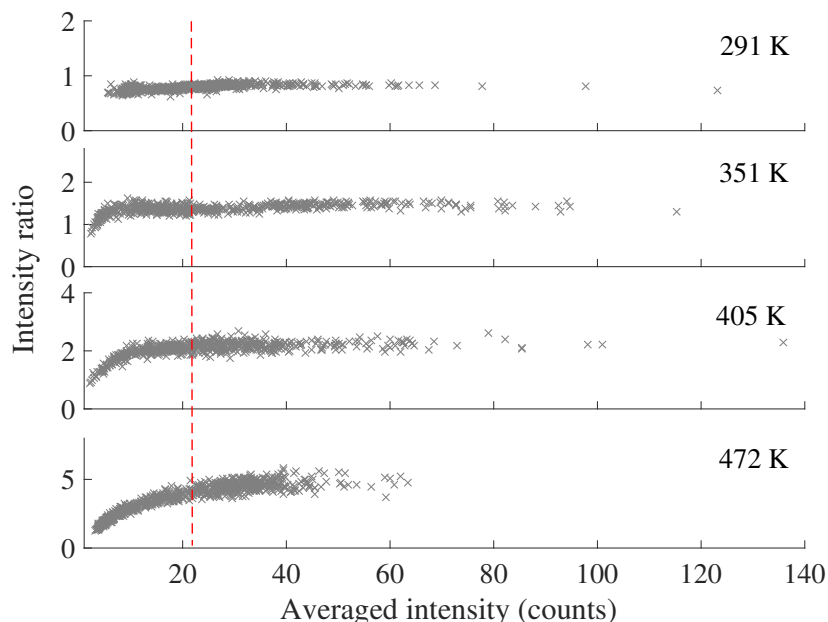


Fig. 3.6 A scan of intensity ratio versus the averaged intensity (red channel) in the probe volume over 800 images, for inlet temperatures of 291, 351, 405 and 472 K, respectively. Images whose intensity in the core region was below 22 counts may bias the temperature measurements and were rejected.

Figure 3.7 shows the calibration curve for ZnO. Circles are the mean intensity ratio measured at the corresponding temperature averaged over the remaining images, and error bars denotes the root mean square of the variance. The solid line is the best quadratic fit to the data points. The calibration curve was extrapolated to 500 K in case the near surface gas temperature slightly exceeds the calibrated range.

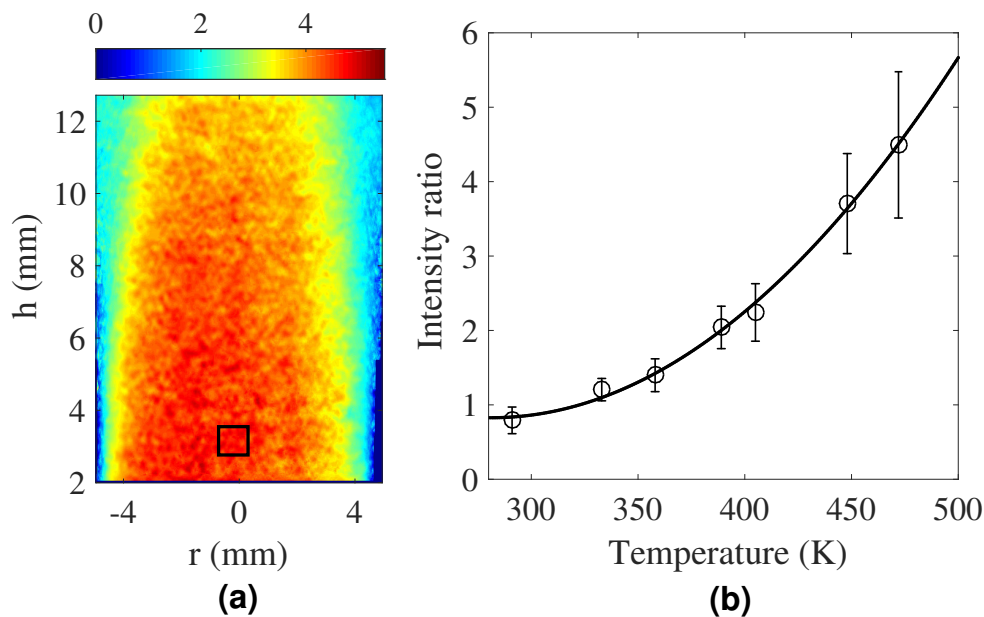


Fig. 3.7 (a) Mean intensity ratio (425 ± 25 nm over 387 ± 5.5 nm) at 472 K in the marked probe volume; (b) mean intensity ratio as a function of temperature in the marked region. Intensity ratio RMS are presented as vertical error bars. Circles are the calibration data points, and the black line is the best quadratic fit.

3.2.7 Test conditions

The test conditions are summarized as follows: a jet of $Re = 3200$ at 291 K impinged on heated foil at $H/D = 1.0, 2.0, 3.0$ and 4.0 , respectively. The room temperature was 293 K with a fluctuation less than 3 K during the experiments.

3.3 Determination of Nusselt number

In the heat flux method, the Nusselt number is calculated from assuming a known convection rate at the wall (foil), so that

$$h(r) = \frac{\dot{q}_c(r)}{T_w(r) - T_j} \quad (3.1)$$

$$Nu = \frac{hD}{k} \quad (3.2)$$

where h is the heat transfer coefficient and is a function of radial distance r , k is the thermal conductivity of the air, and D is the jet nozzle diameter. The heat flux \dot{q}_c corresponds to the estimated convective heat flux at the wall. Temperatures T_w and T_j are measured at the wall and core jet. Note that most previous studies used T_j as the reference temperature. However, since Nusselt number reflects a near-wall heat transfer efficiency by convection, a more appropriate choice of reference temperature should be the adiabatic wall temperature T_{aw} . To be consistent with previous literature, we still use T_j in the present study. The convective heat transfer between the foil and the jet is calculated from the electrical Joule heating \dot{q}_j produced by the foil minus the estimated losses,

$$\dot{q}_c = \dot{q}_j - \dot{q}_l \quad (3.3)$$

\dot{q}_j is the joule heat flux produced by the foil, and \dot{q}_l is the heat flux loss, which is a function of radial distance r . The heat dissipated per unit area of the foil reads

$$\dot{q}_j = \frac{I^2 R}{BL} = \frac{I^2 \rho}{\delta_z B^2} \quad (3.4)$$

I is the current controlled by the power supply. B , L , and δ_z are the width, length and thickness of the foil respectively, and ρ is the resistivity of stainless steel. Unlike previous studies, for the high temperature used in this study, the resistivity is a function of temperature $\rho = \rho(T)$. The heat loss consists of thermal radiation from the front side $\dot{q}_{r,f}$, rear side $\dot{q}_{r,r}$,

and free convection $\dot{q}_{c,r}$ on the rear side of the foil.

$$\dot{q}_{r,f}(r) = \sigma \varepsilon (T_w(r)^4 - T_j^4) \quad (3.5)$$

$$\dot{q}_{r,r}(r) = \sigma \varepsilon (T_w(r)^4 - T_\infty^4) \quad (3.6)$$

$$\dot{q}_{c,r}(r) = h_0 (T_w(r) - T_\infty) \quad (3.7)$$

where r is the radial distance, σ is the Stefan–Boltzmann constant, ε is the emissivity of the black paint, T_∞ is the room temperature. The heat transfer coefficient h_0 by natural convection was measured by changing the current and recording the corresponding foil temperature without the impingement. At steady state conditions, the Joule heat flux matches the heat loss,

$$\dot{q}_j = \dot{q}_{r,f} + \dot{q}_{r,r} + \dot{q}_{c,f} + \dot{q}_{c,r} \quad (3.8)$$

The last two terms in Eq.(3.8) can be calculated by subtracting Eq.(3.5), (3.6) from Eq.(3.4). Because there is no impingement in this case, the heat loss by free convection is assumed to be the same on both sides $\dot{q}_{c,f} = \dot{q}_{c,r}$. The heat transfer for free convection is

$$h_0 = \frac{\dot{q}_{c,f}}{T_w - T_\infty} \quad (3.9)$$

which was measured as $5.9 \text{ W}/(\text{m}^2 \cdot \text{K})$. The steps described above are the heat-flux method to determine the Nu number profile. Note that in this study a low speed infrared camera with a long exposure time was used for foil surface temperature imaging, which yields an averaged Nu profile. If a high-speed infrared camera is available, instantaneous Nu profiles can be measured and correlated with the flow structure.

3.3.1 Results and discussion

Figure 3.8 shows Nu profiles measured by the heat-flux method, using the measured wall temperature as a function of radius. The Nusselt number decreases quickly as the radial distance increases. Nu at the stagnation point changes only slightly with H/D as a parameter.

The maximum value is at the centreline for $H/D = 4.0$, but off-centre for lower nozzle-foil distances, around $r/D = 0.65$. This is consistent with previous observations by [49] and [55] for an impinging jet with low Reynolds numbers. It is shown further on that when H/D increases from 3.0 to 4.0, laminar flow becomes unstable, and this enhances the heat transfer around the stagnation zone, hence at the stagnation point a higher Nu was measured at $H/D = 4.0$.

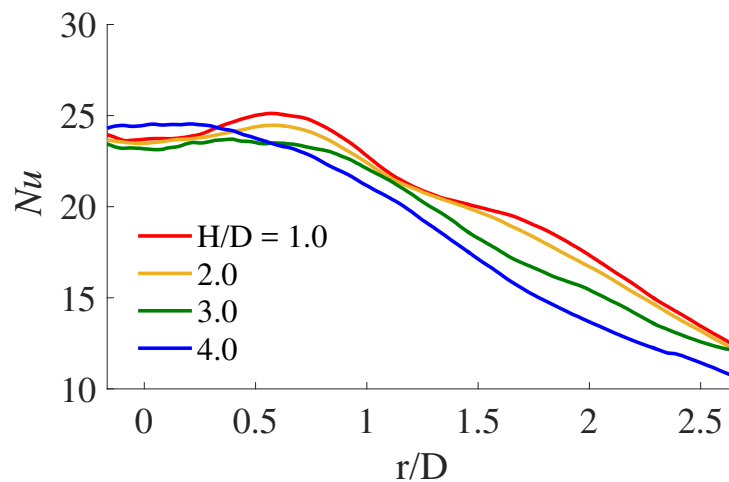


Fig. 3.8 Nusselt number profiles calculated by the traditional heat flux method, for $H/D = 1.0, 2.0, 3.0$ and 4.0 , respectively.

3.4 Temperature imaging

Unlike previous PIV studies which used micron-sized tracer particles, the primary particle size of ZnO powder used in this study is only 200 nm, and most of the aggregates have been broken up by the intense shear when passing through the orifice. Therefore the particles can serve both as a temperature tracer and an ideal marker for the jet. The development of eddies and the mixing process is illustrated clearly by the phosphorescence signal collected at the red channel, because the signal strength at this wavelength band is relatively insensitive to the temperature change, as the spectral red-shift at high temperatures partially offsets the thermal quenching effect.

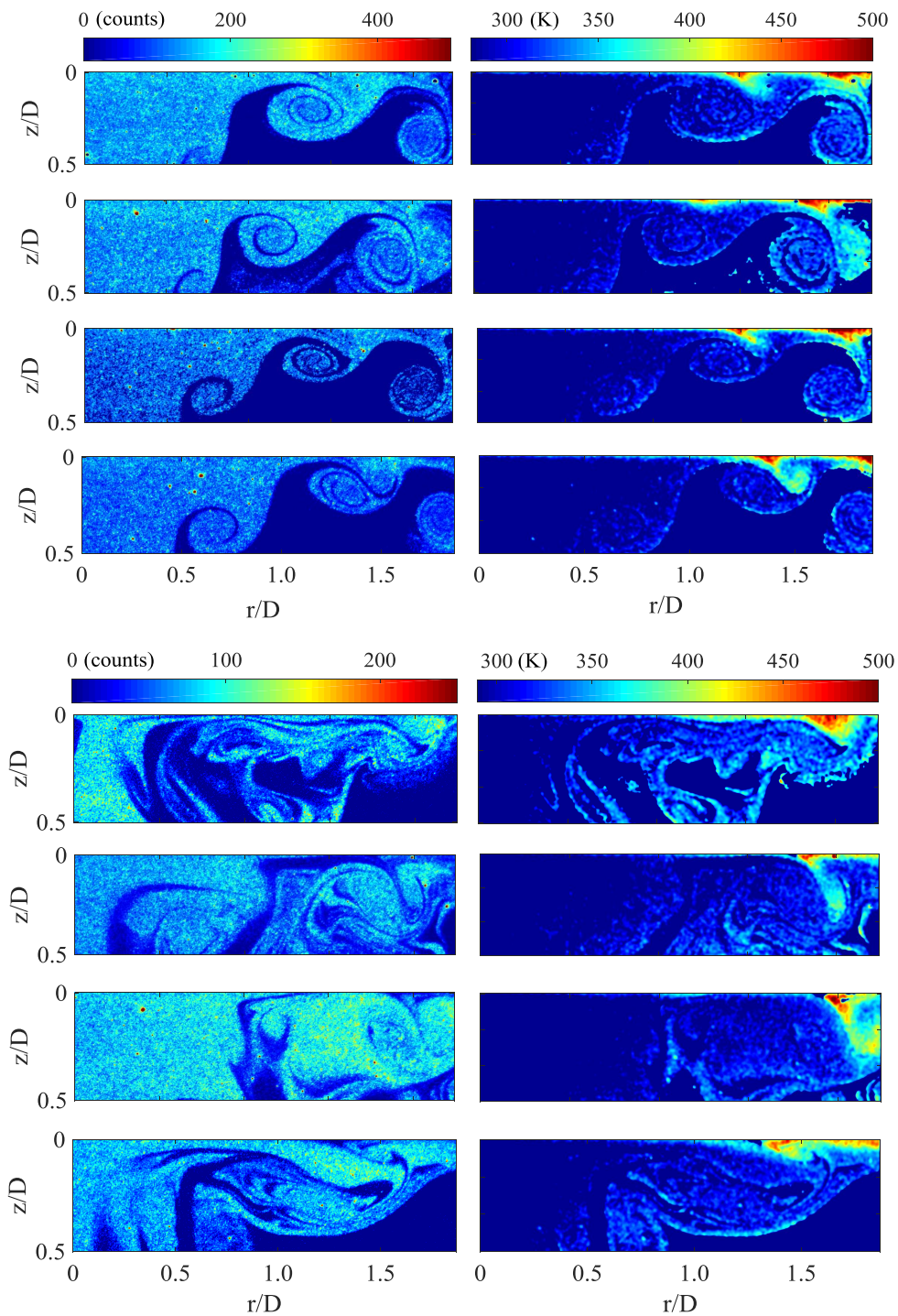


Fig. 3.9 Examples of instantaneous temperature field for (*upper*) $H/D = 2.0$, and (*bottom*) $H/D = 4.0$. The *left column* shows the raw phosphorescence image collected from the red channel, whilst the *right column* shows the corresponding temperature field.

Figure 3.9 shows example instantaneous temperature fields measured by ZnO thermography at $H/D = 2$ and 4, respectively. The raw images collected from the red channel are presented on the left column, which clearly reveal the vortical structure originated from the potential core of the jet, and the corresponding temperature fields are presented on the right column. The jet flow propagates along the wall, gradually picks up the heat, and then mixes with ambient cold air. For low H/D cases, circular vortical structure appears intermittently at a nearly constant rate, which is probably the cause of the cold/warm streaks observed on the wall using a high-speed infrared camera in another study[64]. For large H/D , however, the vortical structures have already breakdown before reaching the wall. In such cases, turbulent mixing, instead of engulfment by large scale eddies, can be observed in the wall-jet region. This may explain why the secondary peak on the Nusselt profile disappeared for $H/D = 4$ in figure 3.8.

Figure 3.10 shows the mean and rms temperature field, for the four nozzle plate distances. From the rms temperature field, for $H/D = 1.0, 2.0,$ and 3.0 , the temperature rms within the stagnation region is low. However, beyond $r/D > 1.5$ the fluctuation in air temperature substantially increases, due to the flapping edge and breakup of vortical structures. For $H/D = 4.0$, the quite stagnation zone disappeared and the temperature rms is ~ 30 K in the whole field. As shown in the instantaneous temperature fields, the perturbation is introduced by breakdown of large eddies which have intruded into the stagnation zone.

3.5 Summary

This work combines the conventional Nusselt number measurement method with gas-phase phosphor thermography to investigate the heat transfer in an impinging jet. The combination of two techniques enables the investigation on the correlation between the Nusselt number and gas temperature. In the following work, a high-speed infrared camera will be used to capture instantaneous wall temperature, and the gas velocity will also be measured simultaneously by adding a PIV camera to the current setup. The relation between instantaneous Nu and heat flux can be achieved, which may help to close the disputations on several issues for

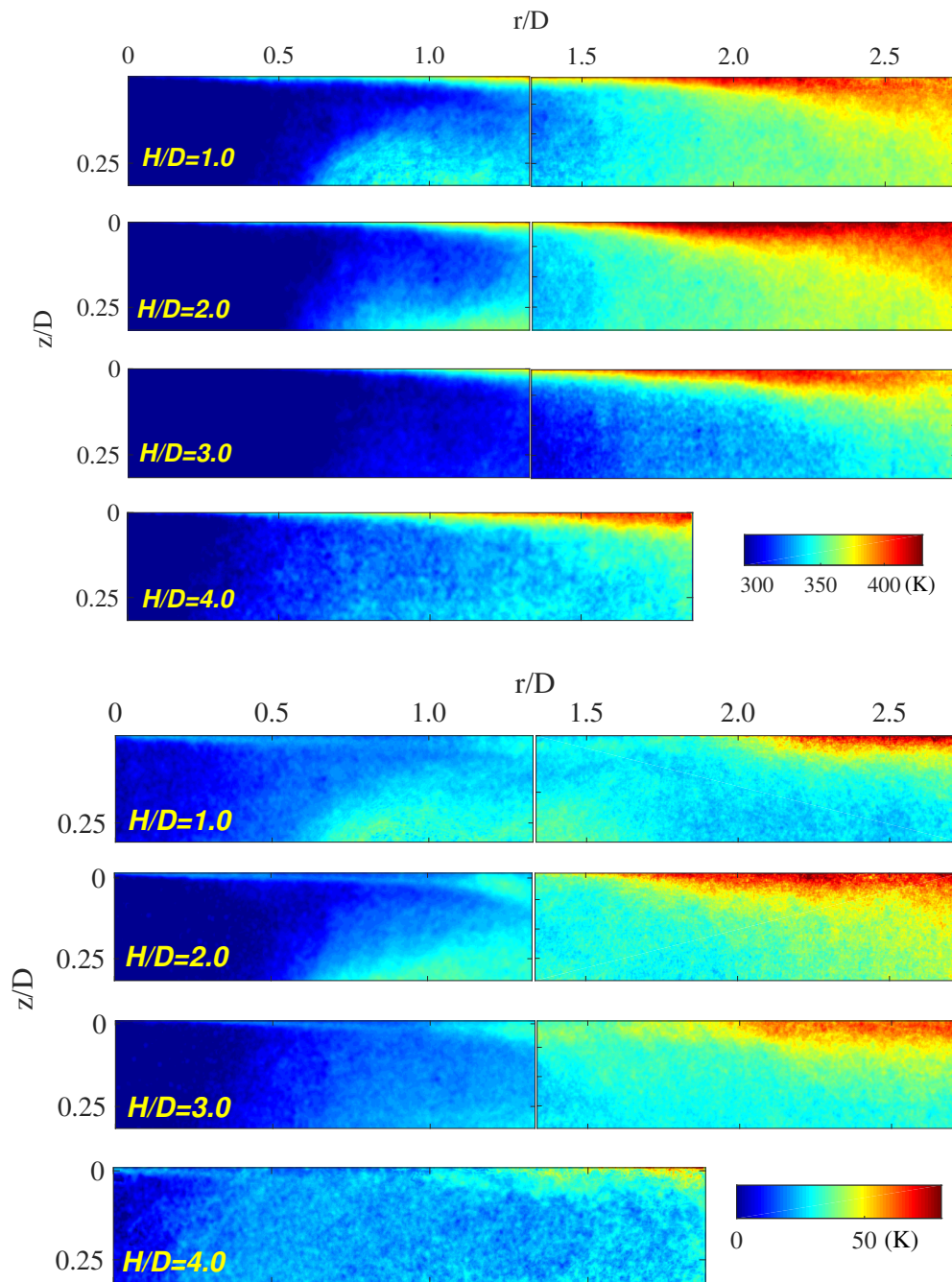


Fig. 3.10 (Upper) mean and (bottom) RMS temperature field measured for $H/D = 1, 2, 3,$ and 4 .

impinging jet, such as the formation of secondary peaks on Nu profiles at low nozzle-wall distances.

Chapter 4

Numerical analysis on SLIPI: gas-phase phosphor thermometry

4.1 Introduction

4.1.1 Multiple scattering

Multiple scatter is a feature of any experiment involving particles. In particular, the issue of multiple scattering in phosphorescence emission has emerged as a source of error in several studies. The term ‘multiple scattering’ has been used to describe the phenomenon by which photons are scattered by particles beyond the target region when passing through an optically dense medium before reaching the detector [80], thus contributing to the signal where none should exist. The phenomenon is prevalent in a variety of systems where small particles or droplets are present, notably in dense sprays. For measurement techniques based on image correlation such as PIV, the uncertainty brought by multiple scattering is trivial unless excessive seeding is used. However, for laser-induced phosphorescence (LIP), multiple scattering may have a more significant influence on temperature measurements. As a technique relying on the intensity ratio of the observed signal, multiple scattering may affect the measurements via several different mechanisms [22] illustrated in Fig. 4.1, and summarised as follows:

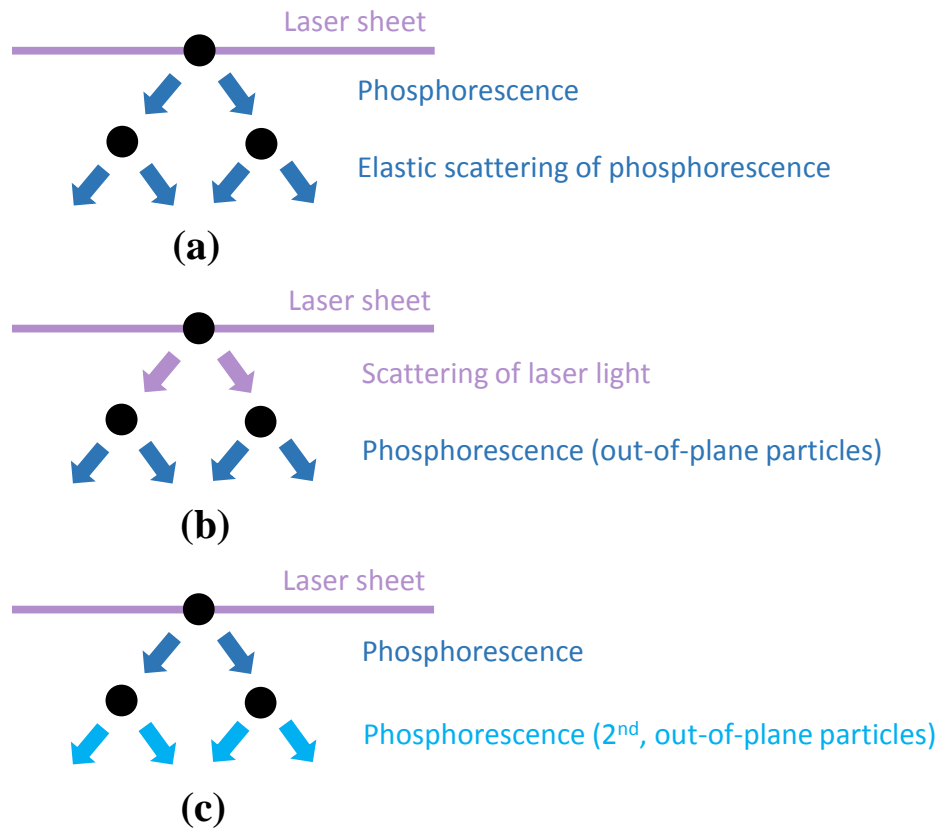


Fig. 4.1 Three mechanisms of multiple scattering for phosphorescence: (a) Elastic scattering of the phosphor signal emitted from the measurement plane; (b) excitation of phosphors by the scattered laser light; and (c) preferential re-absorption and secondary emission. The *black solid circles* represent phosphor particles.

- (a) *Elastic scattering of the phosphor signal emitted from the measurement plane.* In this scenario, the spatial resolution is affected, leading to blurred images. If the spatial resolution significantly deteriorates, the temperature measurements could also be biased. For example, some photons originated from the cold co-flow may be scattered towards the central hot jet, and then captured by the cameras.
- (b) *Excitation of phosphors by the scattered laser light.* Laser light scattered by in-plane particles excites the out-of-plane particles. Hence the signal captured by the detector conveys both in-plane and out-of-plane temperature information.

- (c) *Preferential re-absorption and secondary emission.* The excitation and emission spectra of some fluorescent tracers may partially overlap, and the photons in the overlapping spectral range emitted from the laser plane may be re-absorbed by particles outside the excitation plane and lead to a secondary emission, which may carry different temperature information, yet contribute to the total signal.

An early report on the multiple scatter effect for phosphor particles in dispersed form [22] showed how the phosphor signal could also be captured from outside the illuminated area by a trimmed laser sheet, suggesting that multiple scattering leads to reduced spatial resolution. Similar phenomena were also reported by [41, 42] where the phosphorescence signal appeared in unseeded regions where no signal should have been found. A recent paper investigated the effects of multiple scattering on a film-cooling application [42] in which a 3 mm hot jet was injected into a 40 mm cross-flow at an angle, both seeded with BAM:Eu²⁺. Under these conditions, the effect of multiple scattering was estimated to be responsible for a bias in the jet temperature by ~ 40 K out of 445 K. In the same work, it was reported that the seeding density within the cross-flow should be 10 times lower than that in the jet so as to create an unbiased measurement. However, both signal to noise ratio and spatial resolution severely deteriorate at such low seeding rates. The experiments in [40, 41] proved the fact that, in cases where the signal ratio changes with seeding density, a large temperature bias arises. In particular, if preferential re-absorption occurs, the temperature uncertainty also increases with a longer optical path [14]. Hence for large flow configurations, only controlling the seeding density may not be enough to eliminate the effects of multiple scattering. To solve this problem, it was suggested by [14] that an *in-situ* calibration at exactly the same seeding density and flow condition would, in principle, allow a compensation for the effects of multiple scattering, although this may not always be possible for internal flows.

4.1.2 SLIPI

SLIPI Theory

An alternative solution to multiple scattering in laser-induced phosphorescence is to combine it with structured laser illumination planar imaging (SLIPI), as demonstrated by Zentgraf and co-workers [42]. In that work, near-wall effects and multiple-scatter interference was successfully removed from the phosphorescence signal originating from the laser plane. SLIPI works by reconstructing the signal from multiple (usually three) sinusoidal spatially modulated laser profiles with phase shift angles $0, 2\pi/3, 4\pi/3$, respectively, to illuminate the test area. The assumption is that photons that have been scattered several times or produced during the secondary emission do not preserve the spatial modulation, the true signal can be reconstructed from the modulated fraction, whilst the unmodulated fraction is viewed as scattered signal which does not originate from modulated incident light sheet. The three modulated subimages yield signal intensities (I_1, I_2 and I_3) can be represented by the following general expression

$$I_i = I_{DC} + I_{AC} = I_{DC} + A[\cos(2\pi v y + \Phi_i) + 1] \quad (4.1)$$

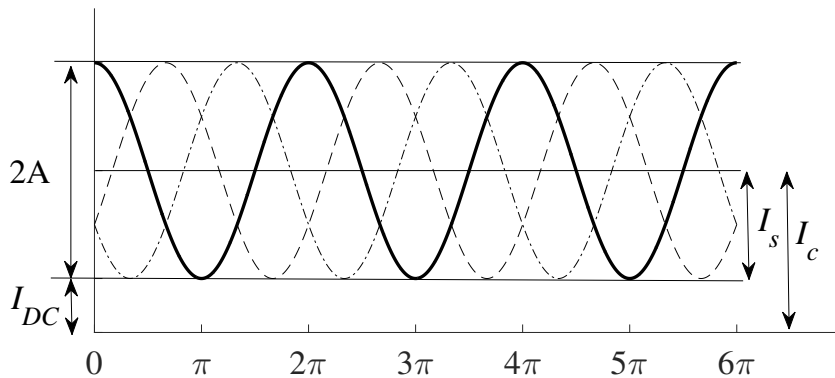


Fig. 4.2 Schematic diagram of three modulated harmonic sub-signals in non-dimensional space, showing the corresponding reconstructed signals.

where I_{DC} (direct current) denotes multiple scattering or any other unmodulated signals, which are assumed to be proportional to the total laser energy passing through the Ronchi

grating; I_{AC} (alternating current) is the modulated signal from the measurement plane; A is the amplitude of modulation; ν the frequency of Ronchi grating. The three sub-signals are sketched in Fig. 4.2. The reconstructed clean image without multiple scattering is extracted by calculating

$$I_s = \frac{\sqrt{2}}{3} [(I_1 - I_2)^2 + (I_1 - I_3)^2 + (I_2 - I_3)^2]^{1/2} = A \quad (4.2)$$

where I_s is referred to in the literature as the SLIPI image. Meanwhile, previous literature introduced the nomenclature of a conventional image I_c :

$$I_c = \frac{I_1 + I_2 + I_3}{3} = A + I_{DC} \quad (4.3)$$

In the work by Kristensson *et al* [81], the multiple scattering fraction ϕ was defined as

$$\phi = \frac{I_{DC}}{A + I_{DC}} = \frac{I_c - I_s}{I_c} \quad (4.4)$$

which was used to quantify the relative amount of light being suppressed by SLIPI, or the contribution from multiple scattering to the recorded signal. All above SLIPI analyses hinge on the assumption that the three input sub-signals generated are strictly *harmonic*, and that the signal behaves *linearly* with laser intensity.

Previous work on SLIPI

SLIPI has been applied to remove scattering or other uncorrelated noise for extracting Mie scattering images in sprays [80], 2D-laser-induced fluorescence (LIF) [82], planar droplet sizing [83] and Rayleigh thermometry [84]. For studies based on averaged or steady-state images, a single laser with a Ronchi (harmonically modulated) grating that can be traversed vertically is sufficient to perform SLIPI. Executing SLIPI on individual shots, however, requires three single-pulsed laser beams and cameras triggered in sequence within a very short time interval so as to keep the tracers at the same position for all subimages. To solve this, a simplified two-pulse SLIPI approach has been developed [85] and later a single-pulse

approach [86]. However, these are not as robust as the three-pulse SLIPI, because the two-pulse approach intrinsically produces residual streaks on the reconstructed image, which requires the use of a low-pass filter; whilst the single-pulse approach loses high-frequency information during the image reconstruction. In a recent study by Kristensson and Berrocal [87], the spatial resolution of one-pulse SLIPI has been improved by crossing two modulated laser sheets at 90° , named xSLIPI.

It is useful to consider under what conditions SLIPI can be usefully applied to LIP. Based on previous literature and the authors' experience in conducting LIP, the application of SLIPI may be necessary when: (a) reducing seeding density is not an option, for example where temperature gradients are high; (b) the experimental test conditions lead to a large scale seeded co-flow region which may introduce severe multiple scattering; and (c) direct incidence of laser light on surfaces cannot be avoided by adjusting the incidence angle or by other strategies such as using UV-absorptive paint. In other situations, excessive multiple scattering can be more easily avoided by reducing phosphor seeding density, whilst the use of intensifiers ahead of cameras can boost the signal (which may also amplify shot noise though). Tests of LIP on BAM:Eu²⁺ [26], YAG:Dy, Er [88], ZnO [14] in a simple air jet, and ZnO in water [44], at a seeding density in the order of 10^{11} particles/m³ shows trivial effects from multiple scattering, whilst achieving a reasonable spatial resolution.

SLIPI for ratio-based methods: linear operation

SLIPI has been applied to denoise two-colour, intensity-ratio based techniques such as 2D-LIF [82] and LIF/Mie planar droplet sizing [83, 89]. Considering a linear signal response to laser fluence for a two-colour thermometry at both channels, the signal intensity $I_{i,\lambda}$ obtained for wavelength λ is given by

$$I_{i,\lambda} = I_{DC} + \underbrace{G(\lambda, T)F}_{I_{AC}} \quad (4.5)$$

where G is the gain function and

$$F = F_0[\cos(2\pi v y + \Phi_i) + 1] \quad (4.6)$$

is the local fluence as a function of y . Since laser extinction is a separate problem from multiple scattering or SLIPI, we do not consider it in the present study, although it could be added into the model without difficulty. After the SLIPI operation

$$I_{s,\lambda} = G(\lambda, T)F_0 \quad (4.7)$$

The signal ratio between two selected channels gives

$$\frac{I_{s,\lambda_1}}{I_{s,\lambda_2}} = \frac{G(\lambda_1, T)}{G(\lambda_2, T)} \quad (4.8)$$

The local temperature can be extracted from the signal ratio according to the above equation, after the effects from the unmodulated signal I_{DC} have been removed by SLIPI. Mathematically, the application of SLIPI on the ratio-based methods does not create any bias so long as the signal growth is linear with the laser fluence.

SLIPI signals for ratio-based methods: non-linear operation

For inelastic scattering phenomena such as fluorescence and phosphorescence, a non-linear signal increase with respect to fluence can usually be observed beyond a certain value of the excitation laser fluence. In the case of phosphorescence, the linear emission regime of most commonly used phosphors is limited to a very low fluence range, which is followed by a gradual saturation. In this scenario, Eq. (4.5) is rewritten as

$$I_{i,\lambda} = I_{DC} + \underbrace{G(\lambda, T, F)F}_{I_{AC}} \quad (4.9)$$

The gain function G now brings non-harmonicity to the sub-signal I_i , since the latter becomes a function of a non-unity power of F . The harmonic analysis depends on the linearity, and is therefore no longer valid. In the present analysis, we take the gas-phase phosphor thermometry as a background scenario and simulate artificial LIP images incorporated with experimentally obtained response curves to clarify the biases introduced by SLIPI due to non-linear signal response, and how to account for them in the final temperature retrieval.

4.2 Numerical method

4.2.1 PIV Synthetic Image Generator (SIG)

We use synthetic LIP images generated by a Matlab program adapted from the PIV synthetic image generator (SIG) [90]. SIG was developed as an open-source program and has been widely used as a tool to synthesize PIV image pairs based on a user-defined velocity field. It allocates random positions to individual particles, whose size and intensity information depends on the input particle size distribution, laser profile, and other optical settings. The SIG program is now a standard tool for evaluating advanced PIV algorithms, quantifying uncertainty, or estimating parameters during the experimental design stage. Examples of the application of SIG or similar versions can be found in [91] and [92]. In the present study, the original algorithm is adapted to generate phosphorescent particle images on a single frame based on a user-defined temperature field, rather than Mie scattering, by incorporating phosphorescence responses of ZnO obtained from the previous experiment described in [77].

4.2.2 Adapted SIG for phosphor particles (LIP-SIG)

In the simulation, we consider particles of characteristic diameter smaller than $2 \mu\text{m}$, which are typical of the required short response time to the changes in local temperature and velocity in turbulent gaseous flows [16]. A particle in this size range is much smaller than a typical pixel pitch size in typical fields of view of the order of several centimetres, with resolutions of the order of tens of micrometres, and thus can be viewed as a point light source. For diffraction-limited lenses, the intensity profile of a point light source projected on the image plane obeys the Airy pattern, which can be approximated as a Gaussian function [93]. Note that the Airy disk theory works for both Mie scattering and phosphorescent emission. The intensity distribution of a single phosphor particle image on the object plane is written as a Gaussian distribution,

$$I_p(r) = A \exp\left(-\frac{r^2}{2\sigma^2}\right) \quad (4.10)$$

where r is the distance to the centre point of the light source. In the LIP-SIG method, we assume all particle images are circular, with a diameter d_τ (in pixels), defined as e^{-2} diameter of the particle image intensity distribution, so that

$$\sigma = d_\tau/4 \quad (4.11)$$

The dimension d_τ of diffraction-limited particle images is mainly determined by the optical lenses used in the setup, specifically by the magnification factor M_0 and the f -number, which are assumed to be the same for all particles in the plane. Other factors such as collected wavelength, characteristics of detector, particle sizes, and so on, could also affect the degree of diffraction to some extent. Here we directly define a particle image size d_τ , instead of calculating it from the factors above. However, when using the LIP-SIG program to design an experiment, those factors can be added directly into the code. After pixelization, the intensity of pixel $[x_i, y_i]$ can be obtained by 2D integration of the Gaussian intensity profile over the pixel,

$$\begin{aligned} I_p[x_i, y_i] &= K d_p^2 \int_{x_i - f_{rx}/2}^{x_i + f_{rx}/2} \exp \left[-\frac{1}{2} \left(\frac{x - x_p}{d_\tau/4} \right)^2 \right] dx \\ &\quad \cdot \int_{y_i - f_{ry}/2}^{y_i + f_{ry}/2} \exp \left[-\frac{1}{2} \left(\frac{y - y_p}{d_\tau/4} \right)^2 \right] dy \\ &= \frac{K \pi d_p^2 d_\tau^2}{128} \left[\operatorname{erf} \left(\frac{x - x_p + f_{rx}/2}{\sqrt{2} d_\tau/4} \right) - \operatorname{erf} \left(\frac{x - x_p - f_{rx}/2}{\sqrt{2} d_\tau/4} \right) \right] \\ &\quad \cdot \left[\operatorname{erf} \left(\frac{y - y_p + f_{ry}/2}{\sqrt{2} d_\tau/4} \right) - \operatorname{erf} \left(\frac{y - y_p - f_{ry}/2}{\sqrt{2} d_\tau/4} \right) \right] \end{aligned} \quad (4.12)$$

where K is a calibration constant; (x_p, y_p) is the position of the point light source in the non-pixelized coordinate, and d_p denotes the physical diameter of the particle (in μm). The fill ratios f_{rx} and f_{ry} indicate the ratio of the sensitive area to the total area of a pixel, determined by the chip architecture, and is a user-defined input parameter in SIG [90]. In Eq. (4.12), we follow the assumption made in the original SIG program that the signal strength I_p is proportional to the square of particle diameter d_p . Yet for phosphorescence, the

relation between particle size and emission strength has not been conclusively determined by experimental studies. Here, particles are assumed to be monodispersed so that the variation in particle size d_p does not affect the analyses.

In order to save computational time, for each particle we only calculate the pixel intensity within a $d_\tau \times d_\tau$ region centered at the particle position,

$$\begin{aligned} x_p - \lceil d_\tau/2 \rceil &\leq x_i \leq x_p + \lceil d_\tau/2 \rceil; \\ y_p - \lceil d_\tau/2 \rceil &\leq y_i \leq y_p + \lceil d_\tau/2 \rceil. \end{aligned} \quad (4.13)$$

as the pixel intensity outside this region is an order of magnitude lower than that of the brightest pixel, which is hence set to zero. The phosphorescence signal is, in general, not sufficiently strong to saturate the CCD sensors, so over-exposure is not considered in the modified LIP-SIG code. The final image intensity is assumed to be a linear sum of the intensity generated by all N particles at a given location:

$$I[x_i, y_i] = \sum_{n=1}^N I_{p,n}[x_i, y_i]. \quad (4.14)$$

The number of particles N is related to the volumetric seeding density n_p by

$$n_p = N/(A\delta) \quad (4.15)$$

where A is the area of the simulated image and δ the thickness of the laser sheet. Considering a common level of pixel resolution at $20 \mu\text{m}/\text{pixel}$ and a 0.3 mm thick laser sheet, 5000 particles on a 200×200 pixel simulation area corresponds to a seeding density $n_p = 1.0 \times 10^{12}$ particles/ m^3 . This seeding density is about one order magnitude higher than the normal seeding level for PIV measurements (10-15 particles per window), and is where multiple scattering may start to affect LIP measurements [14]. In the original SIG code there is an implicit limit on the seeding density, defined by the speckle mode generated by interference patterns from coherent particle scatter when the seeding density is high. This limit is not expected to appear in LIP images, as phosphorescence emission is incoherent. Hence, the

LIP-SIG can be applied to investigate seeding cases even under conditions where severe multiple scattering is most likely to occur.

4.2.3 Emission behaviour dependence on temperature and laser fluence

An experimentally obtained calibration function of phosphorescent emission against temperature and local laser fluence has been built into the LIP-SIG program. For the most commonly used phosphors BAM:Eu²⁺ and ZnO, the emission intensity increases with laser fluence before reaching a plateau, and decreases with higher temperature due to thermal quenching. The intensity ratio at two selected wavelengths strongly depends on the local temperature, but was also found to be a weak function of laser fluence [26, 44, 94]. In this numerical study, we use the experimental data on the signal obtained from ZnO previously acquired in [77] to define the response curve $G(\lambda, T, F)F$ for the phosphorescence signal obtained as a function of temperature T and fluence F . Fig. 4.3 shows the response curves measured at 350 K.

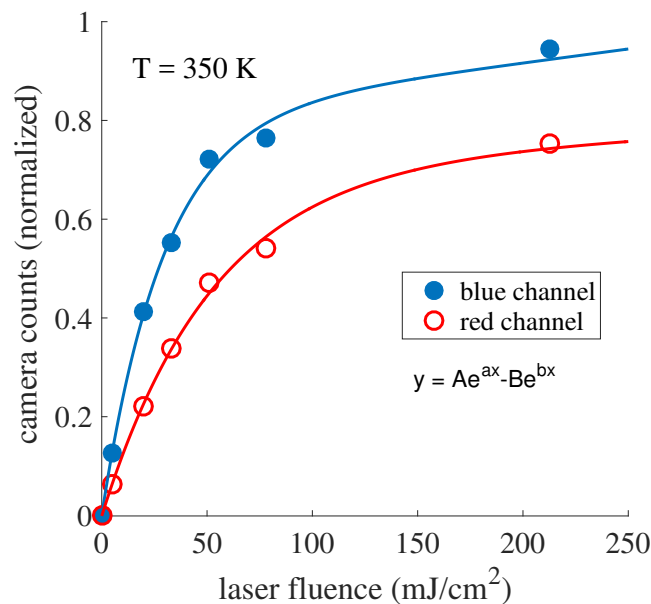


Fig. 4.3 Experimentally obtained response curves for ZnO at 350 K. *Blue circles* are data points collected at the blue channel and *red circles* at the red channel. The *lines* shows the corresponding two-term exponential fittings of the form $y = Ae^{ax} - Be^{bx}$.

Two wavelengths are typically selected for extracting the temperature, λ_r and λ_b , referred as blue (b) and red (r) channel respectively. The choice is usually driven by the maximum sensitivity of the intensity ratio to the temperature, in order to maximize the accuracy of the inversion. For the present response curves, the blue channel spans 387 ± 5.5 nm and the red channel, 425 ± 25 nm. The intensity given by Eq. (4.12) at pixel $[x_i, y_i]$ is assumed to be proportional to the original Gaussian intensity for one particle, local fluence F and the gain function $G(\lambda, T, F)$.

$$I_{p,\lambda}[x_i, y_i] = K_0 G(\lambda, T, F) F \quad (4.16)$$

$$\cdot \int_{x_i-1/2}^{x_i+1/2} \exp \left[-\frac{1}{2} \left(\frac{x - x_p}{d_\tau/4} \right)^2 \right] dx$$

$$\cdot \int_{y_i-1/2}^{y_i+1/2} \exp \left[-\frac{1}{2} \left(\frac{y - y_p}{d_\tau/4} \right)^2 \right] dy$$

where $I_{p,\lambda}[x_i, y_i]$ is the intensity at pixel $[x_i, y_i]$ collected at a given wavelength for a single particle, and the fill ratio f_r is assumed to be equal to unity for simplicity in both x and y directions. The emission intensity was measured for a flow at a constant temperature for a fixed particle concentration, to yield a calibration constant connecting the measured value corresponding to the sum of particle intensities, on the premise that all monodisperse particles have the same response to the constant temperature and fluence. The pixel intensity for a given particle, collected at a different wavelength, is given as

$$I_{p,r}[x_i, y_i] = R_{rb} I_{p,b}[x_i, y_i] \quad (4.17)$$

where R_{rb} is the calibrated signal ratio curve for the red over blue wavelength channels, which is generally also a function of temperature T and laser fluence F . Here we must make the assumption that the diffraction pattern captured by the two cameras (red and blue) is identical, even though this may not be the case for real LIP images. Due to slight differences in spatial resolution, angle of light collection, and sub-pixel misalignment of cameras, the same particle image in general appears differently on the two channels. However, in all studies

so far, a moving average filter was applied to smooth out discrepancies in the diffraction pattern before the ratio is taken between the intensity in the two channels, sacrificing spatial resolution for realizability. Therefore the assumption made here does not create effective discrepancies between simulations and real two-colour LIP measurements in gaseous flows.

With these steps, the response of phosphor emission to temperature and laser fluence was built into the LIP-SIG program. The code can now synthesize random pairs of LIP images based on an input laser profiles and temperature field.

4.2.4 SLIPI subimage generation and image reconstruction

In this subsection, the process of SLIPI subimage synthesis and recovery using the LIP-SIG code developed above is described. It is assumed that the time interval between pulses is sufficiently short (usually several microseconds) so all phosphor particles can be approximated to be static during the three pulses, as would be the case in an instantaneous SLIPI test.

The flowchart in Fig. 4.4 schematically describes the process of SLIPI subimage synthesis and recovery. All simulations were conducted over a 200×200 pixel area. Three horizontally harmonic-modulated laser profiles $F(y)$ were defined at phase angles of 0 , $2\pi/3$, $4\pi/3$, respectively. Fifty single shots were synthesized for each case. A total number N of particles were generated for each single-shot, and a random position (x_p, y_p) was allocated to each particle. Under the assumption of static particles, i.e., particles remain in the same position on all three sub-images, convergence can always be achieved for the SLIPI calculation. For moving particles, which is usually the case for SLIPI based on averaged subimages, 20 single-shots are sufficient to converge the temperature extraction for $N = 5000$, as shown in Fig. 4.5. A uniform temperature field of 350 K in the measurement plane was used in this example. For the purpose of demonstration, for this case we assume a linear signal response as Eq. (4.5). Based on Eqs. (4.14), (4.16), and (4.17), the three sets of SLIPI subimages were simulated and averaged for both channels, as shown in Fig. 4.4(b). Synthesizing three sets of subimages with $N = 5000$ particle images on each single shot took about 2 minutes on a desktop PC. We do not apply any camera noise to the synthetic images for simplicity.

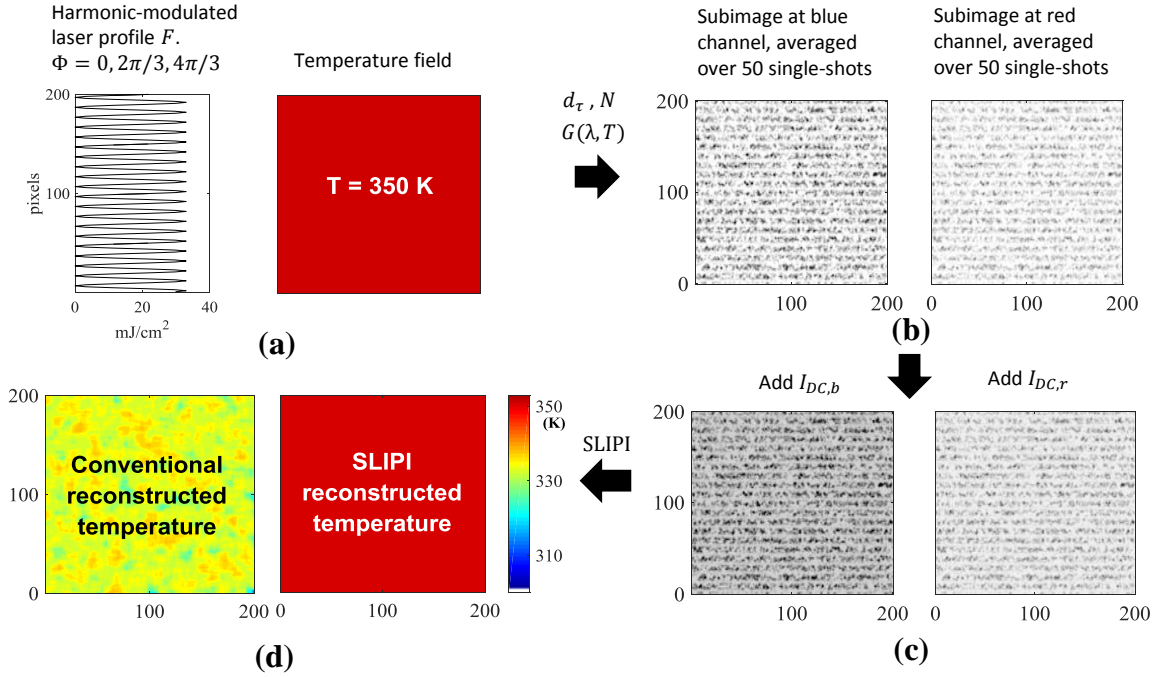


Fig. 4.4 Flow chart for SLIPI image synthesis and reconstruction for linear signal behaviour: (a) definition of a modulated laser profile F and a uniform temperature field (350 K); (b) generation of 50 single-shots SLIPI images (200×200 pixels) using the number of particles ($N = 5000$), using a fixed gain function $G(\lambda, T)$; (c) addition of constant synthetic signals $I_{DC,b}$ and $I_{DC,r}$ to the two channels; (d) extraction of temperature field from conventional and SLIPI reconstructed image. As expected, the SLIPI operation corrects the temperature bias caused by intentionally added unmodulated signals I_{DC} .

To illustrate the working principle of SLIPI, in the present case, a constant baseline signal I_{DC} was intentionally added to the subimages on both channels to simulate multiple scattering. Three averaged SLIPI subimages corresponding to the three spatial modulation angles, I_0 , $I_{2\pi/3}$ and $I_{4\pi/3}$, were generated there with the presence of uniform multiple scattering, as shown in Fig. 4.4(c).

Finally the SLIPI and the conventional images were recovered from the three subimages using Eqs.(4.2) and (4.3). The intensity ratio was translated into temperature by the calibration function $R_{rb}(T, F)$, as shown in Fig. 4.4(d). The SLIPI recovered image clearly recovers the target temperature (350 K), whilst the temperature measured without the SLIPI correction yields a biased value.

The description in Fig. 4.4 indicates the process under which SLIPI works correctly to extract the original signal. The purpose of this study is to investigate the effects of SLIPI

signal retrieval on the true signal when realistic curves for phosphorescence yields are used, rather than the effectiveness of SLIPI in removing I_{DC} . Hence in the following simulations and analyses I_{DC} is set to zero.

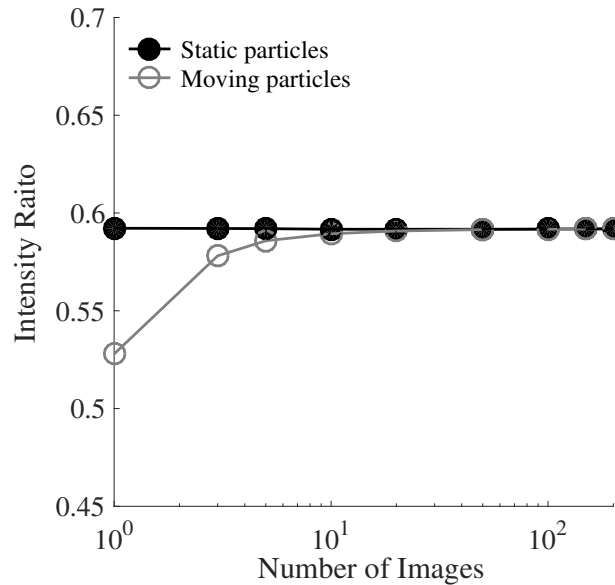


Fig. 4.5 A convergence study of intensity ratio as a function of number of images averaged for SLIPI algorithm. $N = 5000$ for each single shot (0.125 particle/pixel). For static particles, as we assumed in this study, convergence can always be achieved; For moving particles, 20 images are sufficient to converge the temperature extraction for this high seeding level.

4.3 Effect of non-linearity on signal yield

The linear behaviour of the phosphorescence signal with laser fluence is limited to a low fluence range, which followed by a slow saturation. For example, the measured linear response of BAM:Eu²⁺ particles ends at 2-3 mJ/cm², and the corresponding emission saturates at fluences around 200 mJ/cm² [26]. Similarly, the linear response limit and the saturation point for ZnO phosphorescence appears around 50 and 250 mJ/cm², respectively (see Fig. 4.3). To guarantee a robust signal to noise ratio, it is common to choose a laser fluence beyond the linear growth regime for phosphor thermography, for example ~ 100 mJ/cm² for BAM:Eu²⁺ in [16]. However, the non-linear signal yield causes a problem

for SLIPI, namely, distorted sinusoidal modulation on subimages [95] and the presence of higher order harmonics on the SLIPI reconstructed image [96]. In what follows, the effect of non-linearity for LIP on temperature measurements is investigated. In this section, we consider a special case where the intensity ratio R_{rb} is insensitive to laser fluence, that is

$$\frac{G_r(F, T)}{G_b(F, T)} = R_{rb}(T) \quad (4.18)$$

This may be true for some thermographic phosphors, such as Sn-doped phosphor [97]. In contrast, for ZnO and BAM:Eu²⁺, the signal ratio also changes with excitation fluence, as discussed in the following section.

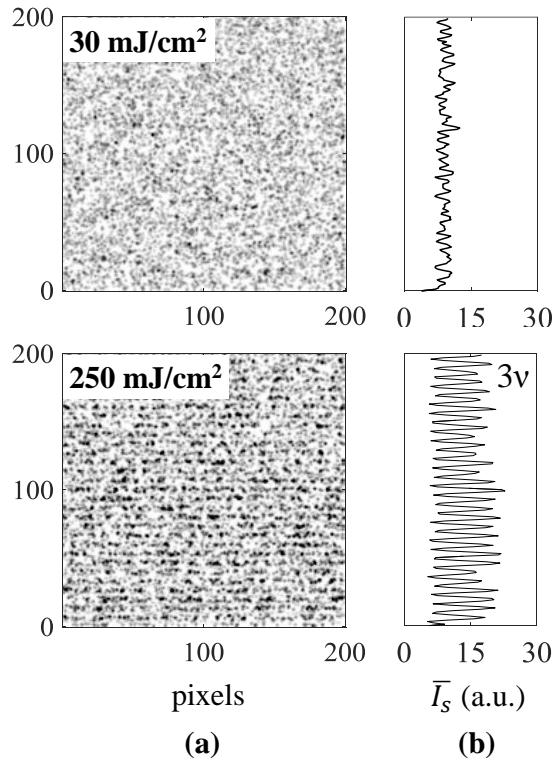


Fig. 4.6 (a) Reconstructed SLIPI image on blue channel for two selected test fluences (peak fluence). The *upper row* shows the case for 30 mJ/cm² (linear regime) and the *bottom row* for 250 mJ/cm² (close to saturation); (b) horizontally averaged intensity profile of the SLIPI reconstructed image. Residual noise can be observed for the case of 250 mJ/cm² at a frequency of 3ν, where ν is the spatial frequency of the Ronchi grating modulation;

For this special case, the image on the blue channel was synthesized first, and the image on the red channel was then synthesized correspondingly by multiplying a constant signal ratio R_{rb} to the blue channel. Two test fluences are selected, one in the linear range (fluence 30 mJ/cm^2) and the other in the saturation range (250 mJ/cm^2). The maximum values represents the maximum fluence used in the modulated laser sheet. As expected, when a high fluence is applied, high order residual noise can be observed on SLIPI recovered image (Fig. 4.6(a) *bottom row*), whilst the noise is trivial for the low fluence case where the signal response is still in the linear regime (Fig. 4.6(a) *upper row*). The high order noise is caused by the non-harmonicity in the subsignals. The FFT analysis shows that the frequency of this residual noise is exactly three times the ground frequency ν (frequency of the Ronchi grating). However, since each term in Eq. (4.2) is multiplied by the same factor, the residual noise cancels out automatically when calculating the ratio between the SLIPI recovered images at the two channels:

$$\frac{I_{s,r}}{I_{s,b}} = \sqrt{\frac{(R_{rb}I_{1,b} - R_{rb}I_{2,b})^2 + (R_{rb}I_{1,b} - R_{rb}I_{3,b})^2 + (R_{rb}I_{2,b} - R_{rb}I_{3,b})^2}{(I_{1,b} - I_{2,b})^2 + (I_{1,b} - I_{3,b})^2 + (I_{2,b} - I_{3,b})^2}} = R_{rb} \quad (4.19)$$

The resulting temperature fields retrieved from simulations at both 30 and 250 mJ/cm^2 cases are unbiased. Although the temperature retrieval is not affected by the non-linearity in the signal response, a problem regarding the signal strength was identified during the simulation. For harmonic subsignals, I_s should be equal to the amplitude of the true signal A as denoted in Eq. (4.2). For the present non-linear response curves, we calculate the average intensities of SLIPI recovered image under various excitation fluences and compare them with A , which is plotted in Fig. 4.7. However, a discrepancy can be observed between A and I_s , which gradually increases with excitation fluence. This is due to the fact that the SLIPI operation rejects non-linear signal gain: in essence, SLIPI acts as a spatial bandpass filter that only preserves the signal energy at the ground frequency (Ronchi grating); at high excitation fluences, the energy of non-linear signal gain is contained at frequencies other

than the fundamental spatial frequency, which is removed in the reconstruction produced by SLIPI. This has two major consequences for LIP measurements:

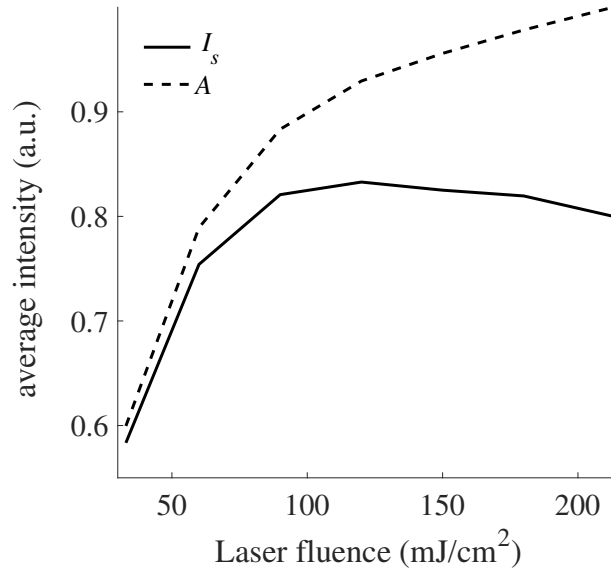


Fig. 4.7 A the amplitude of true signal (*dotted line*) and the average intensity I_s (*solid line*) as a function of laser fluence on blue channel. For linear response, I_s should equal to A . However for the present non-linear response curves, a discrepancy between I_s and A is identified.

Firstly, when SLIPI is applied to phosphorescent emission, the signal strength of the SLIPI recovered image is reduced. In particular, this may be a severe problem for BAM:Eu²⁺, whose linear response ends at a very low fluence (2-3 mJ/cm²) and saturates at a very high fluence (200 mJ/cm²). The low SNR issue has been reported in [42], but was attributed to the subtraction algorithm of SLIPI subimages in that work. From the simulation presented in this study, another possible explanation seems to be that SLIPI removes the non-linear component in the signal, which represents a considerable part in phosphorescence emission from BAM:Eu²⁺. This creates a dilemma to the application of SLIPI to LIP: on one hand the temperature bias due to multiple scattering can be successfully removed by SLIPI, on the other hand the SNR after SLIPI operation means poor precision in the temperature calculation. In general, the low SNR problem can be solved by collecting and averaging over more samples; for instantaneous SLIPI, however, other signal boosting techniques may

be necessary to overcome the low SNR problem. The issue of SNR needs to be evaluated carefully prior to the use of SLIPI on phosphor thermography.

Secondly, the removed non-linear component of the phosphorescence signal is recognized as spurious signal and labeled as multiple scattering. Consequently, the degree of multiple scattering will always be overestimated unless the signal response is in the strictly linear regime.

4.4 Effect of intensity ratio changes to laser fluences

In the case of most frequently used thermographic phosphors such as BAM:Eu²⁺ and ZnO, the intensity ratio is also a function of laser fluence [26, 44, 77, 94]:

$$\frac{G_r(F, T)}{G_b(F, T)} = R_{rb}(F, T) \quad (4.20)$$

This undesirable emission characteristic is usually avoided by using a top-hat laser sheet to obtain constant fluence, or conducting a flat-field correction at room temperature under the same flow configuration. However, to conduct SLIPI, the laser profile is intentionally modulated, so the fluence ranges from zero (ideally) to a maximum value over the test section, which may bias the measured temperature field spatially. Therefore, if the ratio of gains at the selected two channels is not constant with fluence, there could be a problem for SLIPI.

We start by considering a case where the signal remains in the linear region, for up to 30 mJ/cm², with a spatial modulation of 20 pixels, and a constant temperature field of 350 K. No multiple scattering or camera noise was added to the synthetic images. In this case we consider the dependency of intensity ratio to the local fluence, shown in Fig. 4.8(a). Although the reconstructed SLIPI image does not show any obvious residual streaks on either channel (Fig. 4.8(b)), the modulated laser profile leaves its signature onto the temperature field (Fig. 4.8(c)), which was extracted based on the calibration curve measured at 30 mJ/cm². The frequency of the modulation on the temperature field is 3v, which causes a spatial temperature root means square fluctuation of around 3 K. These streaks can be of course

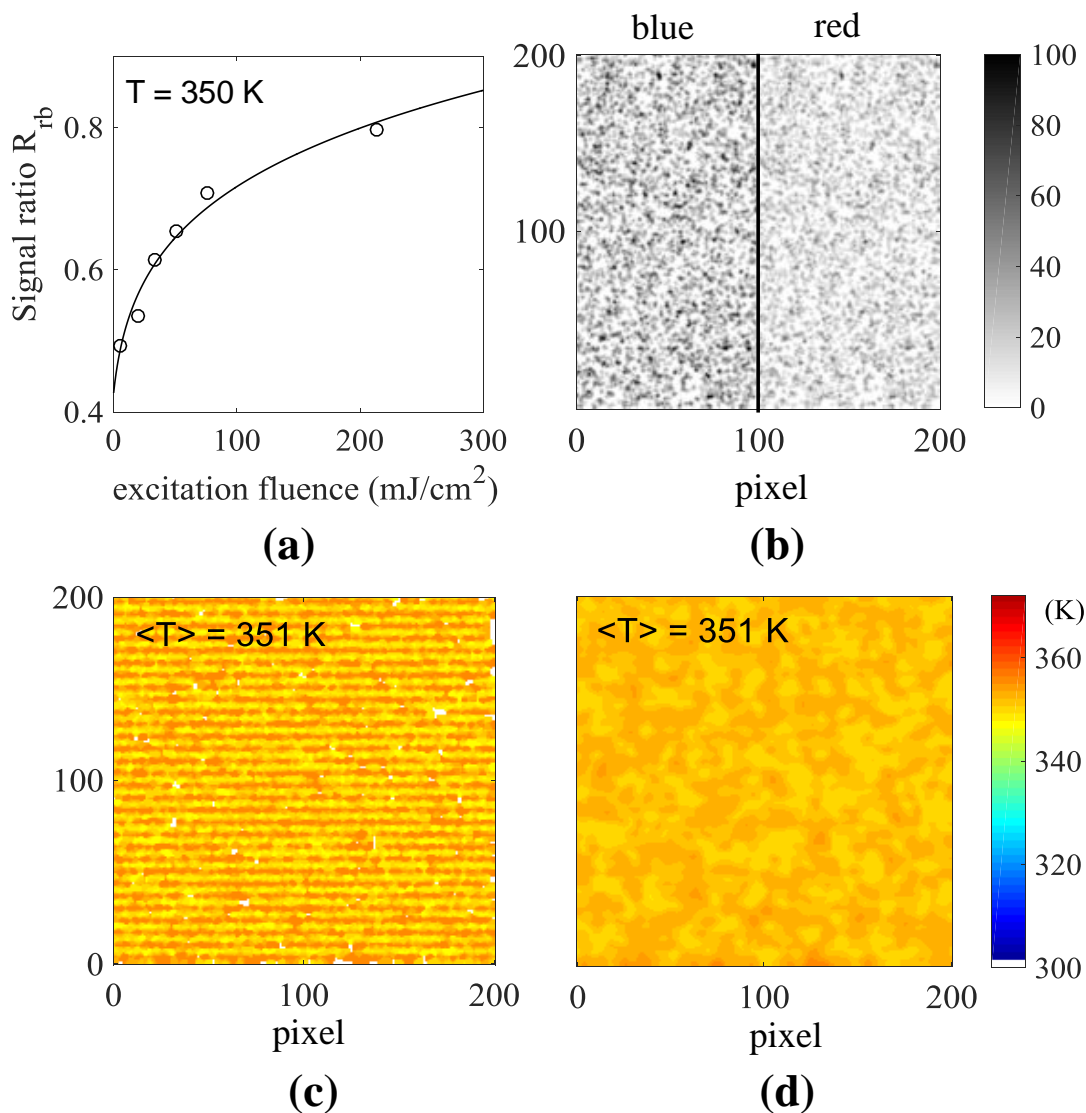


Fig. 4.8 (a) Intensity ratio R_{rb} as a function of laser fluence at 350 K, based on experimental data collected from ZnO. *Circles* are averaged data points, and the *curve* is the best fit to the data points; (b) reconstructed SLIPI images for the two channels; (c) temperature field extracted from the reconstructed SLIPI images, and (d) after a low pass field was applied to (b), the streaks on temperature field are removed. For this case, $N = 5000$, period of modulation is 20 pixels, the laser fluence is $30 \text{ mJ}/\text{cm}^2$.

removed by applying low pass filters to the reconstructed SLIPI image on both channels (Fig. 4.8(d)). However, this reduces the temperature spatial resolution.

The mean temperature extracted from the SLIPI reconstructed image is 1 K higher than the target temperature, as shown in Fig. 4.8(c). However, if the laser fluence is gradually increased until the signal saturates, the temperature bias increases quickly. Fig. 4.9 shows the temperature (spatially averaged) extracted from the SLIPI and conventional images as a function of the excitation fluence, named as T_s and T_c respectively. Both T_s and T_c are biased, but towards opposite directions. The bias in T_s is explained as follows: since SLIPI removes non-linear components from the true signal, considering the signal ratio curve to laser fluences (one channel saturates faster than the other), the amount of signal removed by SLIPI from each channel is non-proportional; after subtracting the non-linear signal from the two channels, the signal ratio changes, and leads to a biased temperature measurement.

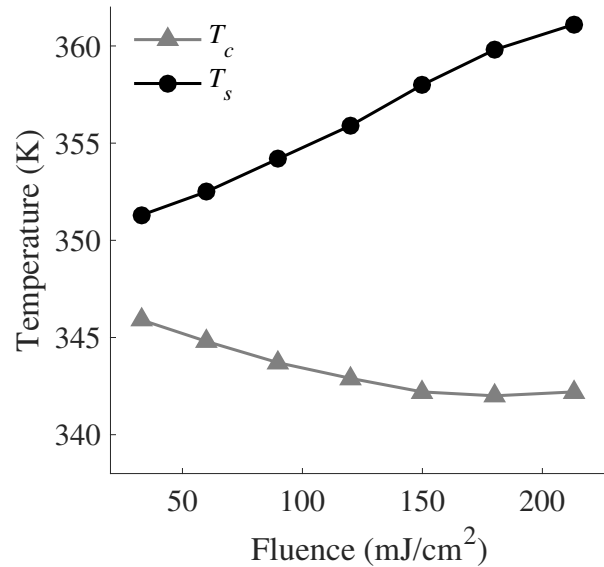


Fig. 4.9 Temperature extracted from conventional (T_c) and SLIPI images (T_s) as a function of excitation fluence. No multiple scattering was applied to the synthetic images, so the temperature bias is purely caused by the saturating emission characteristics of ZnO. For the cases simulated in this figure, $N = 5000$, $T = 350$ K, and the period of modulation is 20 pixels.

A bias in T_c of about 5 K is observed even at a low fluence values of ~ 30 mJ/cm², where the signal response curve still appears to be quite linear (see Fig. 4.3). It suggests that the

conventional images are susceptible to even slight non-linearity in the emission response, as it accumulates the error in the signal shape by adding up three subsignals. This also causes a problem in estimating the degree of multiple scattering, which is described in Section 4.5.

Fig. 4.8 shows the temperature bias for SLIPI using ZnO particles. BAM:Eu²⁺, however, yields a contrasting emission behavior to ZnO: it is a blue-shifted phosphor as temperature increases, and the red channel saturates faster than the blue channel. Hence for SLIPI performed with BAM:Eu²⁺ particles, in theory T_c will be biased to a larger value and T_s to a smaller value.

In general, the temperature reconstruction is not affected by SLIPI for phosphors for which the signal ratio is insensitive to local fluence, as demonstrated in Section 4.3. However, for those that are not, the problems described may appear. In such cases, a low excitation fluence should be selected to minimize the temperature bias. Otherwise a numerical study using the LIP-SIG program incorporated with calibration data acquired from a simple jet may be necessary to estimate the temperature uncertainty brought on by application of SLIPI. For two-color fluorescence thermometry [8], a similar problem may exist if the laser fluence partially or fully saturates the fluorescent tracer. The result of SLIPI on planar droplet sizing [9] could also be affected, since Mie scattering always scales linearly with the laser fluence, whereas the fluorescence is not. Consequently, the ratio between LIF and Mie may be biased. A thorough analysis of the effects of SLIPI on LIF systems would be possible if LIF response curves were available.

4.5 Degree of multiple scattering

Kristensson and co-workers [81] used Eq. (4.4) to determine the relative amount of light being suppressed by SLIPI. In the following work by Zentgraf *et al.* [42], the same equation was applied to quantify the level of multiple scattering in LIP images, and reported a very high 40% contribution to the total signal. In this study, we calculate the degree of multiple scattering on reference SLIPI subimages synthesized without multiple scattering ($I_{DC} = 0$),

and investigate how the signal response affects the estimation. Two reasons that may lead to an inaccurate estimate on the degree of multiple scattering are discussed as follows.

4.5.1 Overestimation caused by non-linear signal yield

As shown earlier, I_c is very sensitive to the non-harmonicity in the signal. If the signal gain is non-linear, then

$$I_c > A + I_{DC} \quad (4.21)$$

This is usually the case in real experiments for both LIP and LIF. In such cases, $(I_c - I_s)/I_c$ overestimates the degree of multiple scattering ϕ . Meanwhile, part of the non-linear gain is rejected by the SLIPI operation. This further biases ϕ to a higher value, since part of the true signal is recognised as multiple scattering and removed from I_s .

4.5.2 Overestimation caused by particle image diffraction

A particle usually appears larger than its physical size on the image due to diffraction. The diffraction pattern does not follow the imposed sinusoidal modulation, but instead leads to a localised blur on the intensity pattern. This effect is interpreted by SLIPI as multiple scattering. For particles of the same size d_p , we compared a case where diffraction was dominant ($d_\tau = 4$ pixels) with a case where it was trivial ($d_\tau = 1$ pixel), which can be achieved by changing the optical settings in a LIP experiment. Other assumed parameters were: 10 pixels of modulation wavelength, a total number of 5000 particles on each single shot, a uniform temperature of 350 K, and a low laser fluence of 30 mJ/cm² so as to maintain a linear signal response. After the SLIPI operation, the degree of multiple scattering for the two channels was reckoned as $\phi_b = 23.6\%$ and $\phi_r = 17.9\%$ for $d_\tau = 4$ pixels; whereas for $d_\tau = 1$ pixel, $\phi_b = 12.8\%$ and $\phi_r = 6.4\%$. The disparity between the two cases is caused by the different levels of particle image diffraction. Mathematically, the overall signal on the averaged subimages no longer corresponds to a sinusoidal shape. Thus, part of the signal energy is removed by SLIPI, which further weakens the SNR of the recovered images. This comes as no surprise, because the initial purpose of the SLIPI technique was to overcome

the diffraction limit in microscopic imaging and thus to achieve a theoretically unlimited resolution [96].

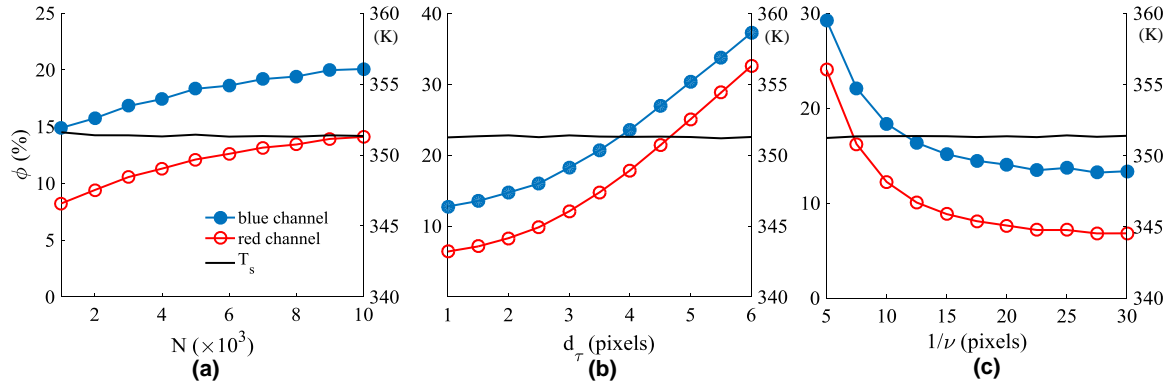


Fig. 4.10 Spurious degree of multiple scattering ϕ reported by SLIPI in both blue (*blue circles*) and red (*red circles*) channels for reference synthetic LIP images where zero multiple scatter signal was added, as a function of (a) particle number N , (b) particle images diameter d_τ , and (c) period of laser sheet modulation $1/\nu$, respectively. For unchanged variables, excitation fluence is 30 mJ/cm^2 , particle number $N = 5000$, laser sheet modulation 10 pixels, and particle image diameter 3 pixels. The temperatures T_s extracted from the SLIPI recovered images are also plotted in the same figure on the y axis on the right side.

SLIPI removes a considerable part of the diffracted signal during the image reconstruction and subsequently yields a spurious degree of multiple scattering. This discrepancy increases with higher particle image density, larger particle image size and narrower fringes, as shown in Figs. 4.10(a), (b) and (c), respectively. The temperature (spatially averaged) extracted from the SLIPI image for corresponding cases is also plotted in the same figure. The signal loss due to particle diffraction does not further bias the mean temperature.

The analysis on particle image diffraction also applies to SLIPI studies on dense sprays or particles. In particular, for the application of SLIPI to sprays [80], the droplet size and concentration varies greatly in the primary and the secondary breakup zone. If SLIPI is applied to resolve the entire spray cone, the amount of true signal removed due to diffraction may be very different along the axial direction, as suggested in Fig. 4.10(a) and (b).

4.6 Simulation uncertainties

The simulation results presented in this Chapter illustrate how SLIPI affects non-linear signal reconstruction and temperature extraction. However, for a specific experiment setup, a quantitative uncertainty analysis requires measurements (or estimations) of input parameters such as camera noise level, particle image density, particle size distribution, the relation between particle size d_p and the strength of phosphorescence emission, laser extinction, etc. Since we did not measure these parameters for the present simulations, the numbers predicted in this study may be different the temperature bias observed in a real SLIPI-LIP experiment.

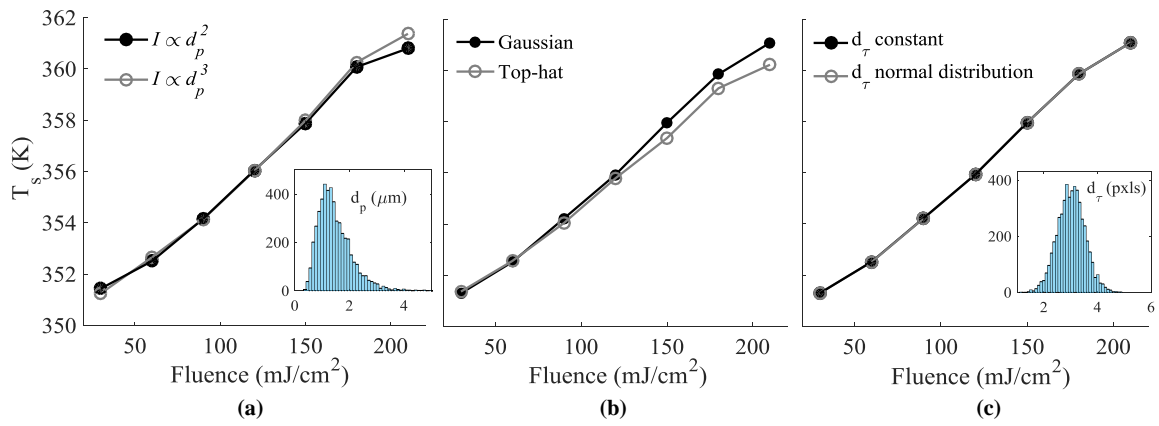


Fig. 4.11 SLIPI recovered temperature T_s as a function of excitation fluences, for (a) an emission intensity in proportional to d_p^2 or d_p^3 ; (b) a Gaussian or top-hat particle image profile; (c) a constant or a varying particle image size d_τ over the simulation field. The distributions of d_p and d_τ are plotted in the subfigures accordingly. Other parameters are kept the same as Fig. 4.9.

Nevertheless, the goal of the SIG-LIP program is to provide quantitative uncertainty analysis for SLIPI-LIP experiments. One important premise for this purpose is the temperature bias predicted by the LIP-SIG program should mainly depend on the input emission curves and excitation fluences, but only marginally on the assumptions made in Section 2. Therefore, we reconduct the simulations for three special cases where the major assumptions are breached, in order to show to how sensitive is the temperature extraction to them: (a) the emission intensity is proportional to either d_p^2 or d_p^3 , whilst d_p follows a lognormal distribution; (b) particle image I_p do not follow a Gaussian profile, but is top-hat; and (c) particle image size d_τ is not constant over the simulation area. Another reason to choose the

above three parameters is that usually they are difficult to measure in real LIP experiments. The T_s curve (SLIPI recovered temperature) in Fig. 4.9 is reproduced for these three special cases, and the result is plotted in Fig. 4.11. In the worst scenario, the disparity in T_s is less than 2 K when using a different assumption. Clearly, changes in the particle size distribution, particle image profile or particle image size distribution have little effects on the measured temperature. The result again shows the major advantage of the intensity-ratio methods: factors that may affect the absolute intensity cancel out automatically, leaving the spectrum shift to play its role on temperature extraction.

4.7 Possible applications of the LIP-SIG program

As illustrated, there are several possible applications of the modified LIP-SIG program, as follows.

Firstly, the LIP-SIG program can provide guidance to experimentalists performing SLIPI. For example, Fig. 4.5 shows at least 20 image should be averaged to achieve convergence for a particle image density of 0.125 particles/pixel. If a particle seeding density below this level is used, more images should be acquired to converge the SLIPI calculation, which can be predicted by the LIP-SIG program.

Secondly, the simulations allow the estimation of the expected degree of multiple scattering in LIP images. As demonstrated earlier, due to non-linear signal gain and particle diffraction, SLIPI overestimates the contribution from multiple scattering in real experiments. The LIP-SIG program can show how much of the true signal will be removed during the SLIPI operation, by synthesizing noise-free reference SLIPI subimages under the same test conditions with experimental calibration data. The true degree of multiple scattering can then be determined by subtracting the spurious degree of multiple scattering ϕ from the measured value.

Thirdly, the simulations allow an assessment of the the temperature bias caused by SLIPI. If the emission spectrum of phosphor particles is sensitive to the excitation fluence, the measured temperature may be biased by the SLIPI operation, especially for cases with a high

laser fluence. In such cases, the LIP-SIG program can help identify the potential temperature bias for the test condition, which can be used to correct the measured value or to facilitate an uncertainty analysis.

Fourthly, it becomes possible to investigate preferential re-absorption. The signal spectrum from the measurement plane is irreversibly changed by re-absorption before it reaches the detector, which in principle cannot be corrected by SLIPI. If changes in the intensity ratio introduced by low SNR and non-linear signal yield have been estimated by LIP-SIG and eradicated from the measured value, the remaining discrepancy in the intensity ratio measured in a low-seeding and a high-seeding (with SLIPI) case should, in principle, be due to the preferential re-absorption. This discrepancy should also show a correlation to the local temperature. Since changes in local temperature shift the emission spectrum, the overlapping wavelength band will either be broadened or narrowed, which then amplifies or suppresses the preferential re-absorption. Demonstrating the correlation between residual temperature bias and spectrum shift experimentally on both ZnO and BAM:Eu²⁺, with the help of LIP-SIG program, can be a strong proof of the existence of preferential re-absorption.

Finally, the same procedure can allow an estimation of PIV uncertainty which would result from the use of fluorescent tracers. The LIP-SIG program can be easily adapted to simulate fluorescent particles as velocity tracers, which have been widely applied in micro-PIV for biological studies. This can be used to investigate the effects such as out-of-focus particle images on the measurement accuracy, which is a common problem for micro-PIV because the imaging system for this application usually has a very narrow depth of field.

4.8 Conclusions

This study investigates the potential effects that structured laser illumination planar imaging (SLIPI) may have on the accuracy of gas-phase phosphor thermography. A LIP-SIG program is developed and combined with signal yield functions obtained from experimental data with ZnO to generate artificial LIP images. The SLIPI process is simulated by generating LIP

images under sinusoidally modulated laser sheets, and then recovering the target temperature field from these images. The main findings are summarized as follows:

- For phosphor particles whose emission strength scales non-linearly with the excitation fluence, the sinusoidal modulation is distorted on each subimage. This leaves higher order residual noise on the SLIPI reconstructed image I_s . However, if the signal ratio does not change with laser fluence, the residual noise cancels out automatically when calculating the signal ratio from two channels, and hence does not affect the temperature retrieval.
- When the phosphorescent emission is close to saturation, a substantial amount of true signal energy is removed by the SLIPI operation, because the energy of non-linear signal gain transfers from the ground frequency to other spatial frequencies, which is recognised as undesired signal by SLIPI.
- A complicating situation appears for phosphors whose intensity ratio changes with the excitation fluence, for example ZnO and BAM:Eu²⁺. Residual streaks appear on the recovered temperature field. This can be removed by applying a low-pass filter to the SLIPI reconstructed images which, however, reduces the spatial resolution.
- The mean temperature after SLIPI operation can also be affected by the intensity ratio changes due to modulated laser sheets. If a low fluence is applied to keep the emission in the linear range, the temperature bias is trivial. However, when using high laser fluences ($\sim 200 \text{ mJ/cm}^2$), a larger temperature bias can appear.
- The SLIPI operation is very likely to overestimate the degree of multiple scattering in LIP images, because the non-linear signal yield and particle diffraction are not sinusoidal-modulated, but are identified as multiple scattering by SLIPI. This may occur in SLIPI with LIF and with Mie scattering (particle-based) as well.

Future work will focus on conducting SLIPI-LIP experiments in a well-controlled environment such as in a laminar air jet or in water [97], and comparing the results with those

predicted by the LIP-SIG program. After experimental validation, the program can be applied to investigate more complex scenarios such as two-pulse and one-pulse SLIPI on phosphor thermometry.

Chapter 5

TPIV based on LII signal from submicron black particles: concept and model

5.1 Introduction

As has been introduced in Chapter 1, the application of TPIV is limited by several factors, namely, (a) the high cost of commercial thermographic phosphors with adequate size characteristics, (b) interference from chemiluminescence and black body radiation in highly luminous flames, (c) the phosphorescent signal decreases significantly at temperatures beyond 900 K owing to thermal quenching [39], even for specially formulated phosphors. Current studies on thermographic PIV focus on overcoming some of these difficulties by developing an inexpensive synthesis process for blue-emitting fast phosphors [43], and by investigating the effects of different laser fluences, seeding densities, gas components on the accuracy of temperature measurements for various types of thermographic phosphor in dispersed form [26, 27].

In this chapter, we consider whether it is possible to achieve a similar accuracy in determining temperatures without resorting to phosphorescence, but instead reverting to the well-studied laser-induced incandescence (LII) technique. LII traditionally works by

heating submicron soot particles to sufficiently high temperatures so as to reach a fixed sublimation temperature, allowing the incandescence signal to be dependent primarily on the concentration of particles [98]. Additional information can often be extracted by considering the signal behaviour with wavelength and time, leading to the determination of particle size and temperature [99–101]. However, one can conceive of a technique whereby the energy added is purposefully lower than the sublimation limit of the particles. Under these conditions, the particle temperature reached will be a function of the initial particle temperature and the net total energy absorbed by the particles within a particular time interval. The resulting incandescent emission spectrum therefore reflects the initial temperature (assumed to be in equilibrium with the surrounding gas), and a fixed quantity. The latter can be determined by a calibration procedure, in which the LII signal for a given gas temperature and total energy added is measured, and finally the original temperature of the gas can be determined by subtraction and inversion of Wien's law, as explained further on.

Imaging flame temperature using multi-colour pyrometry is not a new concept. For a rich soot flame, the approximate flame temperature can be measured by the ratio of soot incandescence at two wavelengths [102–104]. However, such measurements are limited to steady and axisymmetric flames, as Abel inversion is involved. For lean flames or regions where soot is not produced, filament pyrometry has been demonstrated by using thin SiC filaments for measurement of the gas temperatures in equilibrium with the filament [105, 103]. Although two-color (2C) soot/filament pyrometry has shown good accuracy, but are rather strictly limited to steady flames, as exposure times of several hundred microseconds are necessary to collect sufficient incandescence signal, which may be too long to resolve turbulent flows. This limitation can be removed by heating soot particles to significantly higher temperatures, using laser pulses as in two-colour LII (2C-LII). Since the incandescence signal is approximately proportional to T^4 , the intensity of LII signal from soot can be one or two orders of magnitude higher than that of natural soot luminosity in a flame, and most of the LII signal is emitted within 1 μs after the initial laser pulse. In the realm of LII studies, 2C-LII is a well established technique to measure the peak temperature that soot particles can reach after the laser pulse excitation [106, 107]. The original purpose of

2C-LII was to determine the difference between soot and ambient temperature so that the primary-particle size distribution can be estimated based on the measured particle cooling rate at this temperature difference. In the present study, 2C-LII is combined with a calibration (either *in-situ* or *ex-situ*) at a reference local gas temperature to determine the gas temperature. Instead of soot, submicron black particles are intentionally seeded into the flow field as tracers, and illuminated using a (preferably top-hat profile) laser sheet. The resulting LII signal can be used to extract temperature by two-color pyrometry using two cameras. The signal, or that from the simultaneous Mie scatter can also be used at the same time to extract the velocity via cross-correlation, using an additional PIV camera.

5.2 Model

In this section we develop the model for LII thermography, which is based on the LII of submicron particles seeded into the flow. The differential equations for the particle temperatures are developed and solved, and the expected incandescence signal is used to extract the underlying gas temperatures. The feasibility and the sensitivity of the technique and its dynamic range are examined based on the numerical integration of the equations, which will be presented in Section 5.3.

5.2.1 Particle temperature

The model for LII signals arising from laser light absorption by soot particles has been well established [98, 108]. In the present study, a simplified LII model is used, which only considers energy absorption, conduction and evaporation, for a situation where the final particle temperatures are kept below the sublimation limit.

In the following paragraphs, we develop the energy balance within the LII non-sublimating regime, and derive an equation for the obtained LII signal. The energy rate balance for the particle reads:

$$\frac{dU}{dt} = \dot{Q}_a + \dot{Q}_c + \dot{Q}_e \quad (5.1)$$

where \dot{Q}_a is the rate of laser light energy absorbed, \dot{Q}_c is the cooling rate by conduction, and \dot{Q}_e is the sublimation rate. The energy transfer rate via other mechanisms such as radiation or oxidation is 3 to 4 orders of magnitude lower than other mechanisms [109], and are therefore neglected. We assume that the particle is sufficiently small for a uniform temperature T_p to be representative, so that the internal energy of the particle of mass m and specific heat capacity c_s is $dU = mc_p dT_p$. If we also assume that the particle is represented by a sphere of diameter d_p , and a density ρ_s , $m = \frac{\pi}{6}\rho d_p^3$.

The rate of heat absorption by a particle from a light source can be expressed as

$$\dot{Q}_a = \sigma_a I_a(t) = \sigma_a F q \quad (5.2)$$

where σ_a is the absorption cross section, I_a is the laser intensity, which can be represented by the mean fluence (energy per unit area) F , and a normalizing temporal shape assumed to be a Gaussian in time, with a peak at τ_0 , and width τ corresponding to one-half of the laser pulse full width at half maximum.

$$q(t) = \frac{1}{\tau\sqrt{2\pi}} \exp\left(-\frac{(t-\tau_0)^2}{2\tau^2}\right) \quad (5.3)$$

If the particle seeded into the flow falls into the Rayleigh regime ($d_p \ll \lambda_L$), the absorption cross-section σ_a can be expressed as

$$\sigma_a = \frac{\pi^2 d_p^3 E(m)}{\lambda_L} \quad (5.4)$$

where $E(m)$ is the refractive index function for absorption, λ_L is the laser excitation wavelength.

The mean free path for gases at ambient pressure is ~ 70 nm, whilst the target tracer for this technique should be $100\sim 200$ nm. Hence the conduction term assumes that the heat conduction between the particle and surrounding gas molecules is in the transition regime between the free-molecular region and the continuum regime, known as the McCoy-Cha

approximation [110]:

$$\dot{Q}_c = -\frac{2\kappa_a\pi d_p^2}{d_p + GL} (T_p - T_0) \quad (5.5)$$

where κ_a is the thermal conductivity of the bath gas, L is the mean free path, T_0 is the temperature of the bath gas, G is a function of the ratio of the specific heats of the bath gas $\gamma = c_p/c_v$, and is given by:

$$G = \frac{2(9\gamma - 5)}{\alpha_T(\gamma + 1)} \quad (5.6)$$

where α_T is the thermal accommodation coefficient.

The sublimation term is presented as the energy carried away by the vaporised mass,

$$\dot{Q}_s = \frac{\Delta H_v}{W_s} \frac{dm}{dt} \quad (5.7)$$

and

$$\frac{dm}{dt} = \rho_s \frac{\pi}{6} \frac{d}{dt}(d_p^3) = \frac{-\pi d_p^2 W_v \alpha_M P_v}{RT_p} \left(\frac{RT_p}{2\pi W_v} \right)^{0.5} \quad (5.8)$$

where ΔH_v is the enthalpy of formation of the sublimed carbon clusters in energy per unit mole, W_s is the molecular weight of solid carbon, W_v is the molecular weight of sublimed carbon, α_M is the mass-accommodation coefficient, P_v is the average saturation partial pressure of the sublimed particle at temperature T_p , and R is the universal gas constant.

In this simulation we used the value for carbon for the above parameters, and their reference are listed in Table 1. The differential equations are solved numerically in Matlab, and the temporal profile of particle temperature $T_p(t)$, and particle size $d_p(t)$ is obtained. Using the particle temperature history $T_p(t)$ obtained from the LII model, the corresponding LII signal emitted at wavelength λ can be calculated by Planck's expression,

$$S(\lambda_s, t) = \frac{8\pi^3 d_p(t)^3 hc^2 E(m)}{\lambda_s^6 \exp\left(\frac{hc}{\lambda k_B T_p} - 1\right)} \quad (5.9)$$

Table 5.1 Simulation Parameters

Parameter	Value/Expression	Reference
c (m/s)	3×10^8	/
c_s (J/kg K)	1900	[111]
E (m)	0.26	[112]
h (J s)	6.626×10^{-34}	/
k_B ($\text{m}^2 \text{kg s}^{-2} \text{K}^{-1}$)	1.38×10^{-23}	/
L (m)	$2.355 \times 10^{-10} T_0$	[111]
P_v (Pa)	$10^5 \exp \left[-\frac{\Delta H_v}{R} \left(\frac{1}{T} - \frac{1}{3915} \right) \right]$	[113]
R	8.3145	/
W_s (kg/mol)	0.012	[111]
W_v (kg/mol)	0.036	[111]
ΔH_v (J/mol)	7.78×10^5	[111]
α_M	1	[111]
α_T	0.3	[114]
γ	1.3 ^a	/
κ_a (W/m K)	0.1068	[99]
τ_0 (ns)	50	/
τ (ns)	10	/

Note: *a*. The value of γ slightly drops from 1.4 to 1.3 when the temperature increases to 1800 K from room temperature. Here, we assume $\gamma = 1.3$ for the temperature range 300~1800 K, which leads to only a minor error.

where h is Planck's constant, c is the speed of light, k_B is the Boltzmann constant, and λ_s is the detection wavelength. Simulated temporal profiles of particle temperature $T_p(t)$ and LII signal $S(t)$ under various input conditions will be presented in the following sections.

5.2.2 Two-colour pyrometry and gas temperature

Note that equation (5.1) can be rewritten as

$$\frac{dT_p}{dt} = \frac{1}{mc_s} (\dot{Q}_a + \dot{Q}_c + \dot{Q}_e) \quad (5.10)$$

Integration of this equation gives

$$T_p(t) = T_0 + \frac{1}{mc_s} \left(\int \dot{Q}_a dt + \int \dot{Q}_c dt + \int \dot{Q}_e dt \right) \quad (5.11)$$

where T_0 is the initial particle temperature in equilibrium with the surrounding gas. Substitute equation (5.2) and (5.4) to the above equation,

$$T_p(t) = T_0 + \frac{6\pi E(m)}{\rho_s c_s \lambda_L} F \int q(t) dt + \frac{1}{mc_s} \left(\int \dot{Q}_c dt + \int \dot{Q}_e dt \right) \quad (5.12)$$

Note that the laser-induced temperature increase (second term on the right side) does not dependent on the particle size d_p . The particle temperature $T_p(t)$ can be measured by two-color pyrometry, where two sensors are used to detect the incandescence signal $S(\lambda)$ at different wavelengths λ_1 and λ_2 at time t

$$T_p(t) = \frac{hc}{k_B} \left(\frac{1}{\lambda_2} - \frac{1}{\lambda_1} \right) \left[\ln \left[\frac{S(\lambda_1, t) K_2(\lambda_2) \varepsilon(\lambda_2) \lambda_1^5}{S(\lambda_2, t) K_1(\lambda_1) \varepsilon(\lambda_1) \lambda_2^5} \right] \right]^{-1} \quad (5.13)$$

where the $K_{1,2}$ constants are dependent on the optical setup for each sensor, and $\varepsilon(\lambda)$ is the emissivity of the particle (which under the Rayleigh approximation is $\varepsilon = \pi d/\lambda$). If cameras were used as detector, the captured signal S_I will be a time integral of the LII signal, and thus the measured particle temperature T_m at time t is a mean value over the gating time,

$$T_m(t) = \frac{hc}{k_B} \left(\frac{1}{\lambda_2} - \frac{1}{\lambda_1} \right) \left[\ln \left[\frac{S_I(\lambda_1) K_2(\lambda_2) \varepsilon(\lambda_2) \lambda_1^5}{S_I(\lambda_2) K_1(\lambda_1) \varepsilon(\lambda_1) \lambda_2^5} \right] \right]^{-1} \quad (5.14)$$

where

$$S_I = \int S(\lambda, t) dt \quad (5.15)$$

If a submicron particle is heated by a pulsed laser at low fluences (sublimation process is negligible), the particle temperature rise will immediately reach its maximum value several nanoseconds after the laser pulse, while comparatively the particle cooling led by heat

conduction is a much slower process which may take several hundreds of nanoseconds. Hence, if an ICCD camera is shortly gated at the LII signal peak, the particle temperature decay caused by conduction and evaporation is trivial during the exposure time, which will be proven in section 5.3.1. During this short period of time after the laser pulse, the last two terms (conduction and sublimation) in equation (5.12) can be neglected. Note that this is not true for incipient soot. As has been proven in Snelling and co-worker's work [115], for incipient soot (20-40 nm), the cooling rate during the first 50 ns can be as high as -10 K/ns, because the particle size is too small. However, for our case where submicron particles are seeded (e.g. 100 nm), the cooling rate is much slower (-0.8 K/ns) than soot particles, which will be shown later on. Hence this assumption is reasonable for the proposed technique. Under this premise, the particle temperature and the LII signal can be approximated as being stabilized at the peak value and not a function of time, which gives

$$T_p = T_0 + \Delta T \quad (5.16)$$

and

$$S_I = \int S(\lambda, t) dt \approx S(\lambda) \delta t \quad (5.17)$$

ΔT is the laser-induced temperature increase, δt is the camera gating time. Thus, the original gas temperature T_0 can be obtained as:

$$T_0 = \frac{hc}{k_B} \left(\frac{1}{\lambda_2} - \frac{1}{\lambda_1} \right) \left[\ln \left[\frac{S(\lambda_1) \delta t K_2(\lambda_2) \varepsilon(\lambda_2) \lambda_1^5}{S(\lambda_2) \delta t K_1(\lambda_1) \varepsilon(\lambda_1) \lambda_2^5} \right] \right]^{-1} - \Delta T \quad (5.18)$$

δt cancels out in equation (5.18). For a case where we maintain the laser beam characteristics for experiments at gas temperature T_0 and T_{ref} , the second term cancels out, and we have for the temperature difference:

$$T_{\text{ref}} - T_0 = \frac{hc}{k_B} \left(\frac{1}{\lambda_2} - \frac{1}{\lambda_1} \right) \cdot \left[\ln \left[\frac{S_{\text{ref}}(\lambda_1) K_2(\lambda_2) \varepsilon(\lambda_2) \lambda_1^5}{S_{\text{ref}}(\lambda_2) K_1(\lambda_1) \varepsilon(\lambda_1) \lambda_2^5} \right] \right]^{-1} \quad (5.19)$$

$$- \frac{hc}{k_B} \left(\frac{1}{\lambda_2} - \frac{1}{\lambda_1} \right) \cdot \left[\ln \left[\frac{S(\lambda_1) K_2(\lambda_2) \varepsilon(\lambda_2) \lambda_1^5}{S(\lambda_2) K_1(\lambda_1) \varepsilon(\lambda_1) \lambda_2^5} \right] \right]^{-1}$$

This means that in principle, it should be possible to obtain the gas temperature T_0 from essentially a two-colour method on the heated particles, relatively to those under a reference local gas temperature (either *in-situ* or *ex-situ* calibration), so long as the total energy per unit mass of particle (and thus ΔT) can be controlled between the reference and the final situation.

5.2.3 Tracer particle selection

In the simulation, the particles used are assumed to be carbon black powders broken down into submicron aggregates by ultrasonic waves or by high shear force. Carbon black is a suitable surrogate in the present concept as they are formed of mature soot particles, used extensively in LII studies [116], and thus have well characterized light absorption characteristics. These particles are readily available commercially at industrial quantities and have well defined primary size distributions, typically in the range of 20-180 nm [116, 117]. Candidate tracer particles should at least satisfy the requirements that (a) the product of absorption efficiency and energy used should be sufficiently large to obtain adequate LII signal strength, (b) the primary particle size should fall in the Rayleigh regime to allow simple interpretation of the signal, and (c) the size distribution be well defined and sufficiently small to allow the signal obtained to be independent of diameter. Ideal tracers for this technique should also be inexpensive, non-reactive in flames, non-abrasive and able to sustain high temperatures. Potential tracers for this technique could therefore also be powders such as WC, SiC, MnO and other black metal oxides.

5.3 Numeric results and discussions

5.3.1 Particle temperature and integrated LII signal

In this section, simulated temporal profiles of particle temperature and integrated LII signal captured by an ICCD camera under various input conditions are presented, and the feasibility of the proposed technique is hereby demonstrated. Figure 5.1 shows the particle temperature and LII signal profiles at different laser fluences $F = 0.05, 0.07, \text{ and } 0.2 \text{ J/cm}^2$. To investigate influence of the sublimation and the heat conduction process on the history of particle temperature T_p and LII signal S_λ , the result given by non-heat-loss model is also plotted (blue line) for comparison, where the sublimation and heat conduction term were removed from the energy balance equation (5.1). For a low laser fluence (0.05 J/cm^2), the maximum particle temperature reached are the same for both heat-loss and non-heat-loss model, as the energy transferred via particle evaporation is trivial. After the peak, the particle temperature T_p is decaying slowly due to heat conduction to ambient gas, and difference between the real particle temperature (red line) and the adiabatic particle temperature T_a (blue line) increases gradually. It can be observed from the first row of figure 5.1, the particle cooling rate strongly depends on the particle size. For $F = 0.05 \text{ J/cm}^2$, the cooling rate for a 100 nm tracer is about -0.8 K/ns during the first 50 ns after the particle temperature peak, while for a 20 nm incipient soot (purple line), the cooling rate increases to -5.0 K/ns . This address the issue of selecting tracer particles in the right size range: If d_p is too large, the premise of Rayleigh approximation will be breached; however, if d_p is too small, the heat transfer via the conduction process cannot be neglected.

If a camera is used as the detector, the pixel intensity will be proportional to the time integral of LII signal over the shutter time, times its quantum efficiency at the detection wavelength. The time integral of the LII signal as a function of gating time is shown in the third row of figure 5.1. For a particle heated to a temperature below the sublimation point, the time integral of LII signal for the heat-loss case is very close to non-heat-loss case during $0\sim 50 \text{ ns}$ after the laser pulse. For $F = 0.05 \text{ J/cm}^2$, the difference in the integrated LII signal S_I between the two cases reaches 10 % at 43 ns (denoted by the dot line) after the

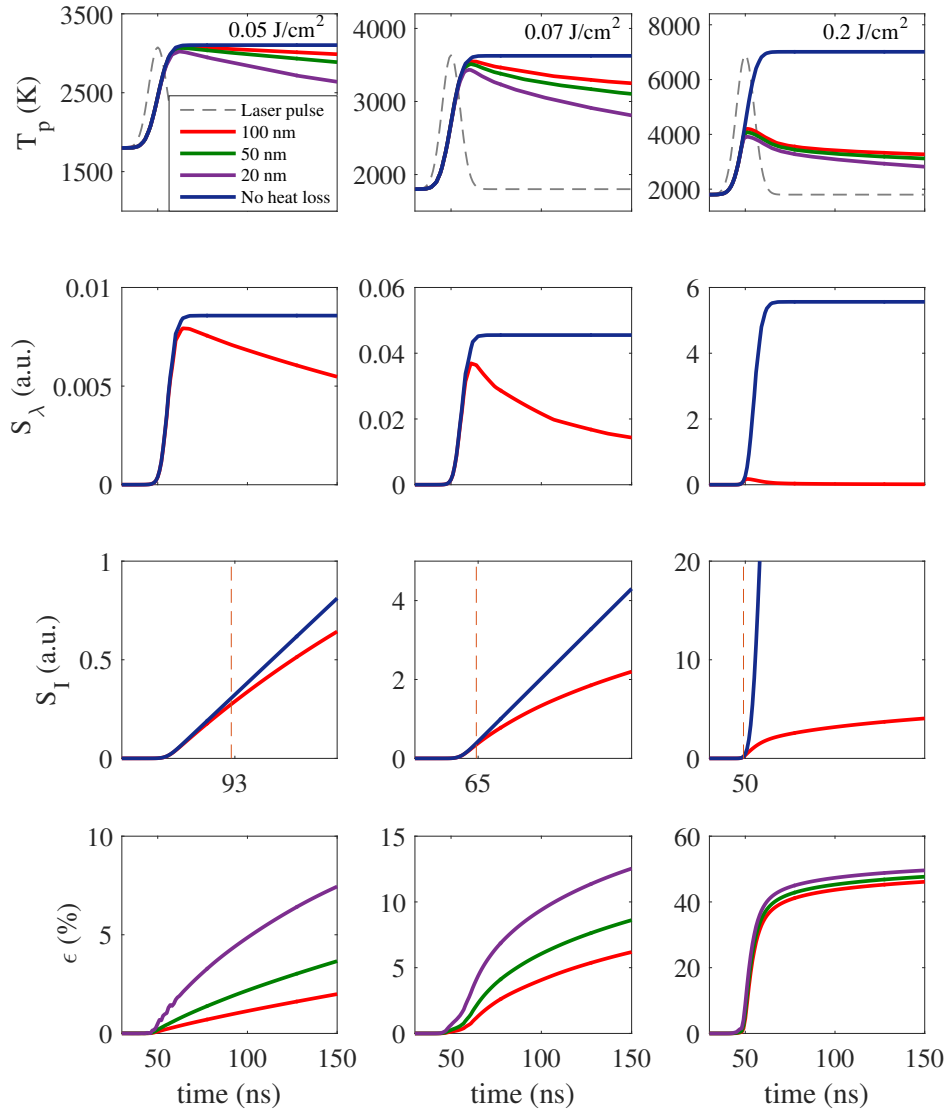


Fig. 5.1 (Row 1) Particle temperature profile T_p for different particle sizes and laser fluences. The blue line illustrates the result given by the non-heat-loss model; (Row 2) temporal profile of LII signal S_λ detected at 400 nm wavelength for $d_p = 100$ nm; (Row 3) Time integral of the LII signal S_I at 400 nm captured by a camera as a function of gating time, the dashed line denotes the time when the difference S_I given by the two models reaches 10 %; (Row 4) the relative error of measured particle temperature T_m by two cameras (400/780 nm) to the adiabatic particle temperature T_a , as a function of gating time δt , particle size d_p and laser fluences F . Other input conditions are: $T_0 = 1800$ K, $\lambda_L = 532$ nm.

peak of laser pulse. For a moderate fluence $F = 0.07 \text{ J/cm}^2$ where the sublimation starts to play a considerable role, this time duration drops to 15 ns. However, for $F = 0.2 \text{ J/cm}^2$, the sublimation process has become substantial and dominated the energy balance, the particle temperature reaches the sublimation point and will not further increase, showing a huge difference ($\sim 3000 \text{ K}$) with the adiabatic particle temperature calculated by the non-heat-loss model.

We define ε as the relative error between the adiabatic particle temperature T_a and the measured particle temperature T_p by two cameras,

$$\varepsilon = \frac{T_a - T_m}{T_a} \quad (5.20)$$

The fourth row of figure 5.1 shows ε as a function of particle size d_p , laser fluence F and camera gating time δt . For the case $F = 0.05 \text{ J/cm}^2$ and $d_p = 100 \text{ nm}$, ε remains below 2.5 % even for an exposure time longer than 100 ns. However, as we noted above, ε will increase if smaller particles are used due to higher cooling rate. The relative error also increases with higher laser fluence. For $F = 0.2 \text{ J/cm}^2$, ε can be as high as 40%.

It can be concluded from the above analysis that, for a low-fluence condition, the assumption we made in equation (5.16) is reasonable that the conduction and sublimation term can be neglected during a short period of time after the laser pulse, and that the particle temperature and LII signal is not a function of time during this time period, whereas for high fluences this assumption can no longer stand.

Since we are proposing a 2D temperature mapping technique, the detectors used are limited to cameras. Choosing an appropriate gating time δt is very important for achieving this technique successfully: (1) according to the analysis above, the gating time should be short enough to ensure that the measured particle temperature by 2-color method is very close to the theoretical value calculated by the non-heat-loss model, (2) it should be short to avoid the noise from flame luminosity, (3) the gating time should be sufficiently long so that the camera can collect adequate LII signal, and (4) it should fall in the range that could be

achieved by an intensifier or a mechanical shutter. In the present study, we assume that two ICCD cameras are used to perform 2C LII thermography, and the gating time of which is denoted as δt starting right after the peak of laser pulse. Unlike conventional 2C-LII studies, all results and analysis below are based on the time integral of the LII signal over the shutter time (δt), rather than on the LII signal peak.

5.3.2 Sensitivity and dynamic range

Figure 5.2 shows the sensitivity of LII signal captured by a camera to gas temperature T_0 at a certain level of laser fluence. The LII signal starts to lose sensitivity to the local gas temperature at high fluences, because the particle peak temperature after heating is very close to the sublimation point. This represents a compromise between sensitivity and dynamic range for the present technique. Assume the dynamic range of CCD sensors reads from 1 to 10 (saturated), for $F = 0.1 \text{ J/cm}^2$, the detectable temperature range is 400~1800 K, but the sensitivity at 1300~1800 K is very low. However, if $F = 0.07 \text{ J/cm}^2$, the signal peak gains better sensitivity to the gas temperature T_0 , but the camera can only capture the incandescence signal from regions of the flame where $T_0 > 1000 \text{ K}$. At higher fluences ($F = 0.2, 0.5 \text{ J/cm}^2$), particles in all regions of the flame have reached the sublimation temperature and cannot further increase. In such case, information of the original temperature field has been entirely lost.

On the other hand, the intensity of incandescence signal is approximately proportional to T_p^4 , hence a sufficiently high laser fluence should be used to guarantee a good signal to noise ratio, especially for ratio-based techniques. It can be observed from the signal profiles in figure 5.1 that the captured signal increases to about 4 times, while the fluence only increases 1.4 times (0.07/0.05). Seeking an appropriate range of laser fluence that can avoid severe sublimation of particles but at the same time achieve adequate signal to noise ratio for an ICCD camera has been proven to be possible based on previous studies on 2C-LII [118], in which high fluences were avoided in order to preserve the original size of primary particles.

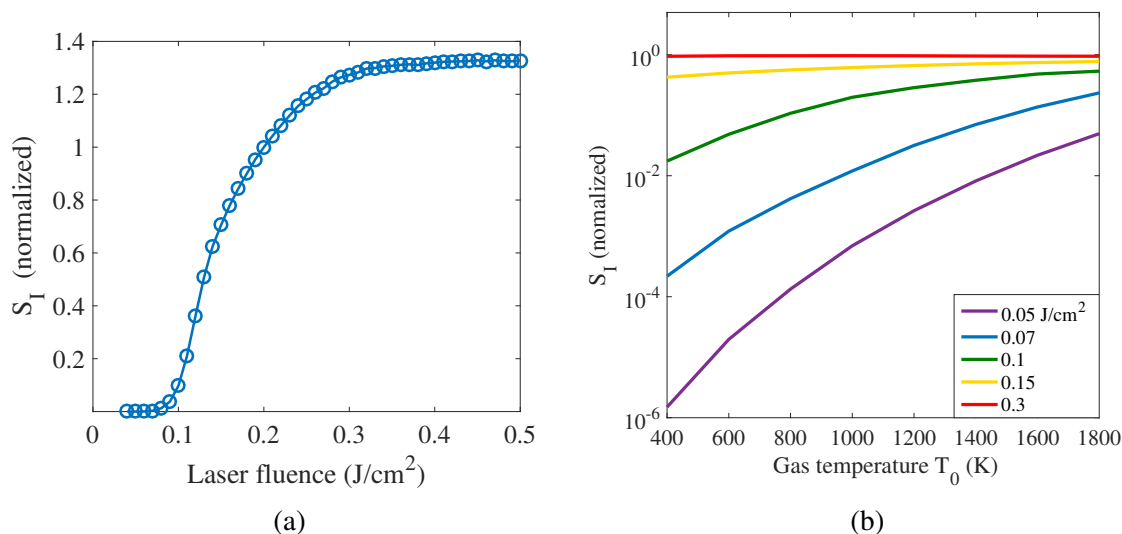


Fig. 5.2 Numerical results of (a) fluence dependence of LII signal magnitude for $T_0 = 1800$ K, normalized at $F = 0.2$ J/cm^2 (b) time integral of LII signal S_I as a function of T_0 at 5 levels of laser fluence. Other input conditions: $d_p(t=0) = 100$ nm, $\lambda_L = 532$ nm, $\lambda_s = 400$ nm, $\delta t = 20$ ns

5.3.3 Detection wavelengths and 2-color ratio

To select an appropriate combination of the detection wavelengths λ_{s1} and λ_{s2} , several factors need to be considered: (a) the signal ratio should be sensitive to particle temperature, (b) bandwidth should be sufficiently broad so that the signal can be detected by the CCD sensors and (c) the wavelengths should avoid the fluorescence emission band from C_2 , C_3 and PAH. At low fluences, most prominent spectral interference arises from Swan-band emission from excited C_2 at 468, 516, 550, and 580~620 nm [119, 120], these spectral bands should be carefully avoided when selecting the detection wavelengths. Liu *et al* [121] investigated the detection wavelength selection numerically, and suggested an optimal combination that $\lambda_{s1} = 400$ nm and $\lambda_{s2} = 780$ nm, the ratio between which will yield the best temperature sensitivity. However, they did not consider the bandwidth of the chosen filters and their effects on the sensitivity of the signal ratio to temperature. Generally, the bandwidth of filters in near UV region should be broader as the quantum efficiency of CCD sensors are relatively low for this wavelength range. Meanwhile, the filter in visible and near IR range should be narrow to reduce the interference from strong flame luminosity, and to protect the sensor from being overexposed.

Figure 5.3 shows the numerical result of LII signal S_I at various detection wavelengths λ_s ranging from 400 nm to 700 nm, as a function of ambient temperature T_0 . Particle size $d_p = 100$ nm, excitation wavelength $\lambda_L = 532$ nm, laser fluence $F = 0.05$ J/cm². The intensities of LII signal peak detected from various spectral lines are all very sensitive to ambient temperatures. However, the proposed technique is based on signal ratio, rather than signal intensity, because the latter is also affected by the particle size d_p and seeding density f_v , which are difficult to be controlled experimentally. The LII signal intensity spans over 2 orders of magnitude for the ambient temperature range from 400 K to 1800 K under the above conditions. Therefore, the LII signal emitted from low temperature regions in a flame may hardly be captured by detectors. Interestingly this is just opposite to the behavior of LIP thermometry which only works in the low-median temperature zone in a flame [39]. In order to measure the temperature in these regions, higher fluences should be applied to heat the particles to a temperature at which they could emit detectable LII signals. However, exposed to the same laser fluence, the particles in high temperature regions of a flame will be overheated and subjected to severe sublimation, and will lose the sensitivity to the temperature field as illustrated in figure 5.2. Experimentally, the 2C-LII thermography is not suitable for low temperature measurements because (a) output energy of a PIV laser is limited, especially for a high speed PIV laser, (b) the ambient temperature is indirectly inferred by measuring the particle peak temperature, hence any error from the latter would be amplified and passed to the former. For example, if a particle at 300 K ambient temperature was heated to 3000 K, 1% error in particle peak temperature measurements will cause 10% relative error for the measured ambient temperature. This is in contrast with phosphor-based thermography, which has very low yield of phosphorescence at high temperatures and thus is preferred for low temperature applications. Hence the LII-based and LIP-based thermographic PIV can be a supplement to each other.

Figure 5.4 plots the signal ratio to ambient temperatures ranging from 400~1800 K for four pairs of detection wavelengths, some of which were reported by previous studies [121, 118, 122]. The bandwidths of selected BP filters are also taken into consideration, and their effects on the temperature sensitivity are presented by comparing with the signal

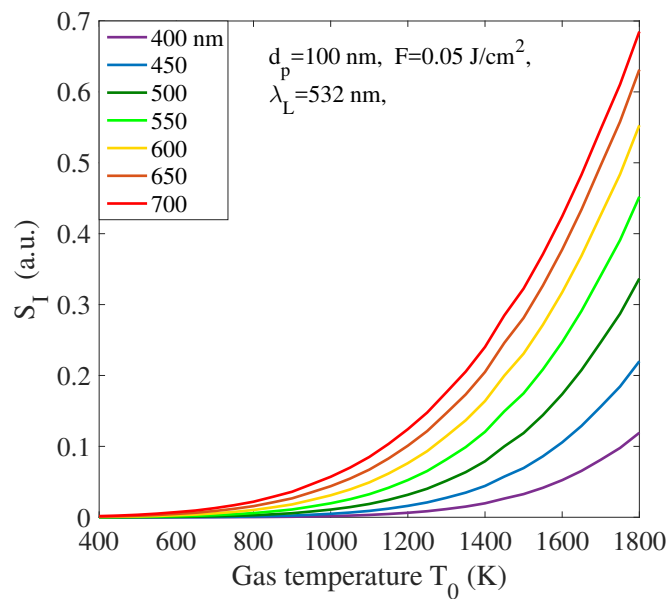
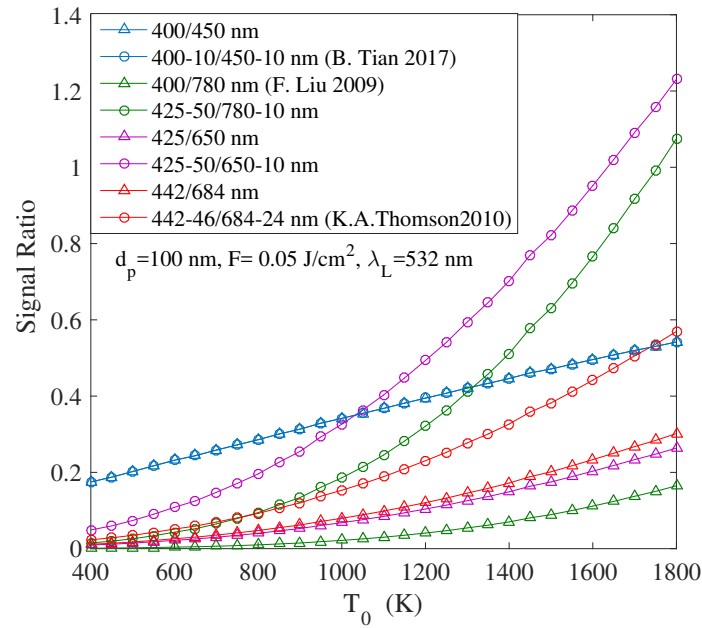
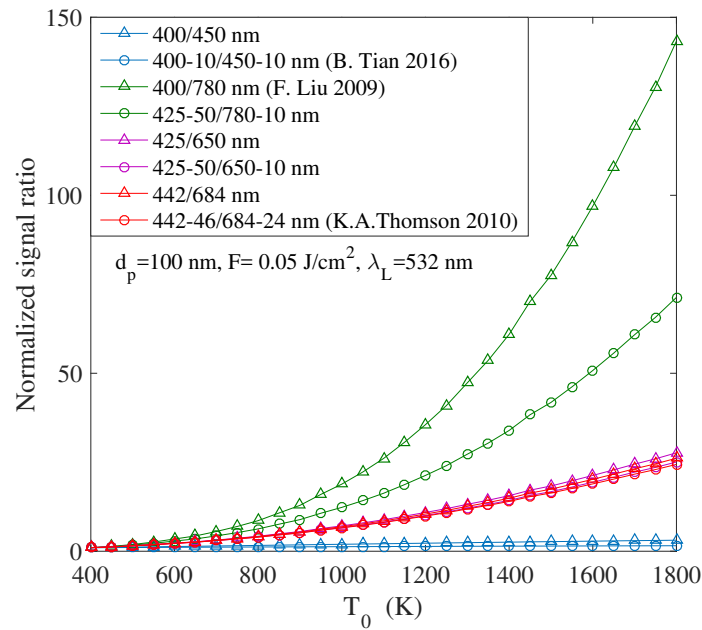


Fig. 5.3 Time integral of LII signal S_I at various detection wavelength ranging from 400 nm to 700 nm, as a function of ambient temperature T_0 . Input conditions: $d_p = 100$ nm, $F = 0.05$ J/cm², $\lambda_L = 532$ nm. Gating time $\delta t = 20$ ns.

ratio curves calculated from centre spectral lines of the same filters. According to figure 5.4(a), the ratio of signal intensity at two spectral lines is far below unity unless the two are close to each other (400/450 nm), because within the temperature range of interest, the LII signal at the short-wavelength line is weak and overwhelmed by the other spectral line. Given that most cameras have low quantum efficiency in near UV range, the blue channel may not be able to capture any signal at all. One way to solve this problem is to use a wide bandpass filter for the blue channel so that more LII signals can be collected. Although this would slightly reduce the sensitivity of the measured signal ratio to temperature, as illustrated by the normalised curves shown in figure 5.4(b), the signal strength collected by the blue channel has been significantly improved and becomes comparable with the other channel for $T_0 > 1400$ K. It can also be observed from figure 5.4(b) that the two selected wavelengths should be far from each other on spectrum to guarantee a better temperature sensitivity. This was confirmed by the results in [122] and [118]: the former (400/450 nm) can hardly resolve the soot temperature while the latter shows a clear map of soot peak temperature which very much resembles a typical temperature pattern of a diffusion flame.



(a)



(b)

Fig. 5.4 (a) Numerical results of signal ratio (Gating time $\delta t = 20$ ns) as a function of ambient temperature for four combination of detection wavelengths, (b) the same curves in (a) are normalized to unity at $T_0 = 400$ K. Cases for both spectral lines (triangle) and bandpass filters (circle) were simulated.

5.4 Summary

This chapter introduces the concept of a LII-based thermographic PIV technique. For submicron particles heated by a top-hat pulsed laser sheet, the temperature increase due to absorption is the same for all individual particles regardless of their size (known as Rayleigh approximation), under the premise that they have not yet reached the sublimation point. Hence the local gas temperature can be inferred from particle peak temperature which can be measured by 2C pyrometry. Meanwhile, the Mie scattering or LII signal itself emitted from the same particles can be recorded by a PIV camera to determine the velocity field. Thus simultaneous temperature and velocity measurements can be achieved. A simplified LII model was built based on previous studies to demonstrate the feasibility of the proposed technique. Several conclusions can be drawn from the numerical investigation:

- (1) The laser energy applied for this technique should be in a moderate range that avoids severe particle sublimation but at the same time can guarantee a robust LII signal strength. This technique is not suitable for low temperature applications as the relative error in measurements of particle peak temperature would be amplified and passed to the measured local gas temperature. Hence it is proposed as a supplement of thermographic PIV based on phosphors.
- (2) Detection wavelengths should be carefully selected to avoid the interference from other laser-induced signals. Numerical results suggest that a wide bandpass filter in near UV range combining with a narrow filter in near IR region is the best option in terms of temperature sensitivity and signal detectability.

The proposed technique has a potential for improving our understanding on fundamental combustion mechanisms by revealing the interaction between turbulence and reaction in flames, using inexpensive tracers. Hence it could be of highly interest for researchers who are working on combustion. Future work will be focused on realizing this technique experimentally, investigating its limits, and seeking ideal tracers for in-chamber applications.

5.5 Further considerations

5.5.1 Tungsten carbide

One potential candidate tracer for the proposed LII-TPIV could be Tungsten carbide particles. The melting point of WC is around 2800 °C, and the boiling point is over 6000 °C, which means that WC particles can sustain the flame temperature in most cases. The laser fluence selected for the proposed technique should be moderate to guarantee a robust LII signal, but at same time to avoid severe sublimation/boiling of the tracer particles in case temperature information is lost. Since WC has a extremely high boiling point, a large window can be expected for the selection of appropriate laser fluence. In the following chapter, PIV measurements based on LII signal from WC particles are demonstrated.

5.5.2 Particle size for velocity and temperature measurement

The LII thermography works only when the particle size falls in the Rayleigh regime. In this size range, the scattered light by individual primary particle may be too weak to be captured by a PIV camera. This may be a potential problem for simultaneous temperature and velocity measurement. Based on our preliminary experimental results, however, the WC particles formed small aggregates in gaseous flows, which generates clear particle image patterns on the PIV image. A clear particle image pattern is ideal for cross-correlation and vector detection. On the temperature measurement, formation of small WC aggregates due to particle inter-forces may not affect the temperature accuracy: the light absorption by small aggregates is usually described by the Rayleigh–Debye–Gans approximation (RDG), which assumes absorption and LII emission is mainly decided by primary particles, rather than the geometry of the aggregate itself [123]. However, if a large aggregate consisting of over hundreds of primary particles is formed, the RDG approximation no longer stands. The heat conduction in such scenario will also be affected: the large geometry suppresses the heat transfer from inner primary particles to ambient gas, thus leads to a long temperature relaxation time. Therefore, controlling the aggregate size is a key issue to implement the proposed LII-TPIV technique.

Chapter 6

LII-based particle image velocimetry for two phase flow velocity measurement

6.1 Introduction

Two-phase flows are of wide interest for a variety of industrial processes, and especially for combustion conversion devices, such as liquid-fueled engines, gas turbines and solid fuel conversion. The interaction between fuel droplets/particulates and gaseous flows is of interest to capture the mass and heat transfer between particle and surrounding gas. Particle image velocimetry (PIV) is often used to collect information on the velocity field for each phase to validate models of droplet/particulate flow and reaction. However, such measurements are challenging for a number of reasons; in particular, droplet and particle sizes relevant to combustion applications range from tens to hundreds of micrometers. This has two consequences: (a) larger particles do not follow the gas flow, particularly under conditions where droplets are injected with high momentum relatively to the surrounding gas; (b) seeding micron-sized tracers into the two-phase flow cannot solve the problem, because the Mie-scatter PIV measurements produces blooming bright spots for the larger particles on the images over the much dimmer smaller particles, biasing and limiting the measurements under the limited dynamic range of typical cameras. There is a vast literature on developing advanced PIV techniques for multi-phase flow in non-reacting cases, but to the authors'

knowledge, none of these studies were aimed at or conducted in *reacting* cases. Hence, the purpose of this study is to develop a new PIV technique that can be applied to measure both non-reacting and reacting two phase flows. A summary and detailed classification of previous methods can be found in the work by Khalitov and Longmire [124].

Methods for discriminating velocities in two different phases fall into two categories: *color-based* methods and *Mie-scatter* methods. These are described below in sequence.

Color-based methods typically use the fluorescence signal from micron-sized tracers doped with laser dye to separate Mie scattering from liquid droplets/non-fluorescent particles. The gas-phase velocity is derived from the former, whilst the velocity of the disperse form is extracted from the latter. Examples of this approach can be found in [125, 126]. The technique suffers from the disadvantages that (a) fluorescent particles are relatively expensive or difficult to prepare in the laboratory, (b) the dyes used to dope the particles/droplets are usually highly toxic, requiring special safety procedures, (c) high laser energy is required for sufficient signal yield, and, most relevant to combustion studies, (d) the fluorescence signal disappears at high temperatures due to thermal quenching and decomposition of dyes in a flame. One of the most recent reports on fluorescence-based PIV by Petrosky and co-workers [127] showed that KR620-doped particles could be a good surrogate for conventional fluorescence tracers due to their low toxicity. However, these particles do not overcome the problem of low signal yield.

Previous work [77] demonstrated PIV measurements with phosphorescence signal using ZnO particles ($< 2 \mu\text{m}$) excited by a double-pulsed UV laser at 355 nm, with an emission spectrum spanning from 350 to 450 nm. Such a technique can be used for velocity measurements in two-phase flows under non-reacting conditions, using a suitable pulsed laser sheet in the UV range. Unlike specially made fluorescent particles, ZnO particles are inexpensive, non-toxic and the resulting light emission is sufficiently strong at the low temperatures, but its signal strength drops quickly as temperature increases, and can no longer be detected by unintensified CCD cameras beyond 500 K.

An alternative approach to fluorescence and phosphorescence is based on the area dependence in Mie scattering: signal from both large droplets or solid particles and intentionally

seeded micron-sized tracers are recorded by a single camera. Large particles are segregated from the smaller particles by preprocessing the PIV image before cross-correlations are made. Sophisticated algorithms have been developed based on signal intensity differences [128], spot size [129], spot shape [130], or their combinations [124]. The cost of the Mie-based method is relatively low on the experimental side, but the algorithms used are significantly more computationally intensive than in usual PIV processing. Further, there is no universal algorithm for all two-phase flows, and image processing methods and filter parameters need to be selected based on the particular conditions of PIV images from each test. Factors such as the seeding density, contrast between large and small particles, and the background signals all have strong effects on the selection of filters and the sequence of operations. Experimentally, the limited camera dynamic range creates a problem: since Mie scattering intensity is proportional to the square of particle size, apertures must be chosen so as to enable visualisation of the smallest particles, yet the light scattered from particles of hundreds of micrometers size may exceed the exposure limit and permanently damage the CCD sensors. Finally, the main limitation of the Mie-based method is the requirement the original liquid or solids particle concentration be very sparse. Due to diffraction, micron-size particle images appear to be much larger than their physical size. Therefore, even for a moderate droplet/solid number concentrations in a gaseous flow, PIV images can be dominated by large bright spots, while the small and dim images of seeded tracers cannot be separated from those large spots. This strongly limits the application of Mie-based methods in combustion studies, because the spacing between fuel droplet/particles is designed to be sufficiently small to allow continuous flame propagation in the mixture, especially in the case of less volatile fuels [131]. On the image processing side, difficulties include (a) decreases in droplet and particle size due to evaporation or reaction, (b) variable spatial concentration over sharp temperature gradients, and (c) image distortion near inhomogeneous gas refractive indices such as flame regions. To date there has not been a general algorithm that can deal with all of these issues.

The absence of a velocity imaging technique for two-phase flames has been reflected in recent combustion studies. In a recent review on work on spray combustion modeling [132], it was concluded that the slip motion of fuel droplets has an effect on the heat and mass

transfer between the droplets and the gaseous flow. Most current studies on sprays rely on Laser Doppler Anemometry (LDA) to measure droplet velocities based on their size range by applying different masks, such as [133, 134]. However, LDA cannot resolve velocities spatially, and the velocity for different size ranges cannot be measured simultaneously. The difficulty in obtaining gas-phase velocity was also highlighted in a study on the combustion of aluminum suspensions [135]. Julien and co-workers attempted to measure the burning velocity of aluminum particles ($SMD=5.6 \mu\text{m}$) on a counterflow burner with PIV, but they found that the slip motion of these particles was considerable. Since no technique was available to determine the fluid velocity directly from this particulate flame, they estimated the effective Stokes time by conducting a calibration in a cold impinging-jet, and then corrected the lag in particle motion.

To implement velocity measurements in two-phase *reacting* flows, we propose using the laser-induced incandescence (LII) image pairs from submicron black tracers in PIV, rather than images of Mie scattering, fluorescence or phosphorescence. LII imaging traditionally works by heating soot particles to sufficiently high temperatures by a high-energy laser sheet so as to reach a fixed sublimation temperature, allowing the incandescence signal to be dependent primarily on the concentration of particles. A comprehensive review on the theory of LII and its application can be found in [98]. The LII technique has also been used to detect carbon black particles in dispersed form [136]. In addition, there have been several recent attempts to use LII technique as a diagnostic method for the flame synthesis of nano-particles such as silicon [137] and titania [138]. In this study, submicron tungsten carbide (WC) particles were seeded into a droplet-laden flow and illuminated using a 532 nm PIV laser at a sufficiently high pulse energy. The WC submicron tracer particles were heated to several thousands of degrees to emit a strong incandescence signal, whereas the temperature increase for large droplets is negligible. The radiative incandescence due to high temperature black body radiation can be collected away from the exciting wavelength (in this case, 400-450 nm), thus allowing a separation of the signal from the submicron particles relatively to the liquid/solid phase.

This study introduces the fundamentals of LII-based PIV, demonstrating the technique for non-reacting two-phase flows, and shows the possibility of application to reacting flows. The experimental setup for LII-PIV is described in section 6.2. Section 6.3 demonstrates LII-based PIV in a single-phase air jet, and compares results with those obtained by Mie-based PIV with $1\ \mu\text{m}$ alumina particles. Velocity measurements in a non-reacting droplet-laden (ethanol $\text{SMD}=38.2\ \mu\text{m}$) flow and a methane/air flat flame are presented in section 6.4 and 6.5, respectively.

6.2 Experimental

6.2.1 Optical system

A double-pulsed Litron Nano-PIV laser at 532 nm was used to generate a diverging light sheet with a thickness of approximately 0.3 mm, by expanding the beam through a focal length $\text{FL} = -150\ \text{mm}$ concave cylindrical lens followed a $\text{FL} = 500\ \text{mm}$ convex lens. The height of the laser sheet above the test section is about 6 cm. The laser energy used was 74.2 mJ for the first pulse, and 87.5 mJ for the second pulse, for an average laser fluence of 0.42 and $0.49\ \text{J}/\text{cm}^2$ respectively. A 2048×2048 pixel CCD camera (Image Pro X 4M, LaVision) was operated in double frame mode at 5 Hz to collect both the LII and Mie scattered signal. The exposure time for the first frame was fixed at $5\ \mu\text{s}$, and the exposure is fixed by the camera CCD technology to a minimum of $\sim 150\ \text{ms}$ for the second frame. A Nikkor 60 mm micro lens was used to focus the image. The pixel resolution was $31.9\ \mu\text{m}$ as calibrated by a target plate. An averaged background signal was recorded and subtracted from the 400 images collected. Due to a limited number of cameras available at the time of the test, the LII and Mie scattering signal were captured non-simultaneously by the same camera, but with different filters: (a) for the LII signal, a $425 \pm 25\ \text{nm}$ bandpass filter was installed in front of the lens and the aperture was opened wide ($f/2.8\text{D}$) to guarantee a sufficiently strong LII signal; (b) for Mie scattering from micron-size particles, the combination of a $\text{ND}=0.6$ neutral density filter and $532 \pm 1.5\ \text{nm}$ narrow bandpass filter was applied, and the lens aperture was set to $f/5.6\text{D}$; and (c) For the very strong scattering from large droplets, a

ND=2 filter was used instead, which reduces the signal to 1% of its original value, and the aperture was reduced to $f/22D$ to avoid any damage to the CCD.

6.2.2 Particles

The tracer particle type for LII-PIV experiments in flames were chosen according to the following considerations: (a) the product of laser light absorption efficiency and energy used should be sufficiently large to obtain adequate LII signal strength; (b) the material should be non-reactive and able to withstand high temperatures; (c) the particle should be small enough to follow the sharp velocity gradients in a turbulent flame; and (d) the particles should be sufficiently large to produce a recognizable individual particle image for a successful cross-correlation. Ideal tracers for this technique should also be non-abrasive (for internal flow studies) and inexpensive (for large flow rate systems).

After considering a number of tracers, such as carbon black, graphite, manganese oxide and silicon carbide, the material selected was tungsten carbide (WC) with particles supplied by A.L.M.T. Corp. (WC02N). The Sauter Mean Diameter (SMD) of the WC particles is $0.2 \mu\text{m}$, with a standard log mean deviation of $0.16 \mu\text{m}$. The Stokes number of these particles is far below unity at the velocities considered, hence their slip velocity should be negligible, as also demonstrated experimentally in section 6.3. Tungsten carbide appears as black in powder form, which suggests that WC particles have a high absorption efficiency to visible and infrared light source. The melting point of WC is around $2800 \text{ }^\circ\text{C}$, so particles remain stable at most flame temperatures. The WC powder is inexpensive ($< \$130/\text{kg}$) and non-toxic, so it can be used in large quantities without safety concerns under well ventilation. These characteristics make WC particles an ideal candidate for the proposed LII-PIV technique. LII-PIV using carbon black and graphite was also attempted, but these were found to be more difficult to handle and disperse, and the results are not shown here. For comparison, a common PIV tracer, $1.0 \mu\text{m}$ alumina (0CON-007, Logitech Ltd.) was also applied to perform PIV measurements described in the following experimental sections.

6.2.3 Seeding density

Controlled seeding density is important for LII-PIV in a flame, as the flames may be sensitive to particle loading. Firstly, the local gas temperature may increase as the heat absorbed by particles from the light source is eventually passed to ambient gas via convection and radiation. This was reported for 2C-LII on a sooting ethylene diffusion flame [139], where the soot volume fraction reported was several orders of magnitude higher than the normal seeding level for PIV measurements. In the present study, the particle concentration is estimated as 1.6×10^{11} particles/m³ based on the Mie scattering images (~ 50 particles per 32×32 interrogation window). With this seeding rate, the heating effect on local gas is estimated as follows.

Consider a single particle of diameter d heated by uniform laser light of wavelength λ , with a fluence F in the Rayleigh regime. The total energy absorbed is given by:

$$q_p = \frac{4\pi d E(m)}{\lambda} F \frac{\pi d^2}{4} \quad (6.1)$$

where $E(m)$ is the refractive-index function for absorption of the tracer particle. In the absence of data for WC particles, the value $E(m) = 0.24$ for soot particles is assumed [140]. For a wavelength of 532 nm, a particle diameter of 200 nm and a mean fluence of 0.45 J/cm², the total energy addition is 1.6×10^{-11} J/particle. For an estimated concentration of 1.6×10^{11} particles/m³, the total energy eventually transferred to the gas corresponds to $Q = 2.6$ J/m³. The expected temperature rise for air properties of $\rho = 1.2$ kg/m³ and $c_p = 1000$ J/kg K is therefore $\Delta T = \frac{Q}{\rho c_p} \approx \mathcal{O}(10^{-3})$ K, which is clearly negligible.

A second consideration might be that the presence of particles with high radiative emissivity may increase the radiative heat loss from the flame: if the seeding density is too high, the temperature distribution in the flame may be changed; if too low, the particle images become too sparse to provide a velocity field with a decent spatial resolution. Here an approximate calculation on the radiative heat loss is presented as follows. For a single spherical WC particle in a flame at 2100 K, the radiative heat loss rate is estimated by the Stefan-Boltzmann law [141], and neglecting absorption of the radiation by surrounding

particles, we have:

$$\dot{q}_r = \pi d^2 \varepsilon \sigma (T_f^4 - T_a^4) = 1.4 \times 10^{-7} \text{ W} \quad (6.2)$$

where ε is the emissivity of tungsten carbide particles, taken as unity. $\sigma = 5.67 \times 10^{-8} \text{ W}/(\text{m}^2 \cdot \text{K}^4)$ is the Stefan-Boltzmann constant and T_f is the flame temperature. Considering a 20 lpm total gas flow rate with a seeding rate of $1.6 \times 10^{11} \text{ WC particles}/\text{m}^3$, total radiative power produced by the glowing particles is

$$\dot{Q}_r = \dot{q}_r N \approx 7 \text{ W} \quad (6.3)$$

For a gas mixture consisting of air/methane at stoichiometry, the heat release rate from combustion of the fuel is approximately

$$\dot{Q}_{CH_4} = 1.2 \text{ kW} \quad (6.4)$$

This suggests that for usual PIV seeding levels (50 particles per interrogation window for the present configuration), the radiative heat loss by WC particles is negligible compared with the heat produced by the reaction.

6.2.4 Effects of the LII decay time on the maximum measurable velocity

In the present experiment the tested flow speeds are lower than 15 m/s. Therefore, during the LII decay time (1-2 μs , based on a preliminary test) the particle barely moves compared with the displacement during the pulse interval, so that particle images do not appear as streaks on any frames. Considering a decay time of 2 μs , 31.9 μm pixel resolution and a particle image size of 2-4 pixels, the maximum velocity allowed is estimated as $\sim 30 \text{ m/s}$ (during the decay time the particle moves less than 2 pixels whilst the signal strength decays exponentially). Beyond this velocity range, particle streaks may appear. However, in principle it should be possible to perform cross-correlations over particle streaks which start from a bright spot to a dark end, thus providing extra information for correlation peak detection. For supersonic

applications, the LII signal would leave a long trajectory (> 20 pixels for current setup) on the images. Direct correlation on these trajectories may not be possible with the proposed technique. In this scenario, further image processing may be required to capture the starting location of particles, which is beyond the scope of this chapter.

6.3 LII-PIV demonstration on an air jet

6.3.1 Operating conditions

The proposed technique was first tested on a seeded air jet of diameter 11.7 mm at a flow rate of 50 slpm, corresponding to a bulk velocity around 8.5 m/s at 298 K and a Reynolds number $Re=6600$. The air flow rate was metered by a 250 slpm Alicat Mass Flow Controller (MFC), with 1% full scale precision. The time interval between two laser pulses was set to $\delta t= 40 \mu s$. Tungsten carbide particles ($0.2 \mu m$) and fine alumina particles ($1 \mu m$) were seeded to the air jet separately by a seeder (Texas Airsonics AJ-1), and measurements were made based on the Mie and LII signal respectively. Before loading new tracers, the seeder, pipe and jet were flushed by 200 slpm air flow rate for 20 minutes to ensure that there were no residual particles in the flow system. Fig. 6.1 shows the PIV images recorded at the green (532 nm, *top row*) and blue (425 nm, *bottom row*) channels for the two types of particles. The absorption cross-section of white alumina particles is much smaller than that of tungsten carbide, hence no LII signal can be detected from alumina tracers, as shown in Fig. 6.1 (*bottom row*). Note that the laser fluence used in this study is too low to heat particles larger than several micrometers to LII temperatures, even if they have large absorption efficiency (black), as also determined in a study of coal particles [142]. Hence this technique can potentially be applied to measure two phase flows laden with large coal or metal particles, as the latter will not produce detectable LII signals.

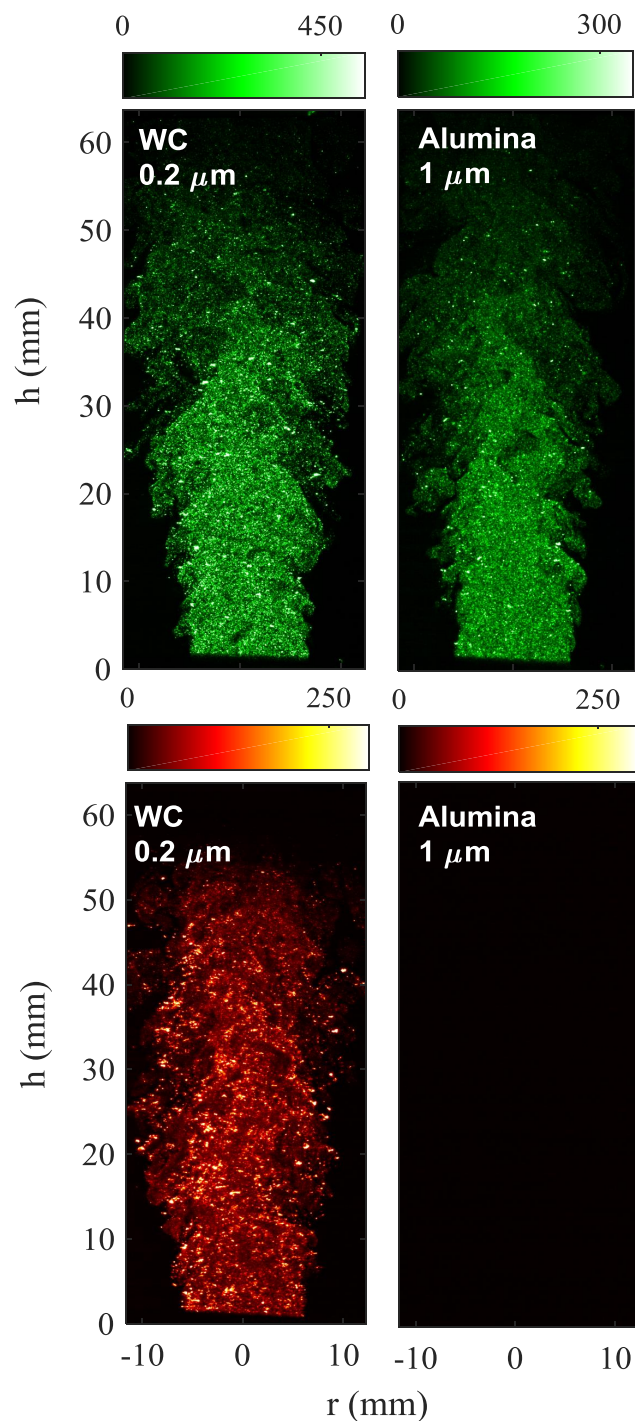


Fig. 6.1 First frame shots of a PIV image pair based on Mie scattering (*top row*), and LII signal (*bottom row*) in an air jet. Tracers are $0.2 \mu\text{m}$ WC and $1 \mu\text{m}$ alumina respectively (*columns*). The colorbars show the actual intensity counts recorded by the camera, which saturates at 9900 counts and has a dark noise around 5 counts. Note that the *hot* colormap is used to represent the incandescence signal, but it was actually collected from a blue channel ($425 \pm 25 \text{ nm}$).

6.3.2 Raw images and data processing

Figures 6.2(a) and (b) show the zoomed-in view of a Mie-scatter and a LII image extracted from the first frame, both based on the WC tracer. As mentioned earlier, for the velocity in this case, the particle displacement during this signal decay time is less than 1 pixel, which cannot be resolved by the camera. Hence particle images do **not** appear as streaks on any frames.

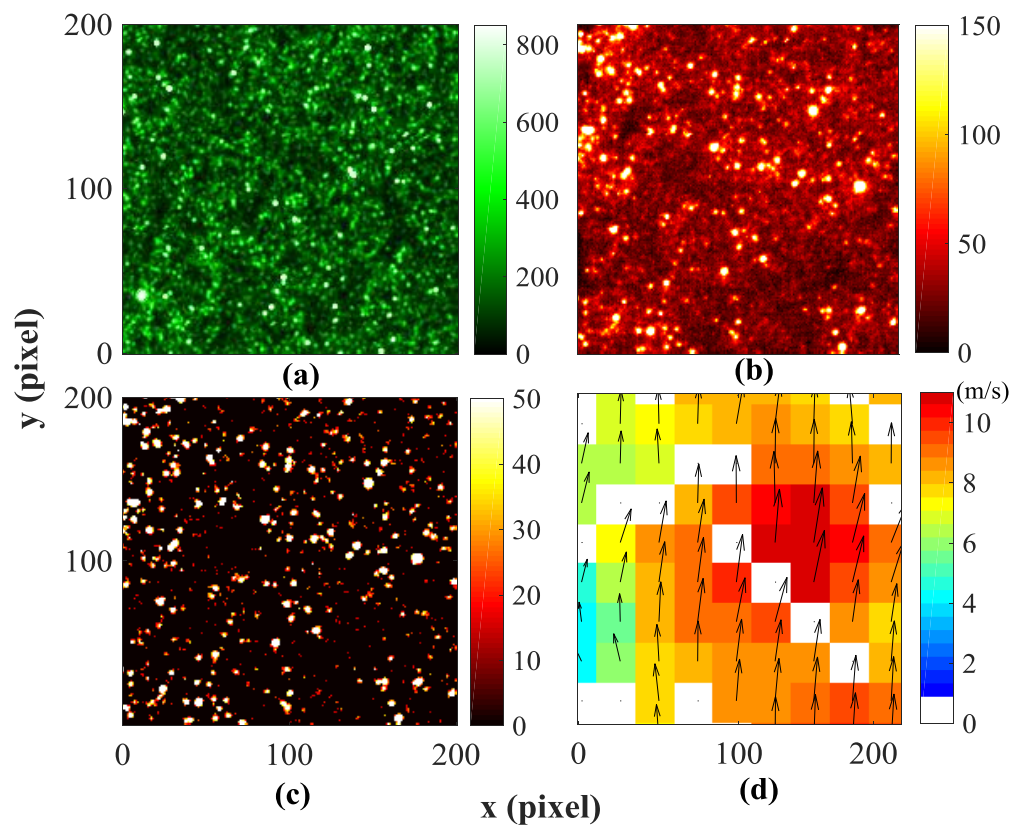


Fig. 6.2 (a) Mie-scatter image of WC particles; (b) LII image of WC particles, both extracted from the first frame; (c) preprocessed LII image; (d) velocity field obtained at the same position based on the LII image pair (second frame not shown here). To present the robustness of the proposed technique, the vector field shown in (d) has not been post-processed by any interpolation or smoothing, and the interrogation region for removed vectors are shown in white. The area of the shown region is 200×200 pixel (6.4×6.4 mm²)

The Mie-scatter images in Fig. 6.2(a) shows clear particle images on a clean background, whereas the LII image 6.2(b) shows blurred particle images on a background of ~ 30 counts.

The mean intensity of LII spots is about 200 counts (maximum 800 counts) for a noise level of 5 counts, whilst the mean intensity of Mie-scatter particle image is around 300 counts. According to the LII theory, the incandescence signal strength is approximately proportional to T_p^4 , and the particle temperature T_p depends on the local laser fluence F . The laser sheet used in this experiment had a Gaussian profile along the out of plane direction. Hence the brightest spots may be particles located close to the peak of the Gaussian profile, whilst particles subjected to the wings of the light sheet only produce very weak spots or form a vague background when projected onto the image plane as their temperature is much lower. This may also explain why there are fewer apparent particle images in Fig. 6.2(b) than that in (a), although they were taken at the same seeding rate. Low apparent particle image density makes LII-PIV more susceptible to the drop of seeding density than the case of Mie-PIV, especially around the mixing layer where unseeded air is entrained.

PIV works by cross-correlating particle image patterns between two frames to derive the displacement during a known time interval δt . A clear particle image pattern within the interrogation window guarantees a robust detection of the correlation peak, whereas a cross-correlation over a plain and smooth background with no particle images does not produce a unique sharp peak, and generates a spurious vector. Hence for the LII-based PIV, the background signal in Fig. 6.2(b) needs to be removed by image preprocessing before cross-correlations are made. The image preprocessing and vector calculation were performed using Davis 8.3 from LaVision, as follows. Both frames of the LII image were filtered by a high pass filter which removed the sliding background with a length scale larger than 10 pixels, and a threshold of 15 counts was applied to the filtered image to remove the noise and residual background signal. Figure 6.2(c) shows the LII image after preprocessing. Vectors were then calculated based on the processed image pairs using multipass cross-correlation with a decreasing window size (64×64 for the first pass, 32×32 for the second pass, both with 25% overlap). Vectors with a Q-factor lower than 1.2 were removed. A median filter was also applied to postprocess the obtained vector field to remove any spurious vectors. In order to show the robustness of LII-based PIV, the removed vectors were left blank without

interpolation and no further post-processing was applied. An example of the raw vector field is shown in Fig. 6.2(d).

6.3.3 Results and discussion

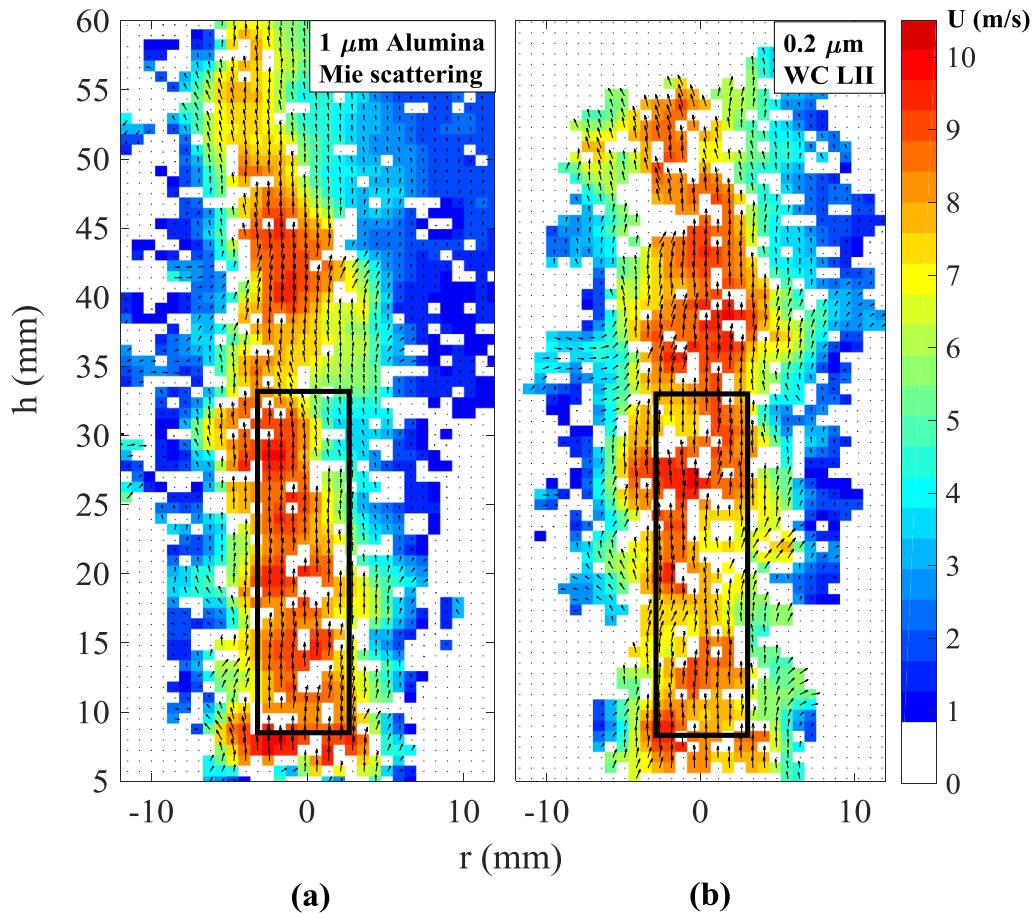


Fig. 6.3 Example of single-shot velocity field based on (a) Mie scattering of 1 μm alumina and (b) LII signal from WC. Note they were taken non-simultaneously. Removed vectors are intentionally left blank rather than interpolated. The percentage of remaining vectors in the marked region after median filtering (averaged over 400 single-shots) is 87% and 84% for Mie-scatter and LII-based PIV, respectively.

Figure 6.3 shows an example of a single-shot velocity field measured by Mie scatter and LII signal respectively. In both cases, the cross-correlation produces quite a few spurious vectors, which have been removed during postprocessing. This is not uncommon for PIV measurements on turbulent flows, as the interrogation window size (of up to ~ 1 mm) is much

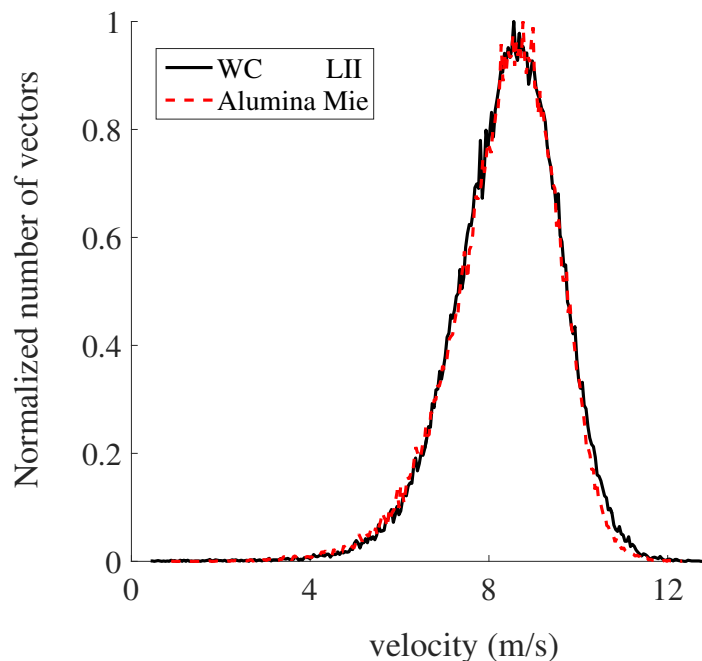


Fig. 6.4 Velocity probability density function (normalized) calculated from the marked region in Figure 6.3 over 400 single-shots. *Black line* denotes the LII-based PIV, and *red dotted line* represents the result from Mie-scatter PIV.

larger than the Kolmogorov scale, and particles within one window may move at different velocities, thus producing a weak correlation peak. The averaged percentage of remaining vectors in the marked region over the whole 400 single-shots is calculated as 87% and 84% for Mie-scatter and LII-based PIV, respectively. This is an acceptable level for a turbulent jet of $Re = 6600$. By that metric, the experiments show that LII technique is as good as traditional Mie-scatter PIV to measure single-shot velocity fields without losing too much spatial information in the core region, even though the number density of LII particle images is relatively lower than those of Mie scatter after preprocessing. The vectors on the top region of Fig. 6.3(b) are missing due to low signal to noise ratio, as the particles here are approaching the edge of the light sheet where the laser fluence drops quickly. This occurs because the LII-PIV is much more sensitive to the local laser fluence than Mie-scatter PIV, suggesting a potential limitation of the technique. The velocity probability density function

(PDF) in the same region is plotted in Fig. 6.4. The velocity PDF extracted from the LII images matches well with that from the Mie-scatter PIV images.

Figures 6.5(a) and 6.6(a) show the mean velocity $\langle U \rangle$ and its rms $\langle u \rangle$ measured with the two types of tracers, namely $1 \mu\text{m}$ alumina and submicron WC. The velocity profiles at $h = 15, 25,$ and 35 mm are extracted and compared in Fig. 6.5(b) and 6.6(b). As shown in Fig. 6.5, the LII-PIV with WC agrees well with the results given by the $1 \mu\text{m}$ alumina case (normal PIV), which shows that the selected submicron WC tracer can accurately follow the flow, and velocities can be accurately extracted from LII image pairs. The velocity rms in the shear layer obtained from LII signal is slightly higher than the normal PIV result, shown in Fig. 6.6. Again this is probably due to the entrainment of unseeded air, leading to a poorer signal to noise ratio at this location for LII images. Adding a seeded coflow with WC particles can solve this problem.

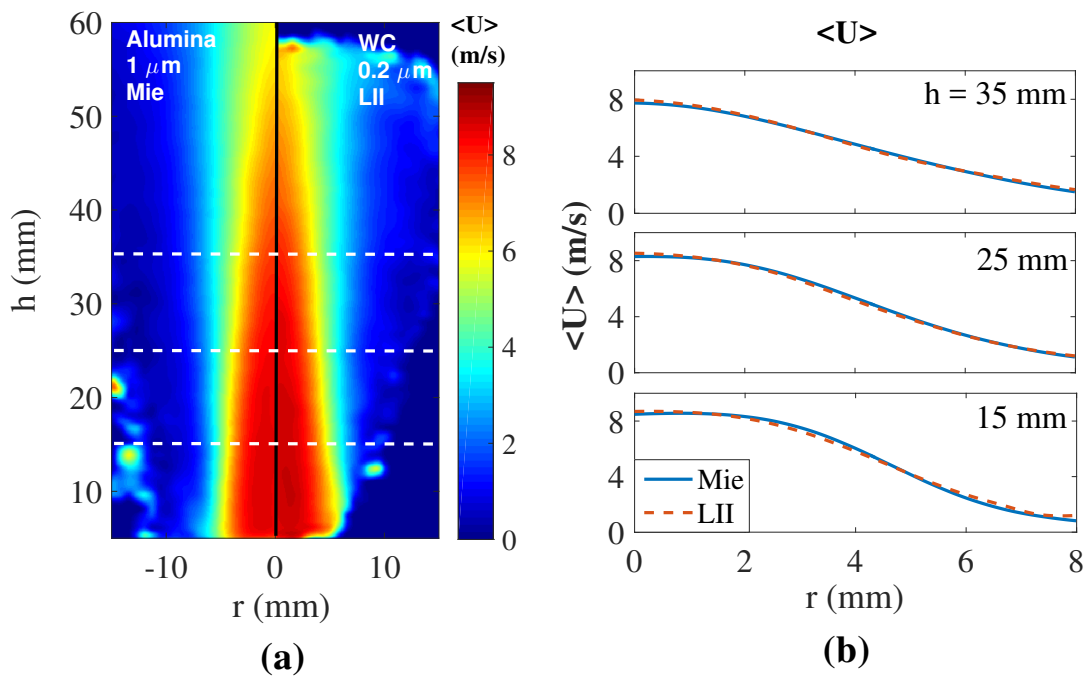


Fig. 6.5 (a) Mean velocity field for the same air jet, measured with $1 \mu\text{m}$ alumina (left half) and $0.2 \mu\text{m}$ WC (right half). (b) The velocity profiles at $h = 15, 25, 35 \text{ mm}$ are extracted and compared. The LII-PIV with WC matches well with the results given by the $1 \mu\text{m}$ alumina case (normal PIV).

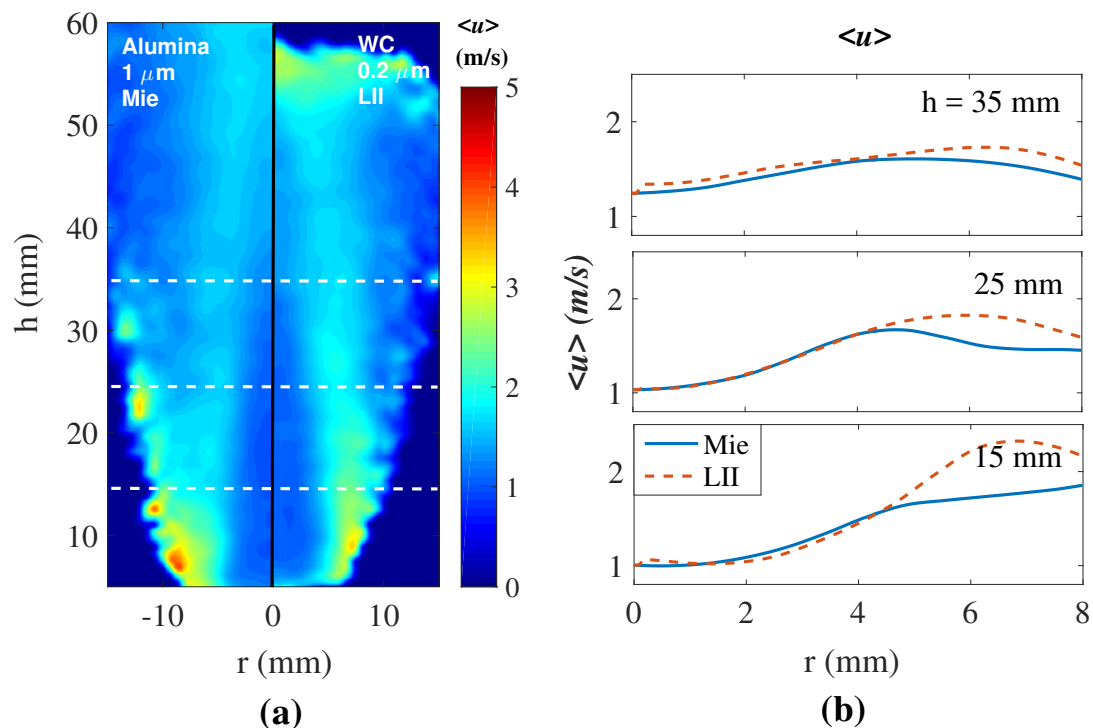


Fig. 6.6 (a) Velocity rms for the same air jet, measured with $1 \mu\text{m}$ alumina (left half) and $0.2 \mu\text{m}$ WC (right half). (b) The velocity profiles at $h = 15, 25, 35 \text{ mm}$ are extracted and compared. The velocity measurement by LII-PIV is more susceptible than Mie-PIV to the drop of seeding density in the mixing layer, hence a higher velocity rms is observed in this region.

6.4 LII-PIV on a non-reacting droplet-laden flow

6.4.1 Operating conditions

In this section, LII-based PIV was applied to measure the velocity field for the gas phase, while Mie scatter PIV is used for the liquid phase in a droplet-laden flow. A Delavan AL-06 air-assisted atomizer was used to generate ethanol droplets. Ethanol was delivered into the atomizer by a syringe pump, and the liquid flow rate was calibrated as 6 ml/min by a micro-scale. The air flow rate through the atomizer was 5 slpm , metered by a 20 slpm Alicat MFC. The atomizer was installed into the bottom of a laminar flame burner, shown in Fig. 6.7(a) schematically. The burner consists of a 90 mm diameter chamber, with a height of 260 mm which converges to an aerodynamically shaped nozzle of 22 mm exit diameter shrouded by a 5 mm wide annular co-flow. For this non-reacting case, no co-flow was used

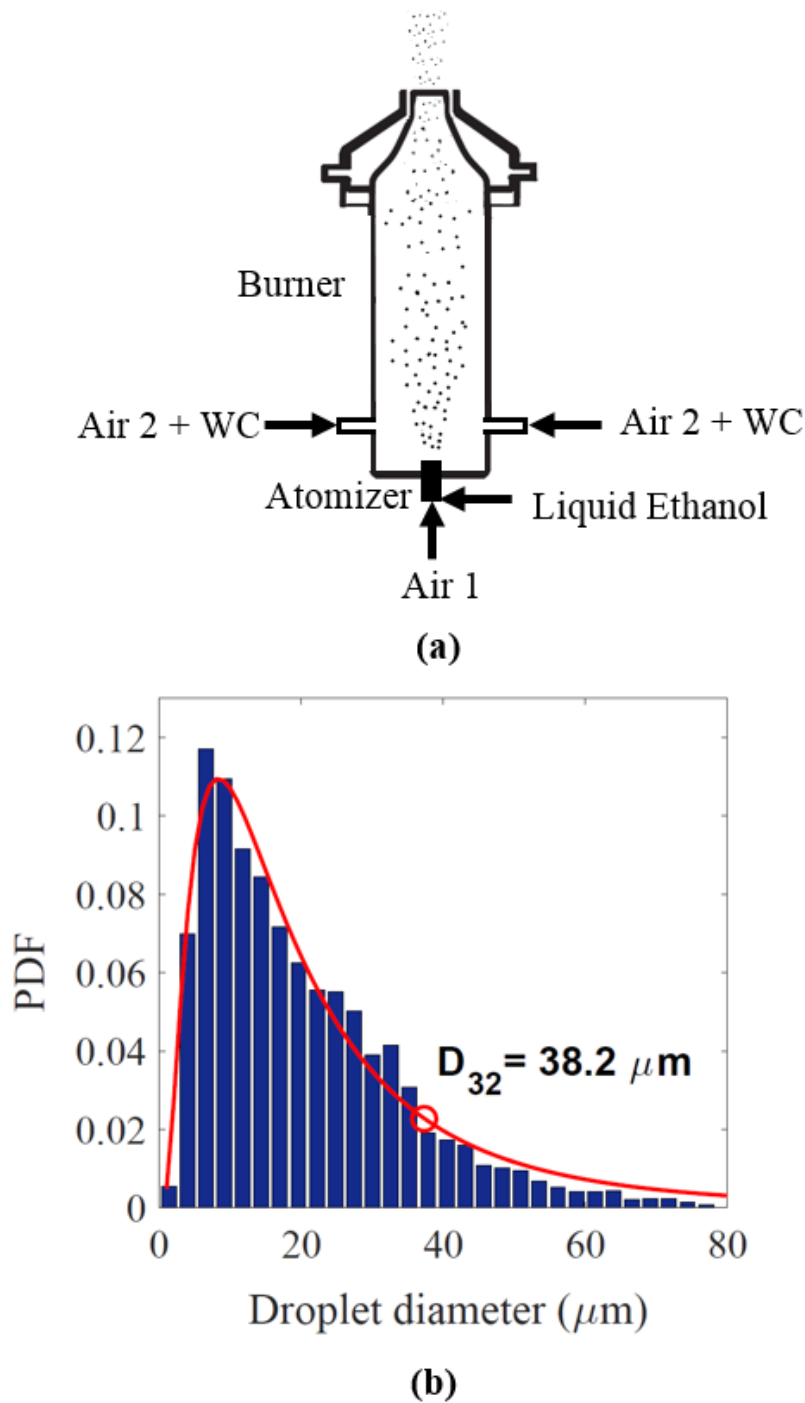


Fig. 6.7 (a) Schematic view of the laminar flame burner and the droplet-laden flow; (b) size distribution of the ethanol droplets measured by a PDA system at the outlet of the burner. A total number of 5000 droplets were sampled, and the size distribution is cut off at $80 \mu\text{m}$, limited by the mask installed in front of the PDA detector. The bars show the measured data and the red curve is the best log-normal fitting to the bars.

to shield the droplet-laden flow. In spite of the high instantaneous temperatures reached by the WC particles, no ignition was observed. The measured droplet SMD was $38.2 \mu\text{m}$ and the size distribution PDF is shown in Fig. 6.7(b), which was measured by a Dantec PDA system at the outlet of the burner. WC tracers were carried by Air 2 (35 slpm, controlled by a 50 slpm Alicat MFC, see figure 6.7(a)), which was mixed with the liquid droplets. The bulk velocity at the burner outlet was about 1.9 m/s at room temperature and $\text{Re}=2800$. The time interval between two laser pulses was set to $230 \mu\text{s}$ for this case. The atomizer itself also generated some acoustic noise and turbulence to the droplet-laden flow. Mie scatter and LII signals from the droplet/WC/air mixture were recorded separately using the same PIV camera. As mentioned in Subsection 6.2.1, a $\text{ND} = 2$ filter and a small aperture ($f/22D$) were applied to protect the CCD from overexposure when capturing the Mie scattering signal. In this configuration, the Mie scatter from the $0.2 \mu\text{m}$ WC particles cannot be detected, as it is lower than the signal scattered from the much larger ethanol droplets by several orders of magnitude. Therefore, Mie scattering from liquid droplets and LII signal from WC can be captured separately to determine the velocity field for each phase. After the two-phase PIV measurement, a conventional PIV test with $1 \mu\text{m}$ alumina particles was conducted for comparison without the presence of ethanol droplets.

6.4.2 Results and discussion: LII and droplet PIV

Figure 6.8 shows sample images of the liquid droplet (Mie) and WC particles (LII) taken from the droplet/WC/air mixture. The velocity of droplets was extracted from the former, and the gas-phase velocity from the latter. Unlike Fig. 6.2(b), the LII particles image in Fig. 6.8(b) are smeared, which is probably due to multiple scattering of the LII signal in the dense droplet cloud. However this does not affect the cross-correlation, as shown later on. Note that it would not be possible to apply any Mie-based methods to separate the gas-phase and droplet velocity for the high droplet density shown in Fig. 6.8(a).

During the mixing process in the chamber, some WC particles may be captured by the liquid, as we noticed after the experiment that some WC tracers were accumulated on the sidewall and at the bottom of the burner. This was not found for the case without the presence

of droplets. It suggests that (a) for an extremely high droplet number density, and thus a narrow interdroplet spacing, solid tracer based two-phase PIV may not be applicable as most particles will be captured by liquid, and the remaining free particles may be too sparse for conducting a successful cross-correlation; and (b) frequent cleaning may be necessary if the measurement is conducted in a confined space with sprays, such as in a chamber or cylinder. However, we note that the same issue would be present for the use of fluorescent or phosphorescent dyes on tracer particles.

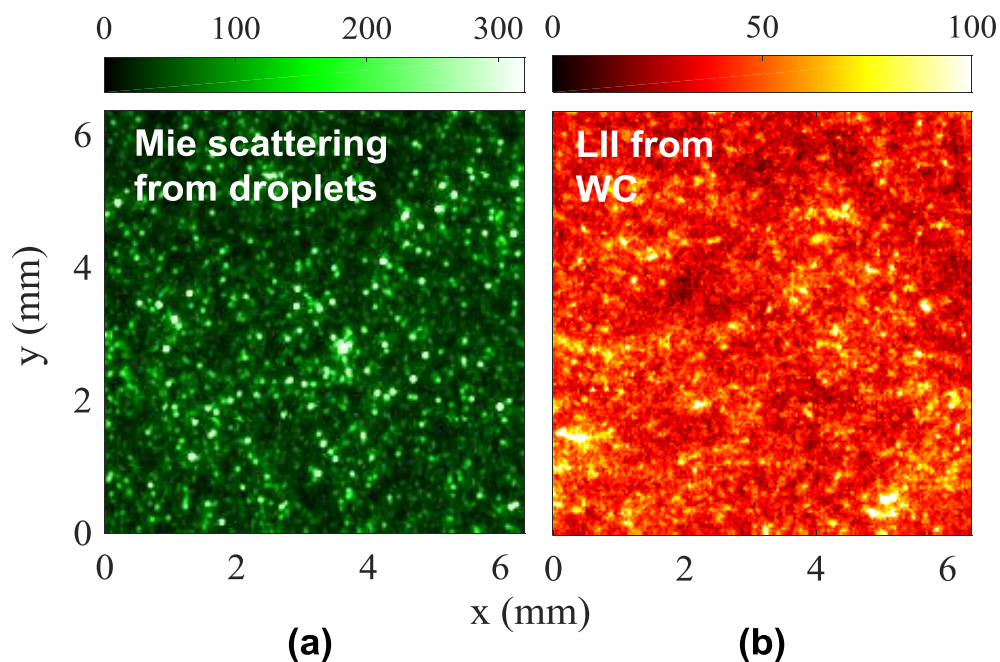


Fig. 6.8 Zoomed-in view of (a) Mie scattering and (b) LII image from the droplet/WC/air mixture.

The same data processing procedure described in subsection 6.3.2 was applied to process the PIV images and to calculate the vector field. Figure 6.9 shows the velocity field based on Mie scattering from the droplets and LII from WC particles. The former represents the velocity for the disperse phase, and the latter for the continuous phase.

Figures 6.10 and 6.11 show the mean and rms velocity measured by droplets (Mie scattering) and WC particles (LII). The mean velocity fields given by the Mie signal and LII signal are very different, as shown in Fig. 6.10(a), (b). This could be attributed to the inertia of liquid droplets, which move significantly slower than the gas. Gravity also plays a

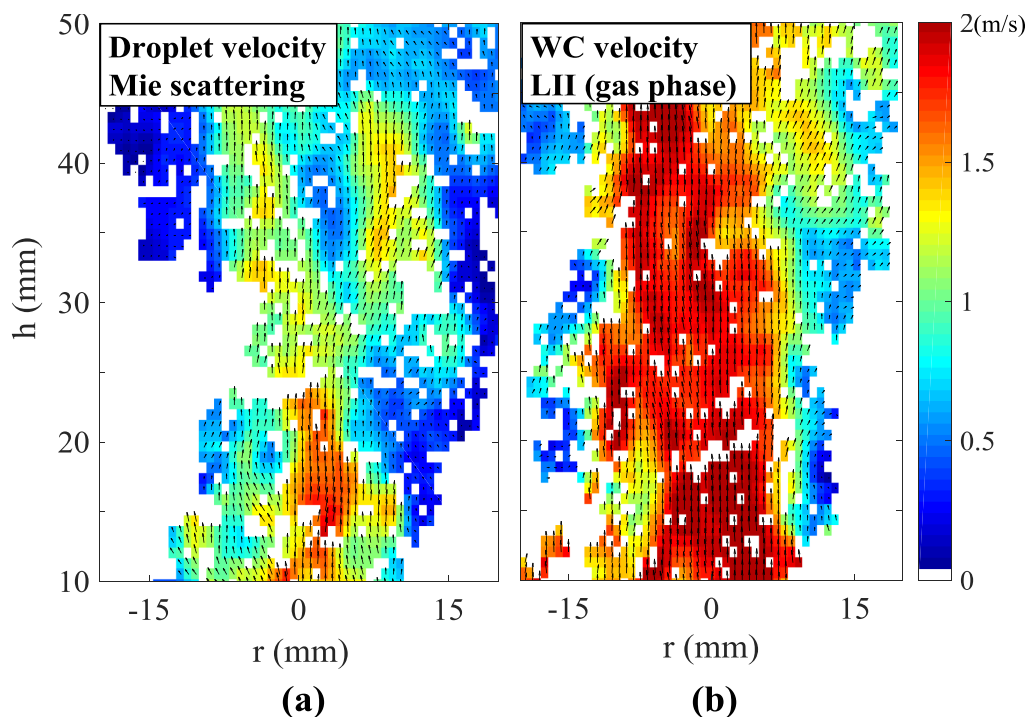


Fig. 6.9 Single-shot velocity field based on (a) Mie scattering from droplets and (b) LII signal from WC, which represents the gas-phase motion in this droplet-laden flow. Removed vectors are left blank intentionally. Note they were taken non-simultaneously.

role, as it could be verified by the observation that some droplets start to move downwards at around 10 cm above the nozzle. A quantitative comparison is made by comparing the velocity PDFs in the core region, and presented in Fig. 6.12. The slip velocity between droplets and gas-phase can be clearly observed from the PDFs. Interestingly, the gas phase velocity measured in the presence of droplets (*black line*) shows a slightly wider distribution than that with no droplets (*red dotted line*). This implies that the large droplets may interact with the gaseous flow, and lead to a higher fluctuation in the gas-phase velocity.

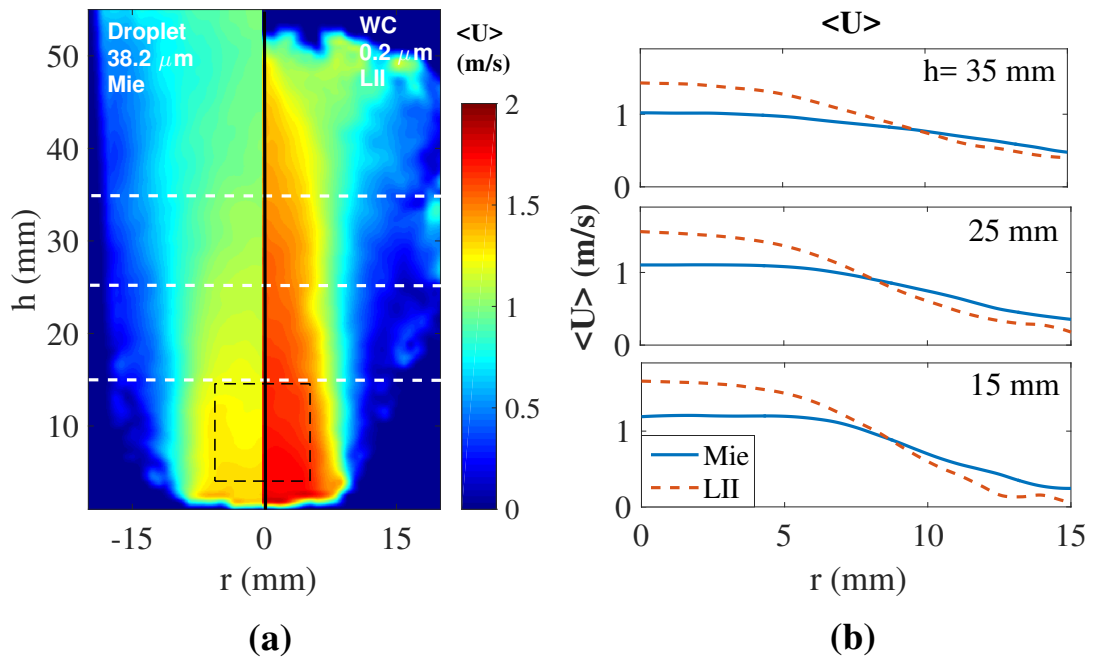


Fig. 6.10 (a) Mean velocity field of liquid phase (*left*) and gas phase (*right*); (b) The velocity profiles at $h = 15, 25, 35$ mm are extracted and compared. Ethanol droplets move significantly more slowly than the gaseous flow due to the effect of gravity relatively to the drag force. The dashed square marks the region where velocity PDFs in Fig. 6.12 are calculated.

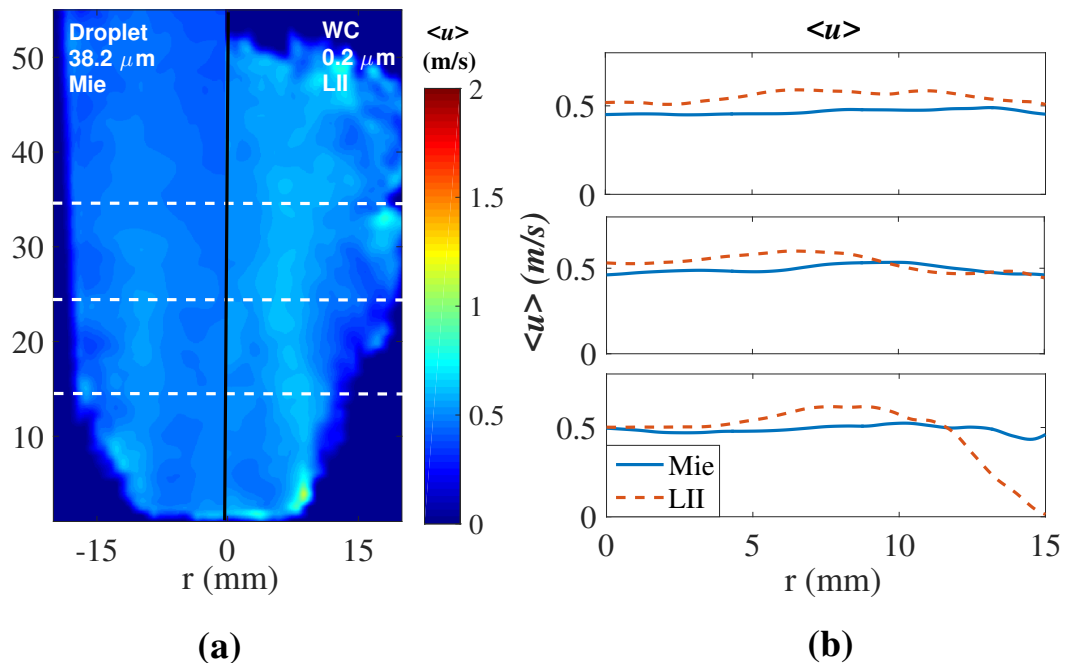


Fig. 6.11 (a) Velocity rms of liquid phase (*left*) and gas phase (*right*); (b) The velocity profiles at $h = 15, 25, 35$ mm are extracted and compared. In the jet core (well seeding) the gas-phase velocity fluctuation is slightly higher than that of the liquid-phase.

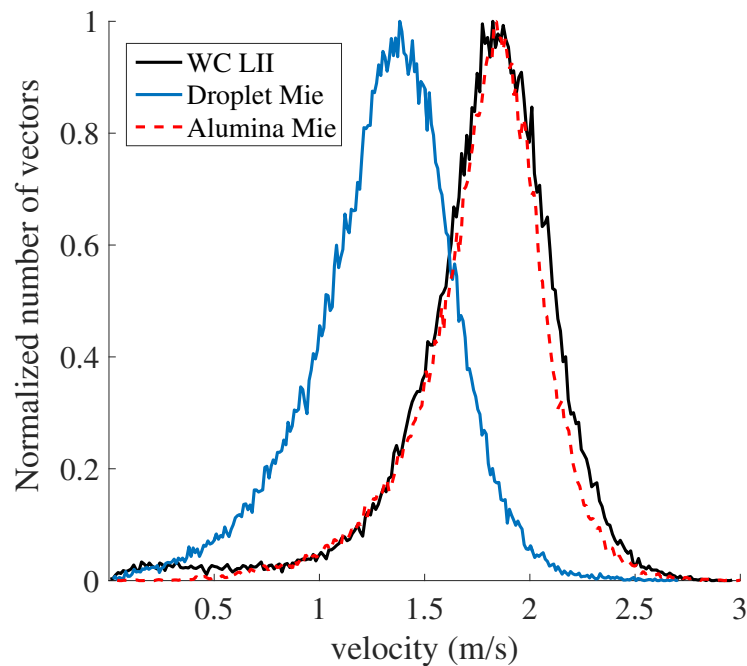


Fig. 6.12 Velocity PDFs calculated over the marked region in figure 6.10(a). *Black line* shows the gas phase velocity, whilst *blue line* presents the droplet velocity. For comparison, the velocity PDF based on 1 μm alumina (*red dotted line*) measured without the presence of droplets is also plotted.

6.5 Demonstration of LII-PIV on a flame

6.5.1 Operating conditions

In this section, the LII-PIV technique was demonstrated on a canonical stagnation flame using the same laminar flame burner, shown in Fig. 6.13. The atomizer was removed from the burner and the hole was sealed. A water-cooled brass plate was placed over the nozzle of the burner, and the distance between the plate and nozzle was fixed at 25 mm. Methane was used as the gaseous fuel with a flow rate of 2.7 slpm, metered by a 20 slpm Alicat MFC. The air flow rate was set to 30 slpm, leading to an equivalence ratio of $\phi = 0.86$. An unseeded nitrogen co-flow was controlled by a 250 slpm Alicat MFC to provide the same co-flow velocity as the main flow. A flat flame is stabilized 5 mm beneath the surface of the cooling plate. It can be observed from Fig. 6.13 that the flame luminosity is very strong due

to radiation from the seeded black WC particles; this saturates the second frame of the LII image and causes a problem for the cross-correlation in the post-flame region, as described later. Tracer particles of diameter $1\ \mu\text{m}$ alumina (normal PIV) and $0.2\ \mu\text{m}$ WC were used for Mie-scatter PIV on this reacting cases separately. For this laminar flame case, 200 images were recorded for each dataset, and a single pass of 32×32 pixel interrogation window with 25% overlap was applied to calculate the vector field.

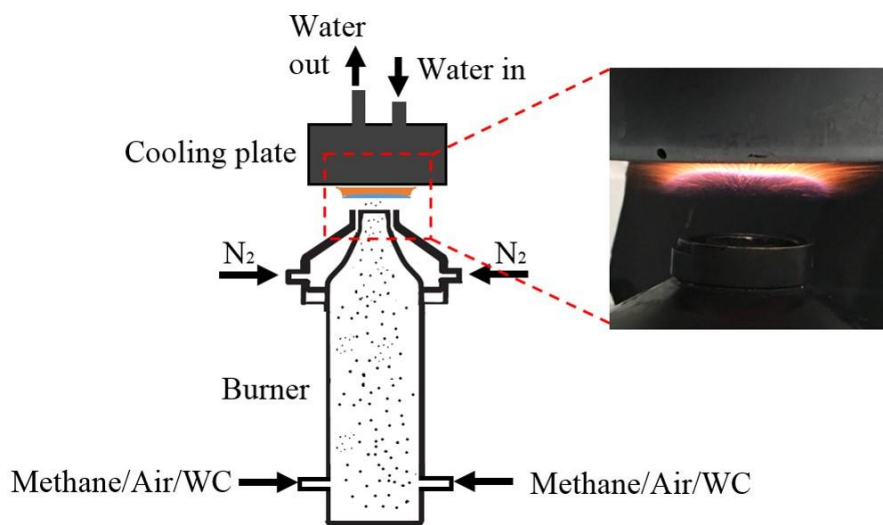


Fig. 6.13 Schematic view of the stagnation flame configuration.

6.5.2 Results and discussion: WC flame PIV

Figure 6.14 shows the result of PIV for the stagnation flame. Figure 6.14(a),(b) are sample single shot first frames of Mie scatter (*left*) and LII (*right*) respectively. The particle density drops by a factor of around seven downstream of the flame front, due to thermal expansion of the flow (thus a much lower seeding density) and the out-of-plane motion of tracer particles as they are approaching towards the cooling plate. This is found to be the case for both alumina and WC tracers. Despite the drop in seeding density, there is still sufficient particle density in both Mie scattering and LII images downstream the flame front for a robust

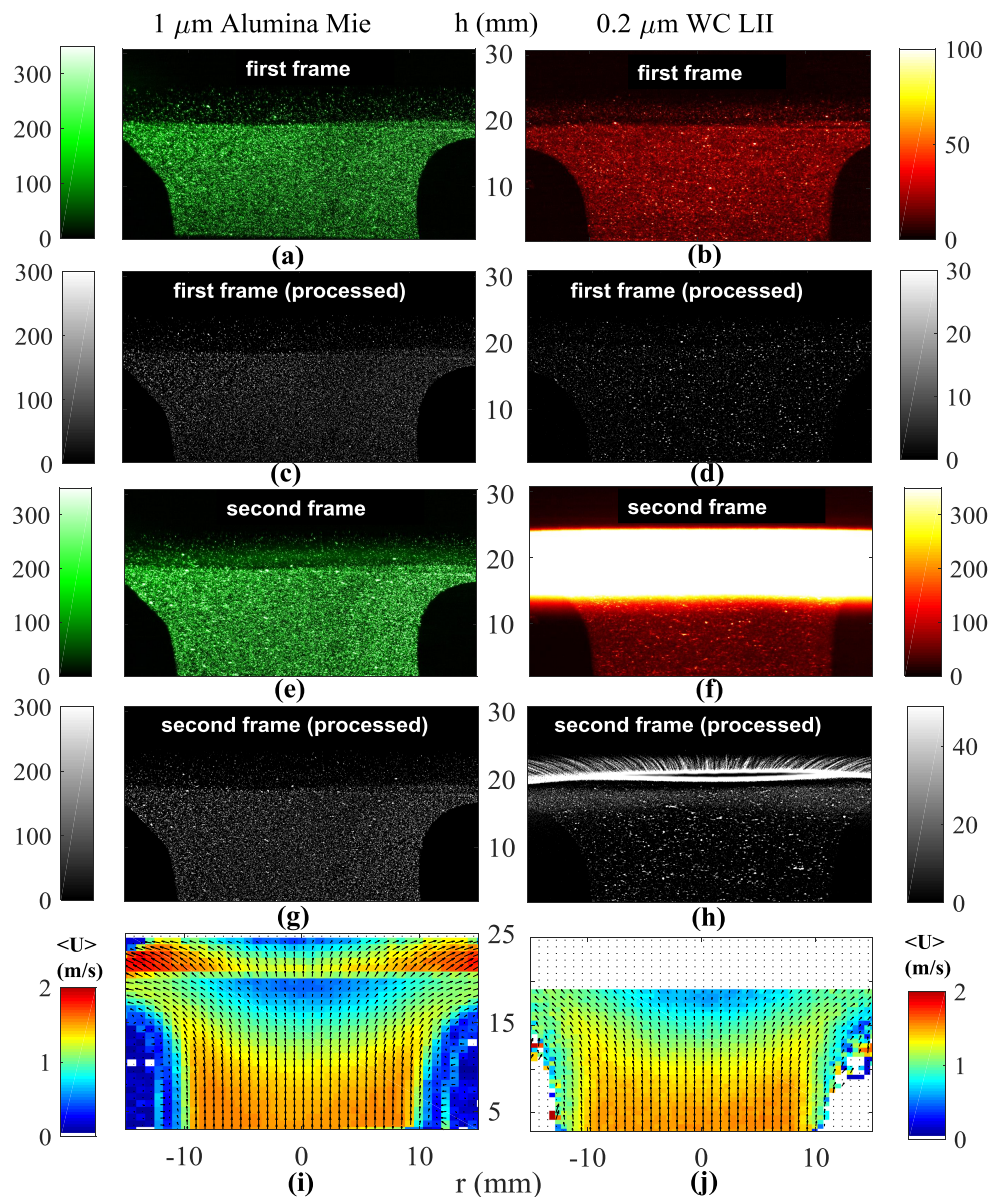


Fig. 6.14 (a,b) First frame a example PIV image; (c,d) Preprocessed image (first frame); (e,f) second frame of the PIV image; (g,h) Preprocessed image (second frame); (i,j) Mean velocity field. *Left column* is based on Mie scattering from alumina tracer, and *right column* on LII signal from tungsten carbide particles, respectively.

cross-correlation, which can be clearly seen after preprocessing the images (*second row* in Fig. 6.14). This shows a great advantage of LII-based PIV over the traditional color-based approach: if fluorescent particles were used for this case, the emission would no longer exist right downstream of the flame front due to thermal quenching and decomposition of the dopant.

However, on the second frame, the LII image becomes saturated by the flame luminosity (Fig. 6.14(f)), whilst the flame only leaves a weak signature on the Mie-scatter image (Fig. 6.14(e)). Because of the readout mechanism of the low-speed CCD camera operated in the double-frame mode, the exposure time of the second frame is much longer than the first frame. As mentioned in section 6.2.1, in the present case the shutter time for the first frame is $5 \mu\text{s}$, and $\sim 150 \text{ ms}$ for the second frame, with an inter-frame interval of 5 ns . This is a common problem for PIV measurements of luminous flames using a (low speed) CCD camera. Several solutions have been proposed to this problem: (a) using a narrow bandpass filter centered at the laser wavelength, as implemented in the present study for obtaining clean Mie-scatter images; (b) using a CMOS high-speed PIV camera operating at a high frequency, which has short exposure time for both frames; (c) reducing the gating time of the second frame with an extra shutter; and (d) using another CCD camera to record the particle images illuminated by the second laser pulse. Method (a) is not appropriate for the LII-PIV technique because black body radiation is also broadband, hence a narrow filter also reduces the strength of LII signal. Method (b) is feasible so long as the high speed laser used has sufficient output energy to generate LII signals. Method (c) has previously been demonstrated by [143], in which high flame luminosity on the second frame was removed successfully using mechanical shutters. Since the shutters are not expensive, this is a good solution for low-speed LII-PIV in flames. Method (d) is simple and straightforward, but the two cameras need to be carefully aligned, and the background displacement needs to be measured with a static target and subtracted by image mapping during the preprocessing stage. Fig. 6.14(i), (j) shows the measured velocity field based on the preprocessed images (g), (h). The LII-PIV method is capable of measuring the velocity upstream the flame front, however the vectors above 20 cm in height were lost owing to the overexposure problem. It

is expected that with an extra shutter/camera, two-phase LII-PIV measurements can also be achieved on a particle-laden or droplet-laden flame successfully. A demonstration is currently underway implementing the LII-PIV technique in flames with the use of high frequency CMOS cameras.

6.5.3 Possibility of applying LII-PIV to a sooty flame

In subsection 6.5.2, a premixed lean flame was used to demonstrate LII-PIV, where little soot was produced. If this technique were to be applied to a diffusion flame where large amounts of soot are produced, such as in [139], the LII signal from black tracers would be overwhelmed by the LII signal from soot particles, which can have a much higher volume fraction than the seeded tracers, and would have reached the sublimation temperature much earlier under the same laser fluence. However, the decay time of LII signal is proportional to the particle size, as larger particles need a longer time to cool down to the ambient temperature due to a smaller surface to volume ratio. The LII signal from soot particles usually lasts for several hundreds of nanoseconds, while the LII decay time of the tungsten carbide powder used in this study is between 1-2 μs . Hence the LII signal from soot may be gated away, or at least reduced to a separable level, by carefully selecting the tracer size and using a proper gating strategy.

6.6 Summary

In this study, a novel PIV technique based on a LII signal from seeded submicron black particles is introduced to separately measure the velocity field corresponding to the liquid and gas phases of a two-phase flow. The black tracers are heated up to several thousand degrees to emit strong incandescence signal by a double-pulsed PIV laser running at high output energy, whilst the laser-induced temperature increase in large liquid droplets or solid particles is negligible. By collecting the LII signal at a wavelength different from the Mie scattering, the motion of seeded black tracers, which represents the gaseous flow field, can be separated from the motion of the disperse phase. Experimentally the LII-PIV technique

was demonstrated on a single phase air jet, a droplet-laden flow, and finally a stagnation flame. The results were compared with those from a single-phase Mie-scatter PIV with 1 μm alumina particles. The main conclusions are summarized as follows:

- Fine and inexpensive tungsten carbide (WC) tracer particles used in this study can accurately follow the gaseous flow, and the LII images are sufficiently robust to achieve accurate velocity measurements.
- LII-PIV is a low cost but promising technique for measuring two-phase flows. In the droplet-laden flow case, by recording the Mie scattering from large droplets and the LII signal from WC particles separately, the liquid-phase and gas-phase velocities were measured independently. The LII-PIV technique is applicable to much higher droplet densities compared with previous methods.
- For the reacting case, the first frame of the LII image provides high quality particle images for cross-correlation even at the reaction and post-flame zone, whereas fluorescent or phosphorescent particles may not produce a detectable signal. However, the second frame is saturated by the flame luminosity, due to the long exposure times created in low speed PIV. This problem can be solved by applying an extra shutter to reduce the shutter time of the second frame, as demonstrated by previous research, or by using a gated or high-speed CMOS camera.
- For reacting flows, the density should be carefully controlled to avoid severe local gas heating and radiative heat loss. A seeding rate at the level of 10^{11} particles/ m^3 is sufficient for velocity measurement whilst not disturbing the flame.

Future work focuses on demonstrating the LII-PIV technique on a two-phase flame (droplet-laden and particle-laden), and on sooty diffusion flames.

Chapter 7

Conclusions and future work

7.1 Conclusions

The experiments presented in this thesis are aimed at improving the current thermographic PIV technique and extending the application of TPIV to flames with the aid of LII signal from seeded submicron black particles. The main conclusions are summarized as follows.

- (1) Thermographic PIV was demonstrated with a simplified experimental setup successfully. The phosphorescence from excited ZnO particles was proved to be suitable for conducting PIV and hence the experimental setup was to a large extent simplified comparing with previous studies. A single-cavity YAG:Nd laser installed with a third harmonic generator was operated in double-pulse mode (enabling the Q-switch twice during one flash-lamp charge) and two non-intensified CCD cameras were running in double-frame mode to record the phosphorescence signal, eliminating the need of using another PIV laser at 532 nm and an extra camera for recording the Mie scatter. Apart from the special laser used in this study, the double-pulse UV light source can also be realized by adding an external third harmonic crystal to a 532 nm PIV laser. A comparison with mean temperatures obtained by a thermocouple showed that the accuracy of ZnO thermography was within 3 K at 410 K in the jet core region. The velocity structures showed similarities to the temperature structures, and the vorticity contour was correlated with the entrainment structures shown on the temperature field.

This shows the potential of thermographic PIV for investigating fundamental problems in fluid mechanics.

- (2) Phosphor thermography with ZnO particles was applied to visualize the gas-phase temperature in a laminar jet impinging on an electrically-heated thin stainless steel foil for a Reynolds number of 3200, and a nozzle-to-foil distance from 1 to 4 nozzle diameters. Meanwhile, an infrared camera was set to record the foil surface temperature for deriving an averaged Nu profile. A heat removal mechanism by eddies was observed in the instantaneous temperature field for low nozzle-wall distances; for large nozzle-wall distances, however, the mechanism was replaced by the turbulent mixing with ambient cold air, since the eddies had broken down before reaching the wall. This can probably explain the disappearance of secondary peaks on Nu profile for large nozzle-wall distances.
- (3) A numerical study was conducted to investigate the effects of Structure Laser Illumination Planar Imaging (SLIPI) on the true phosphorescence signal originated from the measurement plane, and on the temperature retrieval. The experimental data of ZnO emission was built into the code of Synthetic PIV Image Generator (SIG), and the SLIPI process was simulated by synthesizing LIP images under a modulated laser sheet. This study reveals that the non-linear signal gain of phosphor emission will be removed by the SLIPI, which lowers down the SNR of the SLIPI recovered image and affect the quality of temperature measurement (bad precision and spatial resolution), especially for instantaneous SLIPI. This has been verified by the experimental work by Zentgraf *et al* [42]. In cases where the intensity ratio between two spectral lines depends on the excitation fluence, the temperature extracted from SLIPI image will be biased at high excitation fluences. The simulation also reports that the contribution from multiple scattering signal is always overestimated by the algorithm of SLIPI, due to non-linear emission of thermographic phosphors and particle diffraction.
- (4) In order to implement simultaneous temperature and velocity measurements in a high temperature beyond 1000 K, the concept of LII-TPIV was introduced. For

submicron particles heated by a top-hat pulsed laser sheet, the temperature increase due to absorption is the same for all individual particles regardless of their size (known as Rayleigh approximation), under the premise that they have not yet reach the sublimation point. Hence the local gas temperature can be inferred from particle peak temperature which can be measured by 2C pyrometry. Meanwhile, the Mie scattering or LII signal itself emitted from the same particles can be recorded by a PIV camera to determine the velocity field. Thus simultaneous temperature and velocity measurements can be achieved. A simplified LII model was built based on previous studies to demonstrate the feasibility of the proposed technique. The simulation shows that (a) the laser energy applied for this technique should be in a moderate range that avoids severe particle sublimation but at the same time can guarantee a robust LII signal strength, and that (b) a wide bandpass filter in near UV range combining with a narrow filter in near IR region is the best option in terms of temperature sensitivity and signal detectability. This technique is proposed as a supplement of thermographic PIV based on phosphors.

- (5) The idea of using LII signal from seeded submicron black particles to perform PIV was applied to solve a two-phase flow problem: separating the velocity field of the continuum phase from the dispersed phased (large droplets or particles). The technique was demonstrated using Tungsten carbide particles. It was tested in a single-phase air jet, compared with conventional PIV with alumina tracers, and then applied to a non-reacting droplet-laden flow. The result proves that LII-PIV can provide a velocity measurement as accurate as normal Mie-scatter PIV does, and clearly shows the existence of a slip velocity between the gas phase and liquid phase. The advantage of this LII-PIV technique over the previous ones for two-phase flow measurements is its potential to be applied in flames. However, due to the low-speed system used in the present study, the second frame of the PIV camera was saturated by flame luminosity. This can be solved by using high speed CMOS cameras operating at high frequencies, or adding an extra camera to capture the second pulse with a short gating time.

7.2 Future work

A number of interesting opportunities for future work can be foreseen based on the studies presented in this thesis.

7.2.1 Experimental demonstration of LII-TPIV

The theory of LII-based thermographic PIV has been examined by conducting numeric studies with the adapted LII soot model. The next step is to demonstrate this technique experimentally. Several issues are to be investigated thoroughly, including (a) selection of a laser fluence to gain high LII signal strength but at the same time to avoid severe sublimation for the seeded tracers; (b) gating strategies (delayed gating) to avoid the interference from laser-induced fluorescence from the radicals, or LII signal from soot in a flame; and (c) accuracy in temperature measurements by comparing with other techniques such as CARS.

7.2.2 C-dot thermographic PIV

The size of commercial thermographic phosphor particles usually ranges from 1-5 μm . According to the study by Fond *et al* [16], the relaxation time for a 2 μm YAG particle is roughly 48.5 μs for an ambient gas temperature at 1150 K. For low speed flows, indeed a temperature response time of the order of tens microseconds will not affect the temperature accuracy. However, for flows with a higher speed, substantial error may appear. These commercial phosphor particles may fail to work for supersonic flow studies such as the heat transfer in a scramjet. One straightforward solution to this problem is reducing the particle size. However, 5 μm is roughly the upper limit that can be achieved by most commonly used mechanical methods such as ball milling. Further reducing the particle size takes much more efforts and a higher cost.

For supersonic TPIV measurements, carbon dot (C-dot) may be a promising candidate tracer. C-dot is a new class for carbon nanomaterials emerged in recent years in the material science. It has a primary size of several nanometers, and emits fluorescence signal under UV excitation as phosphors do. However, the size and emission spectrum of C-dots can be tuned

by carefully controlling the synthesis process [144]. It is regarded as a promising tool for bioimaging since its biocompatibility and also as a substitute of traditional Quantum dots. Carbon dots can be synthesized rather easily, and in large scale. Surprisingly, the raw material for carbon dots can be even soot [145], or orange peels [146]. Hence the cost for carbon dots synthesis can be very low once mass production has been launched. At least one paper [147] has reported the temperature dependency of the fluorescence emission from C-dot, as shown in figure 7.1(c). In addition, the repeatability of the emission spectrum measurement in the same solution at 100 °C is good even after several days, suggesting carbon dots are stable in solution form.

Figure 7.1 (a)(b)(c) are removed for the copy right reason.
Copyright holders are (a) H. Liu, (b) L. Cao, and (c) K.K.R. Datta, respectively.

Fig. 7.1 (a) Carbon dot solutions synthesized from candle soot, after [145]. The emission spectrum changes with the fraction of soot added into the reaction; (b) fluorescence image of C-dots depositing on a glass substrate by spray, under 365 nm argon laser excitation, adapted from [148]; (c) the emission spectrum of carbon dots shows some temperature dependency, adapted from [147].

C-dots in both powder and solution form can be purchased from chemical suppliers such as Sigma Aldrich. Future work focus on investigating the temperature dependency of their emission spectrum, as well as exploring the feasibility of using C-dot particles to perform simultaneous temperature and velocity imaging in fluids.

7.2.3 Thermographic phosphor synthesis by the impregnation method

The conventional way to synthesize phosphor is by firing the oxides of constituent elements. Although this method allows large scale production of phosphor particles, it is not suitable for producing thermographic phosphors. To guarantee a short relaxation time thermographic phosphor particles should be less than $2\ \mu\text{m}$. However, strong grinding and sieving firing-synthesized phosphors to such a small size severely lowers the emission efficiency [149]. One possible explanation is that destruction of primary particles exposes non-luminescent, amorphous layers and thus reduce the overall emission efficiency, as illustrated in figure 7.2(a). This is largely due to insufficient mixing and thermal treating to molecules inside the particles. To solve this, the Sol-Gel method was applied to produce thermographic phosphor particle [43] since ions were well mixed in solutions. However, the Sol-Gel method for phosphor synthesis involves the use of nitrate solutions and production of NO, which sets obstacles to kilogram-scale production of phosphor particles in laboratories.

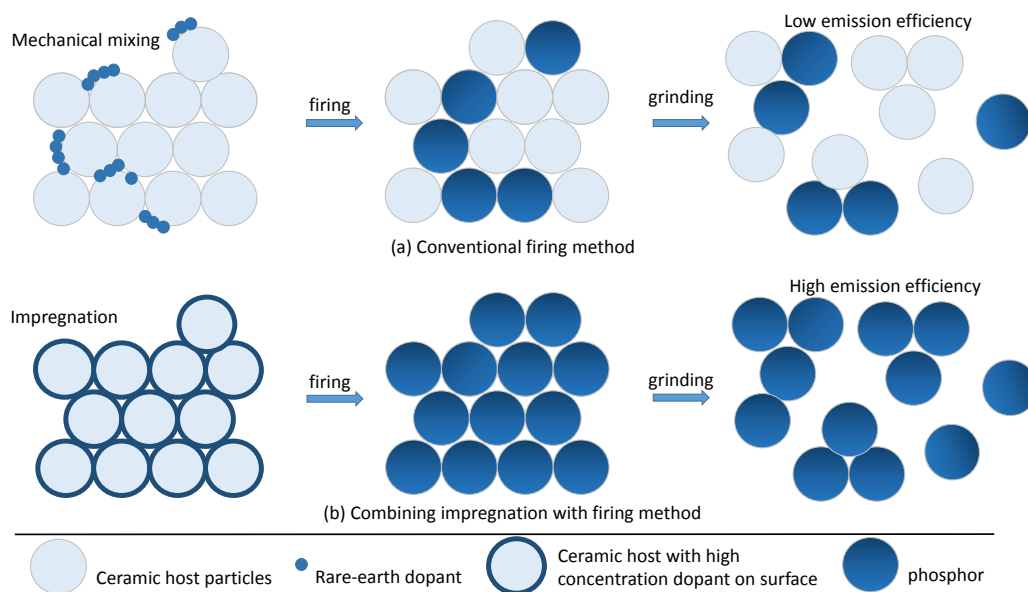


Fig. 7.2 A schematic of (a) conventional firing method for phosphor synthesis, and (b) proposed method combining impregnation and firing for phosphor synthesis.

An alternative could be sintering the dopant-impregnated host particles, illustrated in figure 7.2(b). This has been demonstrated in a recent paper [150]. In that work, Eu^{3+} impregnated CeO_2 nanocrystals were thermal treated at a moderate temperature of 1300

C° and a conversion of Eu³⁺ ions from surface to bulk sites was found. This study sheds light on a new approach for synthesizing thermographic phosphors, describe as follows: (a) synthesizing the ceramic host by the firing method, (b) breaking down the host particles by an ultrasonic homogenizer in liquid and forming a turbid suspension, (c) adding dopant solution to the host particle suspension, (d) stirring the mixture until the liquid is fully evaporated, and (e) baking the dopant-impregnated host particles at a moderate temperature to produce phosphors. The phosphor particles synthesized in this way is expected to keep a high emission efficiency even after long-time grinding, and thus suitable for gas-phase temperature measurement.

7.2.4 Simultaneous temperature and velocity imaging on a droplet-laden flat flame by TPIV

The future work proposed in this subsection connects the thermography technique to a droplet-laden flame study. In that study, the presence of acetone droplet was found to suppress the burning rate of a methane/air flat flame, which was probably attributed to the fact that the evaporation of liquid fuel had absorbed a considerable amount of heat and thus inhibited the first stage reaction. This can be indirectly verified from the observation during the experiments that for cases where the droplet size is very fine, the flame appeared to be very weak and easily extinguished at lean conditions. To confirm this correlation between the gas temperature upstream the flame front and the reference flame speed S_{ref} , we propose to disperse BAM:Eu²⁺ particles to the acetone droplets/methane/air mixture to measure the gas temperature and velocity simultaneously at the thermal expansion zone, and to compare with the case where liquid fuel is fully vaporized.

7.2.5 LII-PIV on a droplet-laden flame and a sooting flame

In Chapter 6, the LII-PIV technique was demonstrated on a non-reacting droplet-laden flow. However, for a reacting case the flame luminosity caused by the black particles saturated the second frame for low-speed PIV cameras. Hence we propose to use a high-speed PIV

laser and two CMOS high-speed cameras to repeat the same experiment on the flat flame, but reducing the height of the illumination area down to 1 to 2 cm so as to guarantee a sufficient laser fluence for the high speed laser used. If the attempt with the high-speed system succeed, this technique will then be used to measure a droplet-laden flame and later a sooty two-phase flame (for example on the coal burner used in [142]).

References

- [1] J. Westerweel, A. Petracchi, R. Delfos, and J. C. R. Hunt, “Characteristics of the turbulent/non-turbulent interface of a non-isothermal jet,” *Philosophical transactions. Series A, Mathematical, physical, and engineering sciences*, vol. 369, pp. 723–737, 2011.
- [2] D. Hofmann and A. Leipertz, “Temperature field measurements in a sooting flame by filtered Rayleigh scattering (FRS),” in *Symposium (International) on Combustion, Naples*, vol. 26, pp. 945–950, 1996.
- [3] D. Müller, R. Pagel, A. Burkert, V. Wagner, and W. Paa, “Two-dimensional temperature measurements in particle loaded technical flames by filtered Rayleigh scattering,” *Applied Optics*, vol. 53, no. 9, pp. 1750–1758, 2014.
- [4] G. Elliott, N. Glumac, C. Carter, and A. Nejad, “Two-dimensional temperature field measurements using a molecular filter based technique,” *Combustion Science and Technology*, vol. 125, no. 1-6, pp. 351–369, 1997.
- [5] G. S. Elliott, N. Glumac, and C. D. Carter, “Molecular filtered Rayleigh scattering applied to combustion,” *Measurement Science and Technology*, vol. 12, no. 4, pp. 452–466, 2001.
- [6] D. Most and A. Leipertz, “Simultaneous Two-Dimensional Flow Velocity and Gas Temperature Measurements by use of a Combined Particle Image Velocimetry and Filtered Rayleigh Scattering Technique,” *Applied Optics*, vol. 40, no. 30, pp. 5379–5387, 2001.
- [7] W. Bessler and C. Schulz, “Quantitative multi-line NO-LIF temperature imaging,” *Applied Physics B*, vol. 78, no. 5, pp. 519–533, 2004.
- [8] R. Cattolica, “OH rotational temperature from two-line laser-excited fluorescence,” *Applied Optics*, vol. 20, no. 7, pp. 1156–66, 1981.
- [9] C. Jainski, L. Lu, V. Sick, and A. Dreizler, “Laser imaging investigation of transient heat transfer processes in turbulent nitrogen jets impinging on a heated wall,” *International Journal of Heat and Mass Transfer*, vol. 74, pp. 101–112, 2014.
- [10] A. S. Nebuchinov, Y. A. Lozhkin, A. V. Bilsky, and D. M. Markovich, “Combination of PIV and PLIF methods to study convective heat transfer in an impinging jet,” *Experimental Thermal and Fluid Science*, vol. 80, pp. 139–146, 2017.

- [11] S. W. Allison and G. T. Gillies, "Remote thermometry with thermographic phosphors: Instrumentation and applications," *Review of Scientific Instruments*, vol. 68, no. 7, pp. 2615–2650, 1997.
- [12] J. Brübach, C. Pflitsch, A. Dreizler, and B. Atakan, "On surface temperature measurements with thermographic phosphors: A review," *Progress in Energy and Combustion Science*, vol. 39, no. 1, pp. 37–60, 2013.
- [13] M. Aldén, A. Omrane, M. Richter, and G. Särner, "Thermographic phosphors for thermometry: A survey of combustion applications," *Progress in Energy and Combustion Science*, vol. 37, no. 4, pp. 422–461, 2011.
- [14] C. Abram, B. Fond, and F. Beyrau, "Temperature measurement techniques for gas and liquid flows using thermographic phosphor tracer particles," *Progress in Energy and Combustion Science*, vol. 64, pp. 93–156, 2018.
- [15] A. H. Khalid and K. Kontis, "Thermographic Phosphors for High Temperature Measurements: Principles, Current State of the Art and Recent Applications," *Sensors*, vol. 8, no. 9, pp. 5673–5744, 2008.
- [16] B. Fond, C. Abram, A. L. Heyes, A. M. Kempf, and F. Beyrau, "Simultaneous temperature, mixture fraction and velocity imaging in turbulent flows using thermographic phosphor tracer particles.," *Optics Express*, vol. 20, no. 20, pp. 22118–33, 2012.
- [17] J. Feist, A. Heyes, K. Choy, and B. Su, "Phosphor thermometry for high temperature gas turbine applications," in *ICIASF 99. 18th International Congress on Instrumentation in Aerospace Simulation Facilities, Toulouse*, pp. 6/1–6/7, IEEE, 1999.
- [18] N. Fuhrmann, J. Brübach, and A. Dreizler, "Phosphor thermometry: A comparison of the luminescence lifetime and the intensity ratio approach," *Proceedings of the Combustion Institute*, vol. 34, no. 2, pp. 3611–3618, 2013.
- [19] J. Brübach, A. Patt, and A. Dreizler, "Spray thermometry using thermographic phosphors," *Applied Physics B*, vol. 83, no. 4, pp. 499–502, 2006.
- [20] R. Hasegawa, I. Sakata, H. Yanagihara, B. Johansson, A. Omrane, and M. Aldén, "Two-dimensional gas-phase temperature measurements using phosphor thermometry," *Applied Physics B*, vol. 88, no. 2, pp. 291–296, 2007.
- [21] D. A. Rothamer and J. Jordan, "Planar imaging thermometry in gaseous flows using upconversion excitation of thermographic phosphors," *Applied Physics B*, vol. 106, no. 2, pp. 435–444, 2011.
- [22] J. P. J. van Lipzig, M. Yu, N. J. Dam, C. C. M. Luijten, and L. P. H. de Goey, "Gas-phase thermometry in a high-pressure cell using $\text{BaMgAl}_{10}\text{O}_{17}:\text{Eu}$ as a thermographic phosphor," *Applied Physics B*, vol. 111, no. 3, pp. 469–481, 2013.
- [23] M. Lawrence, H. Zhao, and L. Ganippa, "Gas phase thermometry of hot turbulent jets using laser induced phosphorescence.," *Optics Express*, vol. 21, no. 10, pp. 12260–81, 2013.

- [24] G. Jovicic, L. Zigan, S. Will, and A. Leipertz, "Phosphor thermometry in turbulent hot gas flows applying Dy:YAG and Dy:Er:YAG particles," *Measurement Science and Technology*, vol. 26, no. 1, pp. 015204–13, 2015.
- [25] P. Schreivogel, C. Abram, B. Fond, M. Straußwald, F. Beyrau, and M. Pfitzner, "Simultaneous kHz-rate temperature and velocity field measurements in the flow emanating from angled and trenched film cooling holes," *International Journal of Heat and Mass Transfer*, vol. 103, pp. 390–400, 2016.
- [26] B. Fond, C. Abram, and F. Beyrau, "Characterisation of the luminescence properties of BAM:Eu²⁺ particles as a tracer for thermographic particle image velocimetry," *Applied Physics B*, vol. 121, no. 4, pp. 495–509, 2015.
- [27] B. Fond, C. Abram, and F. Beyrau, "On the characterisation of tracer particles for thermographic particle image velocimetry," *Applied Physics B*, vol. 118, no. 3, pp. 393–399, 2015.
- [28] S. J. Yi, H. D. Kim, and K. C. Kim, "Decay-slope method for 2-dimensional temperature field measurement using thermographic phosphors," *Experimental Thermal and Fluid Science*, vol. 59, pp. 1–8, 2014.
- [29] A. Omrane, P. Petersson, M. Aldén, and M. Linne, "Simultaneous 2D flow velocity and gas temperature measurements using thermographic phosphors," *Applied Physics B*, vol. 92, no. 1, pp. 99–102, 2008.
- [30] G. Jovicic, L. Zigan, S. Pfadler, and A. Leipertz, "Simultaneous Two-dimensional Temperature and Velocity Measurements in a Gas Flow Applying Thermographic Phosphors," *16th International Symposium on Applications of Laser Techniques to Fluid Mechanics Lisbon, Portugal*, 2012.
- [31] N. J. Neal, J. Jordan, and D. Rothamer, "Simultaneous Measurements of In-Cylinder Temperature and Velocity Distribution in a Small-Bore Diesel Engine Using Thermographic Phosphors," *SAE International Journal of Engines*, vol. 6, no. 1, pp. 300–318, 2013.
- [32] C. Abram, B. Fond, A. L. Heyes, and F. Beyrau, "High-speed planar thermometry and velocimetry using thermographic phosphor particles," *Applied Physics B*, vol. 111, no. 2, pp. 155–160, 2013.
- [33] A. O. Ojo, B. Fond, G. M. V. B. Wachem, L. A. Heyes, and F. Beyrau, "Thermographic laser Doppler velocimetry," *Optics Letters*, vol. 40, no. 20, pp. 1–4, 2015.
- [34] A. O. Ojo, B. Fond, C. Abram, B. G. M. Van Wachem, A. L. Heyes, and F. Beyrau, "Thermographic laser Doppler velocimetry using the phase-shifted luminescence of BAM:Eu²⁺ phosphor particles for thermometry," *Optics Express*, vol. 25, no. 10, pp. 11833–43, 2017.
- [35] S. Someya, Y. Okura, M. Uchida, Y. Sato, and K. Okamoto, "Combined velocity and temperature imaging of gas flow in an engine cylinder," *Optics Letters*, vol. 37, no. 23, pp. 4964–4966, 2012.

- [36] S. Pouya, M. Koochesfahani, P. Snee, M. Bawendi, and D. Nocera, "Single quantum dot (QD) imaging of fluid flow near surfaces," *Experiments in Fluids*, vol. 39, no. 4, pp. 784–786, 2005.
- [37] J. S. Guasto, P. Huang, and K. S. Breuer, "Statistical particle tracking velocimetry using molecular and quantum dot tracer particles," *Experiments in Fluids*, vol. 41, no. 6, pp. 869–880, 2006.
- [38] J. S. Guasto and K. S. Breuer, "Simultaneous, ensemble-averaged measurement of near-wall temperature and velocity in steady micro-flows using single quantum dot tracking," *Experiments in Fluids*, vol. 45, no. 1, pp. 157–166, 2008.
- [39] Z. Yin, B. Fond, G. Eckel, C. Abram, W. Meier, I. Boxx, and F. Beyrau, "Investigation of BAM:Eu²⁺ particles as a tracer for temperature imaging in flames," *Combustion and Flame*, vol. 184, pp. 249–251, 2017.
- [40] M. Stephan, H. Lee, B. Albert, A. Dreizler, and B. Böhm, "Simultaneous planar gas - phase temperature and velocity measurements within a film cooling configuration using thermographic phosphors," *18th International Symposium on the Application of Laser and Imaging Techniques to Fluid Mechanics, Lisbon*, 2016.
- [41] H. Lee, B. Böhm, A. Sadiki, and A. Dreizler, "Turbulent heat flux measurement in a non-reacting round jet, using BAM:Eu²⁺ phosphor thermography and particle image velocimetry," *Applied Physics B*, vol. 122, no. 7, pp. 1–13, 2016.
- [42] F. Zentgraf, M. Stephan, E. Berrocal, B. Albert, B. Böhm, and A. Dreizler, "Application of structured illumination to gas phase thermometry using thermographic phosphor particles: a study for averaged imaging," *Experiments in Fluids*, vol. 58, no. 8, pp. 1–15, 2017.
- [43] Á. Y. González, S. Skinner, F. Beyrau, and A. L. Heyes, "Reusable Thermal History Sensing via Oxidation of a Divalent Rare Earth Ion-Based Phosphor Synthesized by the Sol-Gel Process," *Heat Transfer Engineering*, vol. 36, no. 14-15, pp. 1275–1281, 2015.
- [44] C. Abram, M. Pougin, and F. Beyrau, "Temperature field measurements in liquids using ZnO thermographic phosphor tracer particles," *Experiments in Fluids*, vol. 57, no. 7, pp. 1–14, 2016.
- [45] P. Rodnyi and I. Khodyuk, "Optical and luminescence properties of zinc oxide (Review)," *Optics and Spectroscopy*, vol. 111, no. 5, pp. 776–785, 2011.
- [46] Continuum, "Laser operation manual, double pulse option," 1995.
- [47] R. D. Keane and R. J. Adrian, "Optimization of particle image velocimeters. I. Double pulsed systems," *Measurement Science and Technology*, vol. 1, no. 11, pp. 1202–1215, 1990.
- [48] R. D. Keane and R. J. Adrian, "Theory of cross-correlation analysis of PIV images," *Applied Scientific Research*, vol. 49, no. 3, pp. 191–215, 1992.

- [49] M. Angioletti, R. M. Di Tommaso, E. Nino, and G. Ruocco, "Simultaneous visualization of flow field and evaluation of local heat transfer by transitional impinging jets," *International Journal of Heat and Mass Transfer*, vol. 46, no. 10, pp. 1703–1713, 2003.
- [50] K. Jambunathan, E. Lai, M. A. Moss, and B. L. Button, "A review of heat-transfer data for single circular jet impingement," *International Journal of Heat and Fluid Flow*, vol. 13, no. 2, pp. 106–115, 1992.
- [51] R. Viskanta, "Nusselt-Reynolds Prize Paper Heat Transfer to Impinging Isothermal Gas and Flame Jets," pp. 111–134, 1993.
- [52] N. Zuckerman and N. Lior, "Impingement Heat Transfer: Correlations and Numerical Modeling," *Journal of Heat Transfer*, vol. 127, no. 5, pp. 544–552, 2005.
- [53] A. Dewan, R. Dutta, and B. Srinivasan, "Recent trends in computation of turbulent jet impingement heat transfer," *Heat Transfer Engineering*, vol. 33, no. 4-5, pp. 447–460, 2012.
- [54] R. J. Goldstein, A. I. Behbahani, and K. K. Heppelmann, "Streamwise distribution of the recovery factor and the local heat transfer coefficient to an impinging circular air jet," *International Journal of Heat and Mass Transfer*, vol. 29, no. 8, pp. 1227–1235, 1986.
- [55] D. Lytle and B. W. Webb, "Air jet impingement heat transfer at low nozzle-plate spacings," *International Journal of Heat and Mass Transfer*, vol. 31, no. 12, pp. 1687–1697, 1994.
- [56] T. S. O'Donovan and D. B. Murray, "Jet impingement heat transfer - Part I: Mean and root-mean-square heat transfer and velocity distributions," *International Journal of Heat and Mass Transfer*, vol. 50, no. 17-18, pp. 3291–3301, 2007.
- [57] P. Gulati, V. Katti, and S. V. Prabhu, "Influence of the shape of the nozzle on local heat transfer distribution between smooth flat surface and impinging air jet," *International Journal of Thermal Sciences*, vol. 48, no. 3, pp. 602–617, 2009.
- [58] O. Caggese, G. Gnaegi, G. Hannema, A. Terzis, and P. Ott, "Experimental and numerical investigation of a fully confined impingement round jet," *International Journal of Heat and Mass Transfer*, vol. 65, pp. 873–882, 2013.
- [59] P. Brevet, C. Dejeu, E. Dorignac, M. Jolly, and J. J. Vullierme, "Heat transfer to a row of impinging jets in consideration of optimization," *International Journal of Heat and Mass Transfer*, vol. 45, no. 20, pp. 4191–4200, 2002.
- [60] L. F. G. Geers, M. J. Tummers, T. J. Bueninck, and K. Hanjalić, "Heat transfer correlation for hexagonal and in-line arrays of impinging jets," *International Journal of Heat and Mass Transfer*, vol. 51, no. 21-22, pp. 5389–5399, 2008.
- [61] M. Goodro, J. Park, P. Ligrani, M. Fox, and H. K. Moon, "Effects of hole spacing on spatially-resolved jet array impingement heat transfer," *International Journal of Heat and Mass Transfer*, vol. 51, no. 25-26, pp. 6243–6253, 2008.

- [62] Y. Xing, S. Spring, and B. Weigand, "Experimental and Numerical Investigation of Heat Transfer Characteristics of Inline and Staggered Arrays of Impinging Jets," *Journal of Heat Transfer*, vol. 132, no. 9, pp. 092201–11, 2010.
- [63] S. Roux, M. Fénot, G. Lalizel, L. E. Brizzi, and E. Dorignac, "Experimental investigation of the flow and heat transfer of an impinging jet under acoustic excitation," *International Journal of Heat and Mass Transfer*, vol. 54, no. 15-16, pp. 3277–3290, 2011.
- [64] S. Roux, M. Fénot, G. Lalizel, L. E. Brizzi, and E. Dorignac, "Evidence of flow vortex signatures on wall fluctuating temperature using unsteady infrared thermography for an acoustically forced impinging jet," *International Journal of Heat and Fluid Flow*, vol. 50, pp. 38–50, 2014.
- [65] M. Pakhomov and V. Terekhov, "Numerical study of fluid flow and heat transfer characteristics in an intermittent turbulent impinging round jet," *International Journal of Thermal Sciences*, vol. 87, pp. 85–93, 2015.
- [66] C. T. Chang, G. Kojasoy, F. Landis, and S. Downing, "Confined single- and multiple-jet impingement heat transfer-I. Turbulent submerged liquid jets," *International Journal of Heat and Mass Transfer*, vol. 38, no. 5, pp. 833–842, 1995.
- [67] D. Trainer, J. Kim, and S. J. Kim, "Heat transfer and flow characteristics of air-assisted impinging water jets," *International Journal of Heat and Mass Transfer*, vol. 64, pp. 501–513, 2013.
- [68] C. Quinn, "Heat transfer behaviour of a dilute impinging air-water mist jet," *International Journal of Heat and Mass Transfer*, vol. 111, pp. 1234–1249, 2015.
- [69] D. Lee, R. Greif, S. J. Lee, and J. H. Lee, "Heat Transfer From a Flat Plate to a Fully Developed Axisymmetric Impinging Jet," *Journal of Heat Transfer*, vol. 117, no. 3, pp. 772–776, 1995.
- [70] S. Ashforth-Frost and K. Jambunathan, "Effect of nozzle geometry and semi-confinement on the potential core of a turbulent axisymmetric free jet," *International Communications in Heat and Mass Transfer*, vol. 23, no. 2, pp. 155–162, 1996.
- [71] S. Huang, L., El-Genk, M., "Heat transfer of an impinging jet on a flat surface," *International Journal of Heat and Mass Transfer*, vol. 37, no. 13, pp. 1915–1923, 1994.
- [72] T. S. O'Donovan and D. B. Murray, "Jet impingement heat transfer - Part II: A temporal investigation of heat transfer and local fluid velocities," *International Journal of Heat and Mass Transfer*, vol. 50, no. 17-18, pp. 3302–3314, 2007.
- [73] M. Hadžiabdić and K. Hanjalić, "Vortical structures and heat transfer in a round impinging jet," *Journal of Fluid Mechanics*, vol. 596, pp. 221–260, 2008.
- [74] M. Cundy, P. Trunk, A. Dreizler, and V. Sick, "Gas-phase toluene LIF temperature imaging near surfaces at 10 kHz," *Experiments in Fluids*, vol. 51, no. 5, pp. 1169–1176, 2011.

- [75] J. Sakakibara, K. Hishida, and M. Maeda, "Vortex structure and heat transfer in the stagnation region of an impinging plane jet (simultaneous measurements of velocity and temperature fields by digital particle image velocimetry and laser-induced fluorescence)," *International Journal of Heat and Mass Transfer*, vol. 40, no. 13, pp. 3163–3176, 1997.
- [76] K. Hishida and J. Sakakibara, "Combined planar laser-induced fluorescence - particle image velocimetry technique for velocity and temperature fields," *Experiments in Fluids*, vol. 29, no. Supplement 1, pp. s129–s140, 2000.
- [77] L. Fan, Y. Gao, A. Hayakawa, and S. Hochgreb, "Simultaneous, two-camera, 2D gas-phase temperature and velocity measurements by thermographic particle image velocimetry with ZnO tracers," *Experiments in Fluids*, vol. 58, no. 4, pp. 1–34, 2016.
- [78] M. Trivedi, R. Jagannathan, and C. T. Johansen, "Convective heat transfer enhancement with nanoaerosols," *International Journal of Heat and Mass Transfer*, vol. 102, pp. 1180–1189, 2016.
- [79] B. C. Pak and Y. I. Cho, "Hydrodynamic and heat transfer study of dispersed fluids with submicron metallic oxide particles," *Experimental Heat Transfer*, vol. 11, no. 2, pp. 151–170, 1998.
- [80] E. Berrocal, E. Kristensson, M. Richter, M. Linne, and M. Aldén, "Application of structured illumination for multiple scattering suppression in planar laser imaging of dense sprays," *Optics Express*, vol. 16, no. 22, pp. 17870–17881, 2008.
- [81] E. Kristensson, L. Araneo, E. Berrocal, J. Manin, M. Richter, M. Aldén, and M. Linne, "Analysis of multiple scattering suppression using structured laser illumination planar imaging in scattering and fluorescing media," *Optics Express*, vol. 19, no. 14, pp. 13647–63, 2011.
- [82] Y. N. Mishra, F. A. Nada, S. Polster, E. Kristensson, and E. Berrocal, "Thermometry in aqueous solutions and sprays using two-color LIF and structured illumination," *Optics Express*, vol. 24, no. 5, pp. 4949–4963, 2016.
- [83] Y. N. Mishra, E. Kristensson, and E. Berrocal, "Reliable LIF/Mie droplet sizing in sprays using structured laser illumination planar imaging," *Optics Express*, vol. 22, no. 4, pp. 4480–4494, 2014.
- [84] E. Kristensson, A. Ehn, J. Bood, and M. Aldén, "Advancements in Rayleigh scattering thermometry by means of structured illumination," *Proceedings of the Combustion Institute*, vol. 35, no. 3, pp. 3689–3696, 2015.
- [85] E. Kristensson, E. Berrocal, and M. Aldén, "Two-pulse structured illumination imaging," *Optics Letters*, vol. 39, no. 9, pp. 2584–2587, 2014.
- [86] Y. N. Mishra, E. Kristensson, M. Koegl, J. Jönsson, L. Zigan, and E. Berrocal, "Comparison between two-phase and one-phase slipi for instantaneous imaging of transient sprays," *Experiments in Fluids*, vol. 58, no. 9, pp. 110/1–17, 2017.

- [87] E. Kristensson and E. Berrocal, “Crossed patterned structured illumination for the analysis and velocimetry of transient turbid media,” *Scientific Reports*, vol. 8, no. 1, pp. 1–9, 2018.
- [88] E. Hertle, S. Will, and L. Zigan, “Characterization of YAG:Dy,Er for thermographic particle image velocimetry in a calibration cell,” *Measurement Science and Technology*, vol. 28, no. 2, pp. 025013/1–7, 2017.
- [89] M. Storch, Y. N. Mishra, M. Koegl, E. Kristensson, S. Will, L. Zigan, and E. Berrocal, “Two-phase SLIPI for instantaneous LIF and Mie imaging of transient fuel sprays,” *Optics Letters*, vol. 41, no. 23, pp. 5422–5425, 2016.
- [90] B. Lecordier and J. Westerweel, “The EUROPIV Synthetic Image Generator (S.I.G.),” *Particle Image Velocimetry: Recent Improvements*, pp. 145–161, 2004.
- [91] A. Sciacchitano, B. Wieneke, and F. Scarano, “PIV uncertainty quantification by image matching,” *Measurement Science and Technology*, vol. 24, no. 4, pp. 045302/1–16, 2013.
- [92] B. Wieneke, “PIV uncertainty quantification from correlation statistics,” *Measurement Science and Technology*, vol. 26, no. 7, pp. 74002/1–10, 2015.
- [93] R. J. Adrian and C. S. Yao, “Pulsed laser technique application to liquid and gaseous flows and the scattering power of seed materials,” *Applied Optics*, vol. 24, no. 1, pp. 44–52, 1985.
- [94] D. Witkowski and D. A. Rothamer, “Investigation of aerosol phosphor thermometry (APT) measurement biases for Eu:BAM,” *Applied Physics B*, vol. 124, no. 10, pp. 202/1–14, 2018.
- [95] E. Kristensson, “Structured Laser Illumination Planar Imaging SLIPI Applications for Spray Diagnostics,” *Dissertation, Lund University*, 2012.
- [96] M. G. L. Gustafsson, “Nonlinear structured-illumination microscopy: Wide-field fluorescence imaging with theoretically unlimited resolution,” *Proceedings of the National Academy of Sciences*, vol. 102, no. 37, pp. 13081–13086, 2005.
- [97] B. Fond, C. Abram, M. Pougin, and F. Beyrau, “Investigation of the tin-doped phosphor $(\text{Sr,Mg})_3(\text{PO}_4)_2:\text{Sn}^{2+}$ for fluid temperature measurements,” *Optical Materials Express*, vol. 9, no. 2, p. 802, 2019.
- [98] H. Michelsen, C. Schulz, G. Smallwood, and S. Will, “Laser-induced incandescence: Particulate diagnostics for combustion, atmospheric, and industrial applications,” *Progress in Energy and Combustion Science*, pp. 1–47, 2015.
- [99] S. Will, S. Schraml, and A. Leipertz, “Two-dimensional soot-particle sizing by time-resolved laser-induced incandescence,” *Optics Letters*, vol. 20, no. 22, pp. 2342–2344, 1995.
- [100] S. Will, S. Schraml, and A. Leipert, “Comprehensive two-dimensional soot diagnostics based on laser-induced incandescence (LII),” *Symposium (International) on Combustion, Naples*, vol. 26, no. 2, pp. 2277–2284, 1996.

- [101] S. Will, S. Schraml, K. Bader, and a. Leipertz, "Performance characteristics of soot primary particle size measurements by time-resolved laser-induced incandescence.," *Applied Optics*, vol. 37, no. 24, pp. 5647–5658, 1998.
- [102] S. De Iuliis, F. Cignoli, S. Benecchi, and G. Zizak, "Determination of soot parameters by a two-angle scattering-extinction technique in an ethylene diffusion flame.," *Applied Optics*, vol. 37, no. 33, pp. 7865–74, 1998.
- [103] P. B. Kuhn, B. Ma, B. C. Connelly, M. D. Smooke, and M. B. Long, "Soot and thin-filament pyrometry using a color digital camera," *Proceedings of the Combustion Institute*, vol. 33, no. 1, pp. 743–750, 2011.
- [104] H. Guo, J. a. Castillo, and P. B. Sunderland, "Digital camera measurements of soot temperature and soot volume fraction in axisymmetric flames," *Applied Optics*, vol. 52, pp. 8040–8047, 2013.
- [105] W. M. Pitts, K. C. Smyth, and D. A. Everest, "Effects of finite time response and soot deposition on thin filament pyrometry measurements in time-varying diffusion flames," *Symposium (International) on Combustion, Colorado*, vol. 27, no. 1, pp. 563–569, 1998.
- [106] T. Lehre, B. Jungfleisch, R. Suntz, and H. Bockhorn, "Size distributions of nanoscaled particles and gas temperatures from time-resolved laser-induced-incandescence measurements," *Applied Optics*, vol. 42, no. 12, pp. 2021–2030, 2003.
- [107] T. P. Jenkins and R. K. Hanson, "Soot pyrometry using modulated absorption/emission," *Combustion and Flame*, vol. 126, no. 1, pp. 1669–1679, 2001.
- [108] C. Schulz, B. Kock, M. Hofmann, H. Michelsen, S. Will, B. Bougie, R. Suntz, and G. Smallwood, "Laser-induced incandescence: recent trends and current questions," *Applied Physics B*, vol. 83, no. 3, pp. 333–354, 2006.
- [109] R. Lemaire and M. Mobtil, "Modeling laser-induced incandescence of soot: a new approach based on the use of inverse techniques," *Applied Physics B*, vol. 119, no. 4, pp. 577–606, 2015.
- [110] B. McCoy and C. Cha, "Transport phenomena in the rarefied gas transition regime," *Chemical Engineering Science*, vol. 29, no. 2, pp. 381–388, 1974.
- [111] L. A. Melton, "Soot diagnostics based on laser heating," *Applied Optics*, vol. 23, no. 13, pp. 2201–2208, 1984.
- [112] K. C. Smyth and C. R. Shaddix, "The elusive history of $m = 1.57 - 0.56i$ for the refractive index of soot," *Combustion and Flame*, vol. 107, no. 3, pp. 314 – 320, 1996.
- [113] H. Leider, O. Krikorian, and D. Young, "Thermodynamic properties of carbon up to the critical point," *Carbon*, vol. 11, no. 5, pp. 555–563, 1973.
- [114] H. a. Michelsen, "Understanding and predicting the temporal response of laser-induced incandescence from carbonaceous particles," *Journal of Chemical Physics*, vol. 118, no. 20, pp. 7012–7045, 2003.

- [115] D. R. Snelling, K. a. Thomson, F. Liu, and G. J. Smallwood, "Comparison of LII derived soot temperature measurements with LII model predictions for soot in a laminar diffusion flame," *Applied Physics B*, vol. 96, pp. 657–669, 2009.
- [116] S. Dankers, S. Stephan, S. Will, and A. Leipertz, "Application of laser-induced incandescence to suspended carbon black particles," *Optics Letters*, vol. 32, no. 13, pp. 1160–1164, 2007.
- [117] A. Medalia and F. Heckman, "Morphology of aggregates—II. Size and shape factors of carbon black aggregates from electron microscopy," *Carbon*, vol. 7, no. 5, pp. 567–582, 1969.
- [118] B. M. Crosland, M. R. Johnson, and K. a. Thomson, "Analysis of uncertainties in instantaneous soot volume fraction measurements using two-dimensional, auto-compensating, laser-induced incandescence (2D-AC-LII)," *Applied Physics B*, vol. 102, no. 1, pp. 173–183, 2011.
- [119] P. E. Bengtsson and M. Alden, "Soot-visualization strategies using laser techniques," *Applied Physics B*, vol. 60, no. 1, pp. 51–59, 1995.
- [120] F. Goulay, L. Nemes, P. E. Schrader, and H. A. Michelsen, "Spontaneous emission from $C_2(d^3\Pi_g)$ and $C_3(A^1\Pi_u)$ during laser irradiation of soot particles," *Molecular Physics*, vol. 108, no. 7-9, pp. 1013–1025, 2010.
- [121] F. Liu, D. R. Snelling, K. A. Thomson, and G. J. Smallwood, "Sensitivity and relative error analyses of soot temperature and volume fraction determined by two-color LII," *Applied Physics B*, vol. 96, no. 4, pp. 623–636, 2009.
- [122] B. Tian, C. Zhang, Y. Gao, and S. Hochgreb, "Planar 2-color time-resolved laser-induced incandescence measurements of soot in a diffusion flame," *Aerosol Science and Technology*, vol. 51, no. 12, pp. 1345–1353, 2017.
- [123] R. K. Chakrabarty, H. Moosmüller, W. P. Arnott, M. A. Garro, J. G. Slowik, E. S. Cross, J. H. Han, P. Davidovits, T. B. Onasch, and D. R. Worsnop, "Light scattering and absorption by fractal-like carbonaceous chain aggregates: comparison of theories and experiment," *Applied Optics*, vol. 46, no. 28, pp. 6990–7006, 2007.
- [124] D. A. Khalitov and E. K. Longmire, "Simultaneous two-phase PIV by two-parameter phase discrimination," *Experiments in Fluids*, vol. 32, no. 2, pp. 252–268, 2002.
- [125] D. Towers, C. Towers, C. Buckberry, and M. Reeves, "A colour PIV system employing fluorescent particles for two-phase flow measurements," *Measurement Science and Technology*, vol. 10, pp. 824–830, 1999.
- [126] K. D. Driscoll, V. Sick, and C. Gray, "Simultaneous air/fuel-phase PIV measurements in a dense fuel spray," *Experiments in Fluids*, vol. 35, no. 1, pp. 112–115, 2003.
- [127] B. J. Petrosky, K. T. Lowe, P. M. Danehy, C. J. Wohl, and P. I. Tiemsin, "Improvements in laser flare removal for particle image velocimetry using fluorescent dye-doped particles," *Measurement Science and Technology*, vol. 26, no. 11, pp. 115303/1–13, 2015.

- [128] J. Sakakibara, R. B. Wicker, and J. K. Eaton, "Measurements of the particle-fluid velocity correlation and the extra dissipation in a round jet," *International Journal of Multiphase Flow*, vol. 22, no. 5, pp. 863–881, 1996.
- [129] Y. A. Hassan, T. K. Blanchat, C. H. Seeley, and R. E. Canaan, "Simultaneous velocity measurements of both components of a two-phase flow using particle image velocimetry," *International Journal of Multiphase Flow*, vol. 18, no. 3, pp. 371–395, 1992.
- [130] K. T. Kiger and C. Pan, "PIV Technique for the Simultaneous Measurement of Dilute Two-Phase Flows," *Journal of Fluids Engineering*, vol. 122, no. 2000, pp. 811–818, 2000.
- [131] G. D. Myers and A. H. Lefebvre, "Flame propagation in heterogeneous mixtures of fuel drops and air," *Combustion and Flame*, vol. 66, no. 2, pp. 193–210, 1986.
- [132] A. L. Sánchez, J. Urzay, and A. Liñán, "The role of separation of scales in the description of spray combustion," *Proceedings of the Combustion Institute*, vol. 35, no. 2, pp. 1549–1577, 2015.
- [133] A. Kourmatzis, P. X. Pham, and A. R. Masri, "Characterization of atomization and combustion in moderately dense turbulent spray flames," *Combustion and Flame*, vol. 162, no. 4, pp. 978–996, 2015.
- [134] J. Kariuki and E. Mastorakos, "Experimental investigation of turbulent flames in uniform dispersions of ethanol droplets," *Combustion and Flame*, vol. 179, pp. 95–116, 2017.
- [135] P. Julien, S. Whiteley, M. Soo, S. Goroshin, D. L. Frost, and J. M. Bergthorson, "Flame speed measurements in aluminum suspensions using a counterflow burner," *Proceedings of the Combustion Institute*, vol. 000, pp. 1–8, 2015.
- [136] S. Dankers, S. Schraml, S. Will, and A. Leipertz, "Application of Laser-Induced Incandescence for the Determination of Primary Particle Sizes of Nanoparticles Demonstrated Using Carbon Blacks," *Chemical Engineering & Technology*, vol. 25, no. 12, pp. 1160–1164, 2002.
- [137] T. A. Sipkens, R. Mansmann, K. J. Daun, N. Petermann, J. T. Titantah, M. Karttunen, H. Wiggers, T. Dreier, and C. Schulz, "In situ nanoparticle size measurements of gas-borne silicon nanoparticles by time-resolved laser-induced incandescence," *Applied Physics B*, vol. 116, no. 3, pp. 623–636, 2013.
- [138] F. Cignoli, C. Bellomunno, S. Maffi, and G. Zizak, "Laser-induced incandescence of titania nanoparticles synthesized in a flame," *Applied Physics B*, vol. 96, no. 4, pp. 593–599, 2009.
- [139] E. Nordström, N. E. Olofsson, J. Simonsson, J. Johnsson, H. Bladh, and P. E. Bengtsson, "Local gas heating in sooting flames by heat transfer from laser-heated particles investigated using rotational CARS and LII," *Proceedings of the Combustion Institute*, vol. 35, pp. 3707–3713, 2014.

- [140] S. S. Krishnan, K.-C. Lin, and G. M. Faeth, "Extinction and Scattering Properties of Soot Emitted From Buoyant Turbulent Diffusion Flames," *Journal of Heat Transfer*, vol. 123, no. 2, pp. 331–339, 2001.
- [141] B. F. Kock, B. Tribalet, C. Schulz, and P. Roth, "Two-color time-resolved lii applied to soot particle sizing in the cylinder of a diesel engine," *Combustion and Flame*, vol. 147, no. 1, pp. 79 – 92, 2006.
- [142] S. Balusamy, M. M. Kamal, S. M. Lowe, B. Tian, Y. Gao, and S. Hochgreb, "Laser diagnostics of pulverized coal combustion in O₂/N₂ and O₂/CO₂ conditions: velocity and scalar field measurements," *Experiments in Fluids*, vol. 56, no. 5, pp. 1–16, 2015.
- [143] Y. H. Li, C. Y. Wu, B. C. Chen, and Y. C. Chao, "Measurements of a high-luminosity flame structure by a shuttered PIV system," *Measurement Science and Technology*, vol. 19, no. 4, pp. 045401/1–11, 2008.
- [144] X. Sun and Y. Lei, "Fluorescent carbon dots and their sensing applications," *TrAC - Trends in Analytical Chemistry*, vol. 89, pp. 163–180, 2017.
- [145] H. Liu, T. Ye, and C. Mao, "Fluorescent carbon nanoparticles derived from candle soot," *Angewandte Chemie - International Edition*, vol. 46, no. 34, pp. 6473–6475, 2007.
- [146] A. Prasannan and T. Imae, "One-pot synthesis of fluorescent carbon dots from orange waste peels," *Industrial and Engineering Chemistry Research*, vol. 52, no. 44, pp. 15673–15678, 2013.
- [147] K. K. R. Datta, G. Qi, R. Zboril, and E. P. Giannelis, "Yellow emitting carbon dots with superior colloidal, thermal, and photochemical stabilities," *J. Mater. Chem. C*, vol. 4, no. 41, pp. 9798–9803, 2016.
- [148] L. Cao, X. Wang, M. J. Meziani, F. Lu, H. Wang, P. G. Luo, Y. Lin, B. A. Harruff, L. M. Veca, D. Murray, S. Y. Xie, and Y. P. Sun, "Carbon dots for multiphoton bioimaging," *Journal of the American Chemical Society*, vol. 129, no. 37, pp. 11318–11319, 2007.
- [149] Y. Willian, S. Shigeo, and Y. Hajime, *Phosphor Handbook*. Boca Raton: CRC Press, second ed., 2007.
- [150] C. Tiseanu, V. I. Parvulescu, M. Sanchez-Dominguez, and M. Boutonnet, "Temperature induced conversion from surface to "bulk" sites in Eu³⁺-impregnated CeO₂ nanocrystals," *Journal of Applied Physics*, vol. 112, no. 1, pp. 013521/1–9, 2012.